Óbuda University

Doctoral School on Materials Sciences and Technologies

Bánki Donát Faculty of Mechanical and Safety Engineering

Doctoral (PhD) Dissertation

The Effect of Ultrasound on the Inelastic Deformation of Metals

By:

Ali H. Alhilfi

Supervisor:

Prof. Dr. Endre Ruszinkó

Budapest, 2023

Content

Abstract

This dissertation discusses the effect of ultrasound on the inelastic deformation of metals. A model constructed in terms of the Synthetic theory of inelastic deformation has been developed. In the framework of the model, the following phenomena have been analytically described. (i) Ultrasonic temporary softening and residual softening or hardening; are recorded during the plastic flow of metals in the acoustic field. (ii) Ultrasound-assisted creep and stress relief (recovery). (iii) Ultrasound-assisted phase transformations (transformation plasticity and pseudoelastic deformation coupled with ultrasound). The extension of the synthetic theory is accomplished by introducing into its constitutional relationships new terms reflecting the impact of ultrasonic energy on the deformation state of sonicated material. The model results are consistent with the experimental data.

The list of used designations

T	Temperature, K
σ	Hydrostatic stress, Pa
ε	Strain
E	Young modulus, Pa
t	Time, s
$\mathcal{S}^3$	Ilyushin three-dimensional stress deviator space
$\mathcal{E}^3$	Ilyushin three-dimensional strain deviator space
$\vec{\boldsymbol{S}}$	Stress vector
$\dot{\vec{\boldsymbol{S}}}$	Stress rate vector
$\vec{\boldsymbol{e}}$	Strain vector
e_i	Macro level deformation vector components
$\vec{\boldsymbol{g}}_i$	$\mathcal{S}^3$ unit vector
$\vec{\boldsymbol{f}}_i$	$\mathcal{E}^3$ unit vector
σ_{ij}	Stress tensor component, Pa
ε_{ij}	Strain tensor component
σ_{kk}	Stress component
ε_{kk}	Strain component
S_{ij}	stress deviator tensor components
e_{ij}	strain deviator tensor components
δ_{ij}	Kronecker delta
J_2	second scalar invariant of the stress deviator tensor, MPa
V	Volume, cm^3
$\lvert\vec{\boldsymbol{S}}\rvert$	Stress vector length, MPa
S_1, S_2, S_3	Independent components
τ_0	Effective stress, MPa
$\tilde{\alpha}, \tilde{\beta}, \omega$	$\vec{\boldsymbol{l}}$ vector Descartes coordinate systemic direction cosines
$\vec{\boldsymbol{N}}$	Unit normal vector, MPa
$N_1, \cdots, N_5$	Components of vector $\vec{\boldsymbol{N}}$
I_N	Rate integral
H_N	Plane distance
α, β, λ	spherical angels

φ_N	plastic strain intensity
ψ_N	Defect intensity
I_N	Fault intensity, MPa, MPa 2
S_P	Creep limit
σ_P	creep limit of metal under uniaxial tension shear, MPa
τ_P	creep limit of metal under pure shear, MPa
γ	Stacking fault energy, $mJ\ m^{-2}$
B	Model constant
p	Model constant
r	Material constant
Θ	Model constant, MPa
K	Function of the homologous temperature, T
Q	Creep activation energy, KJ/mol
σ_S	Yield strength of material, MPa
φ_N^0	Total cumulative permanent strain intensity before the steady-state creep
K_1	Temperature- dependent function
K_2	Stress- dependent function
c	Model constant
p	Model constant
t_M	Active load duration, s
K	Model constants
φ_N^0	Deformation rate, s^{-1}
K_1	Creep limit the flow through current in the presence of MPa
K_2	Uniaxial drag secondary creep speed vector component
$\dot{\varepsilon}$	Model constant flow through current
Φ	The martensite fraction
A_s, A_f	Start and finish temperatures for austenite reaction
M_s, M_f	Start and finish temperatures for martensite reaction
$\dot{\Phi}$	Martensite fraction rate
$\dot{T}_e$	Rate of effective temperature
T_e	Effective temperature, K
D	Model constant
T_f	Austenitic transformation finish temperature, K
T_i	Temperatures as ultrasound is On, K
S_Φ	Tensile stress inducing martensitic transformation in the material, MPa
S_U	Stress vector

U	Ultrasonic energy density
U_t	Reflects the temporary softening action of ultrasound
σ_m	Vibrating stress amplitude MPa
$\vec{\boldsymbol{u}}$	Unit vector indicating the vibration mode
A_k	$(k = 1,2,3,4)$ Model constants
τ	Sonication duration
γ	Stacking fault energy
U_r	Reflects the residual action of ultrasound
φ_{NU}	Development of plastic slips
h	Heaviside step function
e_U	Plastic deformation in acoustoplasticity
σ_U	Unidirectional stress in ultrasonic field
c	Speed of sound
f	Frequency
ξ	Vibration amplitude
σ_S	Yield limit (yield stress)
$\Delta\varphi_{NU}$	Increment in plastic strain intensity
U_k	Ultrasound induced stress drop
U_C	Creep properties of a material in the ultrasonic field
S_m	Oscillating stress amplitude
$H_{\max}$	Maximum plane distance
e_u	The shape memory deformation
Δe	Plastic strain increment
ΔT	Temperature range when ultrasound is On
$U_{1,2}$	Model constant
r_U	Model constant
T_0	Temperature constant
e_U	Pseudoelastic strain component
ε_m	Amplitude of ultrasonic deformation
$S_{\Phi U}$	Ultrasound-assisted plastic (pseudoelastic) deformation
t_S	Instant of the start of plastic deformation.
$\tilde{t}$	Moment of the transition to the stationary creep.
ψ_{N0}	Number of defects cumulated in the material during plastic deforming
$H_{\max}$	Maximum plane distance for the whole loading history

Chapter I. Introduction

From the early decades of the 20th century, ultrasonic vibrations have been used to improve different types of manufacturing processes. Numerous investigations showed significant advantages of the plastic deformation method combined with ultrasonic oscillations to decrease forces and energy consumption, increase equipment capacity, and make it possible to deform materials that fail if treated by conventional methods. Ultrasonic vibration can significantly improve the plastic forming of metal, and the related technology has recently attracted much academic interest. Applying ultrasonic vibration in casting, welding, milling, drilling, drawing, extrusion, sheet forming processes, etc., has been widely studied. Another perspective branch of the utilization of ultrasound is the effect of ultrasound on the phase transformations of shape memory alloys.

The improvement of existing ultrasonic materials technologies and the development of new ones require studies of the effect of ultrasound on the structure and properties of metals and alloys via modern experimental techniques and modeling and simulation methods. The effects of ultrasonic vibration on material inelastic deformation, and the potential mechanisms behind these phenomena, have become foci for current research.

Although a considerable amount of experimental and theoretical research about the potential benefits of applying ultrasonic energy has been performed for several decades, the underlying physical principles remain elusive, and the analytical modeling of ultrasound-assisted phenomena is still far from completion.

Many vital phenomena were observed in metal deformation coupled with ultrasonic treatment. Their first group manifests itself during the plastic flow of metals in an acoustic field: ultrasonic temporary softening and ultrasonic residual hardening. While the former manifests itself during the simultaneous action of unidirectional and vibrating load, the latter enters into force in the post-sonicated state. The ultrasonic temporary softening is at the core of the energy consumption reduction during metal-forming processes because acoustic energy decreases the static stress value to induce/develop plastic deformation.

The other aspect where ultrasound action can be revealed is the ultrasound-assisted time-dependent processes such as creep deformation and the recovery of work-hardened materials. Ultrasonic waves accelerate primary and secondary creep deformation and induce/intensify the recovery processes of

plastically pre-strained materials. Understanding and modeling these phenomena' processes is crucial for predicting the processed material's deformation state and mechanical properties (e.g., relief processes, etc.).

Furthermore, ultrasonic vibrations have found wide application in shape memory alloy technology. It often happens that, because of structural features or other peculiarities, phase transformations (austenite/martensite) can not be induced for many applications in a direct way (heating/cooling). Other ways to initiate them are known: neutron irradiation, hydrostatic pressure, and ultrasonic action. The last method is the most attractive because ultrasonic vibration does not require expensive equipment like other methods.

In order to model the phenomena presented above, the Synthetic theory of inelastic deformation is proposed to be utilized. Its main peculiarity is a two-level approach to calculating deformations: macrodeformation results from the processes occurring on the micro level of the material and is derived via the behavior of the carriers of inelastic deformation (the crystalline grid defects – dislocations, point defects, twins, etc.). This feature of the Synthetic theory gives great room for maneuvering, making it possible to solve a wide circle of non-classical problems.

This dissertation aims to develop a model, in terms of the extended Synthetic theory, for the analytical description of inelastic deformation in the presence of ultrasound.

1.1 Objectives

The primary purpose of this work is to establish a model to predict and calculate the effects of ultrasound on the inelastic deformation of metals. The model is constructed in terms of the Synthetic theory. The following topics are covered:

I. Plastic deformation with ultrasound temporary and residual phenomena:

A. Acoustoplasticity
B. Residual hardening
C. Residual softening

II. The effect of ultrasound on the time-dependent processes

A. Ultrasound-assisted primary and secondary creep in the case of periodic and continuous action of ultrasound
B. Ultrasound recovery of work-hardened materials

III. Ultrasound-assisted phase transformations

A. Effect of ultrasound impulses on the austenite transformation
B. Martensite transformation (pseudoelastic deformation) in the presence of ultrasound

1.2 Scope

Chapter II emphasizes the progress that has been made, the present situation, and the open difficulties associated with the phenomenon studied in this dissertation. Examining findings derived from theory and experiment helps us understand the processes governing the phenomena to be modeled and support the analytical manipulations presented in Chapter IV.

Chapter III reveals the Synthetic theory's fundamental formulations, ideas, and concepts. First of all, a two-level approach to calculating inelastic deformations is proposed. Then the notion of stress vector and strain vector within the three-dimensional stress/strain deviator space framework is introduced. The next step, which makes up the core of the synthetic theory, is to show the principles of the construction of the yield surface (i.e., to define a yield criterion) and the evolution of the loading surface (i.e., to define a hardening rule). Further, equations for the quantities describing a stress-strain state of material on its microscopic level - strain intensity, defect intensity, and their interrelation – are presented. Finally, the procedure of the calculation of macrodeformation is considered. Two cases are considered: irrecoverable (plastic/creep) deformation of metals and the deformation resulting from phase transformations of shape memory alloys.

Chapter IV aims to model phenomena recorded in the experiments from Chapter II

Section 4.1 concentrates upon the extension of the Synthetic theory to model the effects of ultrasound on the plastic straining of metals. Here two terms were inserted into the plastic flow rule, which governs the deformation characteristic of material both during sonication and after it. The first term reflects the promoting action of ultrasound during the simultaneous action of static and alternating load. The second one characterizes how the post-sonicated material's defect structure affects the plastic flow after the ultrasound action terminates (residual softening or hardening).

Section 4.2 extends the Synthetic theory to model ultrasound-assisted temporary processes in metals. Introducing new terms that reflect the influence of acoustic energy on the processes governing the deformation state of metals enables us to solve/model the following problems: (i) creep deformation under the continuous and periodic action of ultrasound and (ii) ultrasound-induced recovery (relaxation) of work-hardened materials.

Section 4.3 aims to develop a model of the peculiarities of phase – direct (martensite) and reverse (austenite) –transformations of shape memory alloys in the ultrasound field. Manipulating with the central element of the Synthetic theory – effective temperature – responsible for developing both transformation plasticity (austenite transformation) and pseudoelastic deformation (martensite transformation), relationships that lead to a good agreement with experimental data are derived.

Chapter II. State of Art

Ultrasonic vibration is the physical vibration of molecules in the medium through which sound travels. Ultrasound refers to sound waves that exceed the audible frequency range, i.e., sound waves that are more than 20 kHz. Acoustic waves cause compressions and rarefaction (decompressions) in the medium particles as they travel through them.

Nowadays, ultrasonic technology is a convenient and accessible tool to assist many metalworking processes, such as machining, forming, joining, welding, microelectronic wire bonding, etc. Ultrasound shows various beneficial features: low energy consumption, high reliability and ampacity, "cold process," short process time, etc. That is why acoustoplasticity has received rapidly increasing interest from academics and industries. The outcome of ultrasonic integration in metal processing is sufficiently available in the literature: Yadav et al. (2005), Daud et al. (2006, 2007), Inoue (1984), Langenecker (1961, 1966), Kamarah et al. (1991), Siddiq et al. (2008a, 2008b), and Gallego et al. (2010). Ultrasonic application has become widespread in various metalworking processes, (Kumar et al. (2008), Thoe et al. (1998), Deng et al. (2016), Rukosuyev et al. (2010), Brehl et al. (2008), Kumar, (2013)), (see Fig. 2.1). The use of Ultrasonics in metallurgy dates to the early twentieth century. Many studies on various forming processes with ultrasonic assistance have been conducted for decades since the Austrian scientists Blaha and Langenecker (1955) reported that the yield stress could be significantly reduced when ultrasonic vibration was superimposed in the tensile test of Zinc single crystal for the first time.

The effect of ultrasound on the deformation properties of metals can be listed as follows:

1) Ultrasonic hardening.
2) Plastic deformation coupled with acoustic energy:
    a. ultrasonic temporary softening (acoustoplasticity),
    b. ultrasound residual effects: residual softening and residual hardening.
3) Ultrasound-assisted creep and stress relaxation.
4) Ultrasound-assisted phase transformation: austenite transformation and pseudoelastic deformation.

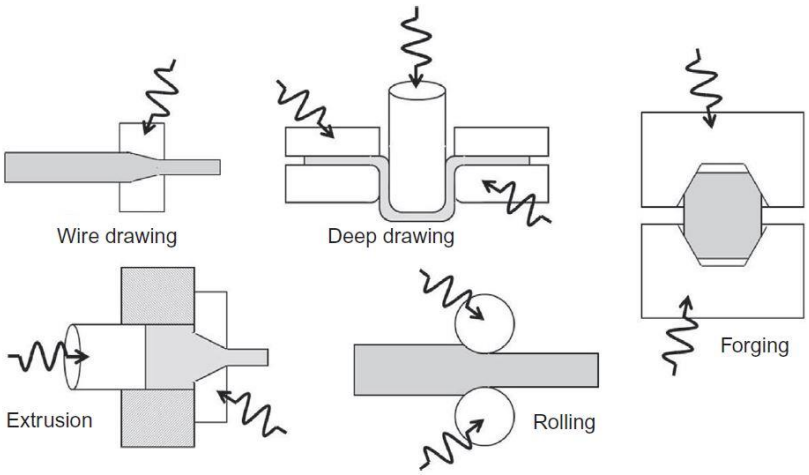

Fig. 2.1 Ultrasonics applied to metal forming processes. (Graff, 2015)

2.1 Vibrating systems for the ultrasonic irradiation of metals

Mechanical vibrations of ultrasonic frequency enable the conduction of accelerated aging tests of structural materials. A typical acoustic vibrating system is outlined in Fig. 2.2. It consists of

(i) *ultrasonic generator* (1),

(ii) *transducer* (2), which converts the electrical power into mechanical vibrations; it operates at the ultrasonic frequency spectrum (commonly between 15 and 100 kHz; whichever technology is used, the output end of the transducer will be oscillating, typically with an amplitude of 20 – 40 μm.). The transducer can be either of the magnetostrictive or the piezo-electric type. The transducer is coupled to the *waveguide system*:

(iii) *ultrasonic horn, conical* (4) and *cylindrical section* (5), (also known as acoustic horn, acoustic waveguide) is a device commonly used for augmenting the oscillation displacement amplitude provided by an ultrasonic transducer. The device is necessary because the transducers' amplitudes are insufficient for most practical power ultrasound applications. Another function of the ultrasonic horn is efficiently transferring the acoustic energy from the ultrasonic transducer into the treated media.

(iv) *sonicated specimen* (6),

(v) *supporters* (3) and (7), onto which the system is mounted,

(vi) *half-wave reflector* (8).

An essential characteristic of an acoustic system is a resonant regime of its operating, which is possible only when the length of all the elements of the system equals $\lambda/2$ or is multiply of $\lambda/2$. In this case, the superposition of direct and reflected waves constitutes a standing wave, which allows us to strictly determine the positions of stress/displacement nodes and antinodes along the specimen.

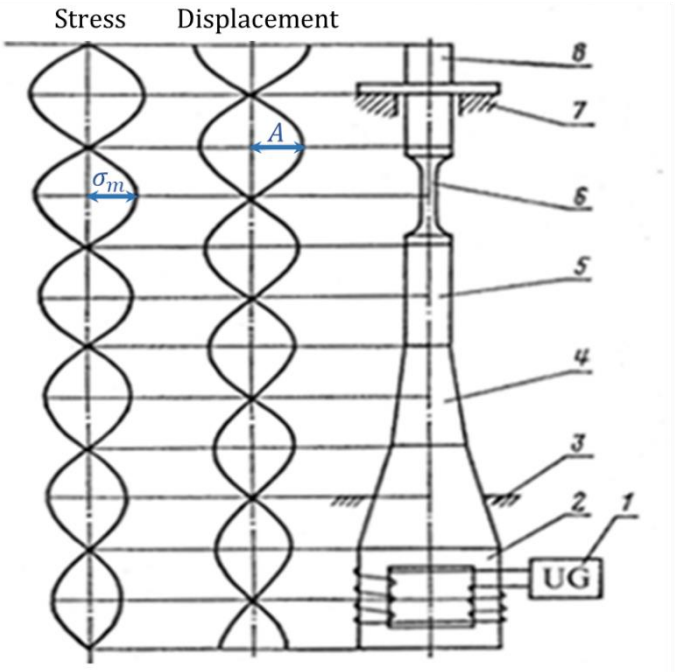

Fig. 2.2 Setup for the sonication (Rusinko, 2012)

Figs. 2.3 and 2.4 demonstrate vibrating systems for the simultaneous action of static and oscillating load for the cases of plastic deforming and creep testing, respectively.

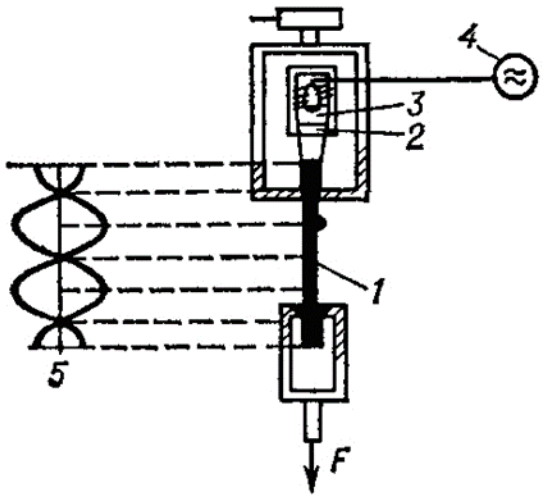

Fig. 2.3 Scheme of static load (F) combined with ultrasound: 1– specimen; 2 – concentrator, 3 – transducer, 4 – generator, 5 – displacement distribution along the specimen (Golyamina, I. et al., 1979)

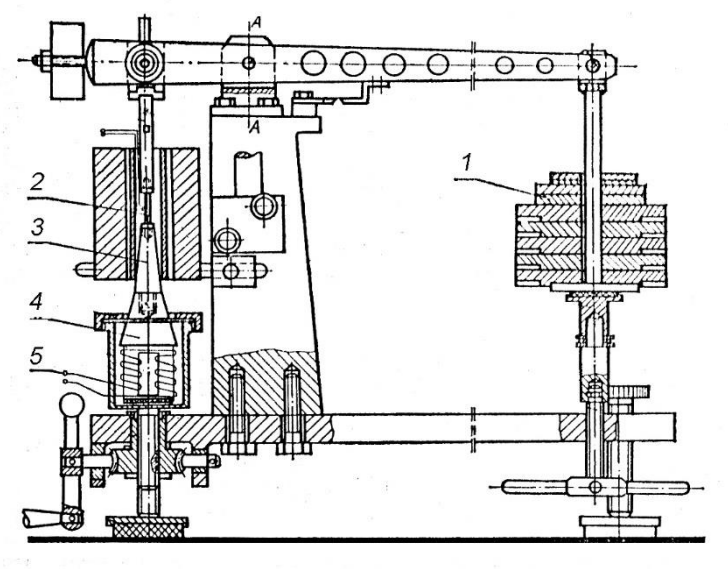

Fig. 2.4 Creep test stand coupled with vibrating system: 1 – weights, 2 – specimen, 3 – concentrator, 4 – transducer powered via input terminal 5 (Severdenko, 1979)

The following table collects the main ultrasound parameters and their relationships (Fitzpatrick, 2018), which will be used further throughout (see Fig. 2.2):

Table 2.1 The main terms and relationships

Term	***Designation***	***Units***
The amplitude of oscillation/displacement/vibration	A	μm
The amplitude of alternating stress	σ_m	MPa
Ultrasound intensity/sound energy density	U	$\frac{\mathrm{J}}{\mathrm{m}^3} = \mathrm{MPa}$
$\sigma_m = EA\frac{\omega}{c}$		
$U = \frac{1}{2}\rho A^2\omega^2$		
$U = \frac{1}{2}\rho\left(\frac{c\sigma_m}{E}\right)^2$		
Amplitude of ultrasonic deformation	ε_m	-
$\varepsilon_m = \frac{\sigma_m}{E}$		
Density	ρ	$\frac{\mathrm{kg}}{\mathrm{m}^3}$

Speed of sound	c	$\frac{\mathrm{m}}{\mathrm{s}}$
Young's modulus	E	Mpa

2.2 Ultrasonic hardening

Ultrasonic hardening is observed during the sonication of metals in the annealed state. The first research on the fine structure of metals was conducted by Langenecker (1966) on the wire specimens of monocrystal aluminum (99.99%). The specimens were subjected to ultrasound with an intensity of 25 W/cm^2. It was found that the ultrasonic irradiation increased dislocation density, by several orders of magnitude; a grain structure was observed whose subgrains are stretched in the direction of the wave propagation. Later, employing X-raying, Langenecker directly observed dislocation multiplication in the acoustic field.

Fig. 2.5 demonstrates the transmission electron micrographs of iron-foil (carbon content of 0.003 %) subjected to the action of ultrasound. As seen from Fig. 2.5, the dislocation distribution is strongly non-homogeneous. As a rule, the dislocations are concentrated in tangles and tied into knots, with many immobile jogs on them. A significant number of small dislocation loops formed by the agglomeration of vacancies are observed. Pileups of dislocations near the grain boundaries are also reported in the works of Westmacott (1965) and Langenecker (1966), and it can be assumed that the grain boundaries are the prevailing sources of dislocations under the action of ultrasound.

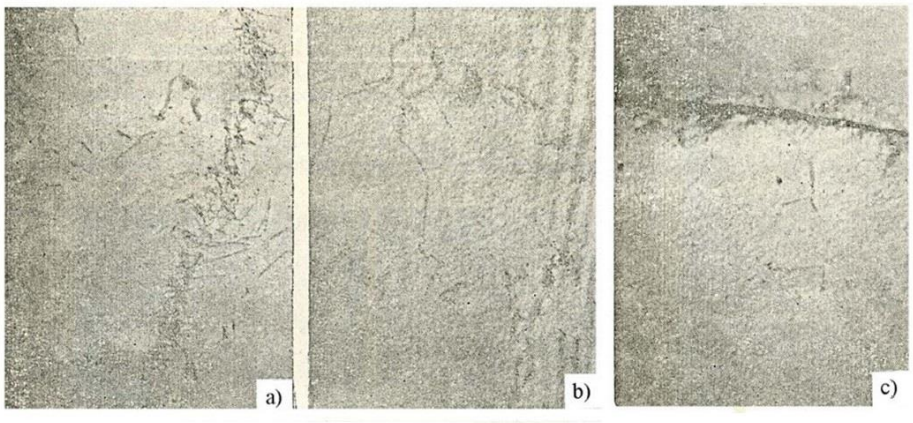

Fig 2.5 The dislocation structure of iron subjected to ultrasonic irradiation (×50000): $t = 20$°C, a, b – oscillating stress amplitude $\sigma_m = 200$ MPa; c – $\sigma_m = 20$ MPa; cycle numbers $2 \cdot 10^6$ oscillating frequency $f = 20$ kHz; (Kulemin, 1978).

Fig. 2.6 shows the microstructure of the germanium surface after several impulses of ultrasound loading; the etching follows every impulse. It is easy to see that some fraction of etch-pits remains on their spots (immobile dislocations), while others move in appropriate directions (mobile dislocations). Therefore, despite the periodic change in the sign of vibrating loading, the dislocations move only in one direction. This peculiarity is explained by crystal imperfections (point defects) that trail behind the moving dislocation.

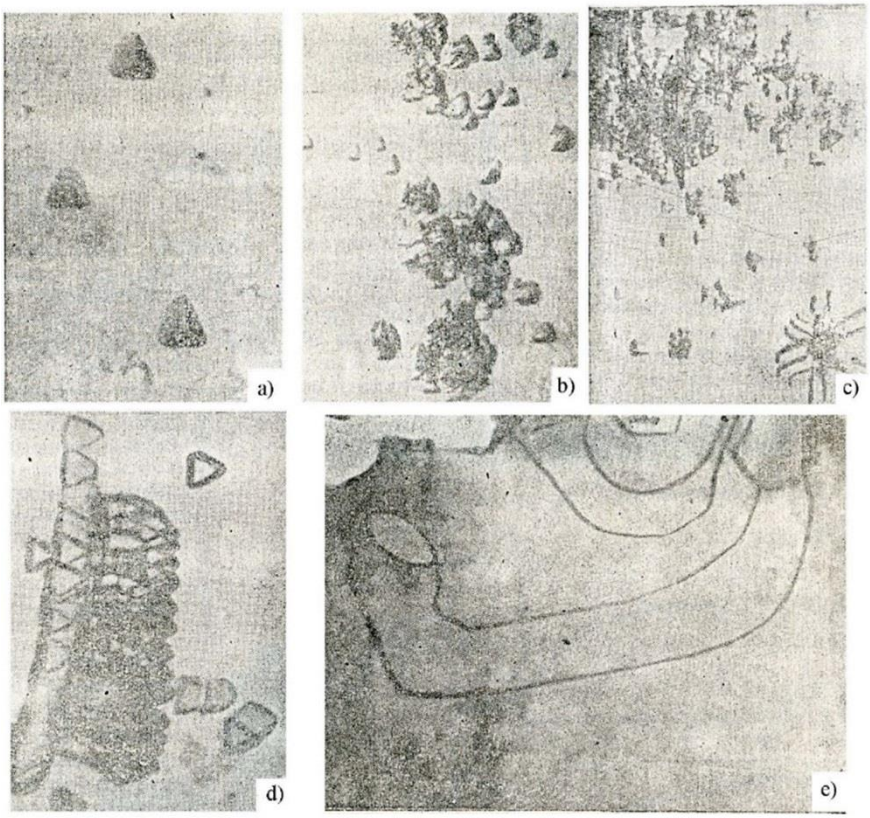

Fig. 2.6 Dislocation structure of germanium: a) initial surface of germanium (×450); b) and c) during sonication – sonication time $\tau = 3$ min and 5 min at $t = 400$℃, stress amplitude $\sigma_m = 3$ MPa (×270); d) layer-by-layer etching after the sonification of $\tau = 0.5$ min, $\sigma_m = 3$ MPa (×450); e) electron micrograph of sonicated germanium $t = 600$℃, $\sigma_m = 3$ MPa, $\tau = 10$ min (×60000); (Kulemin, 1978).

The degree of ultrasonic hardening depends on the intensity and duration of acoustic action. Fig. 2.7 demonstrates the dislocation density (N_d) and hardness (h_μ) of aluminum and germanium as a function of sonication time (τ). As can be seen from this figure, the dislocation density, first increases and then, beginning with some value of sonication time, remains unchangeable. The saturation of the dislocation density results seemingly from the fact that dislocation sources tend to slow down their action due to the stresses induced by the dislocations nucleated at previous loading cycles. Annihilation of the dislocations of opposite signs emanating from sources located in parallel atomic planes explains the mechanisms governing the stabilization of the dislocation density. The manner of the growth of dislocation density repeats in the increase of the yield strength of annealed materials in the course of sonication (Fig. 2.8).

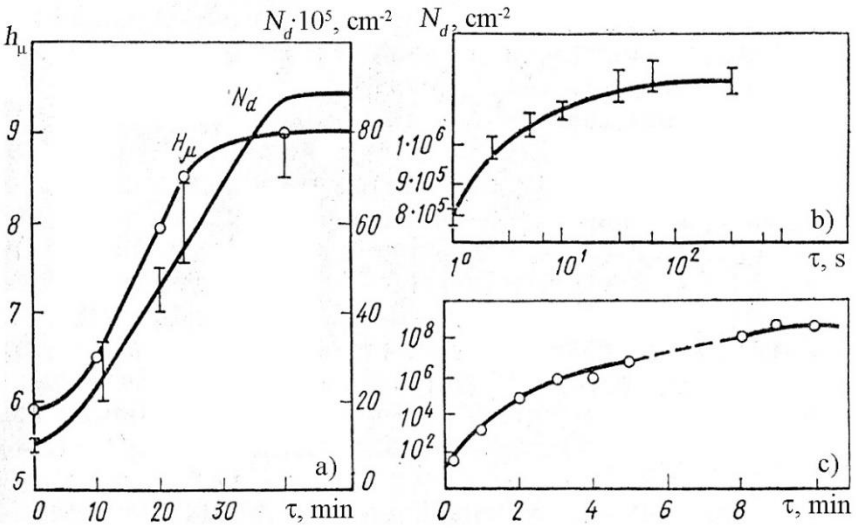

Fig. 2.7 Dislocation density and microhardness of aluminum (a) and (b) and germanium (c) as a function of ultrasound-action-time τ: a) $t = 50$℃, stress amplitude $\sigma_m = 20$ MPa; b) $t = 20$℃, $\sigma_m = 18$ MPa; c) $t = 700$℃, $\sigma_m = 18$ MPa; (Kulemin, 1978).

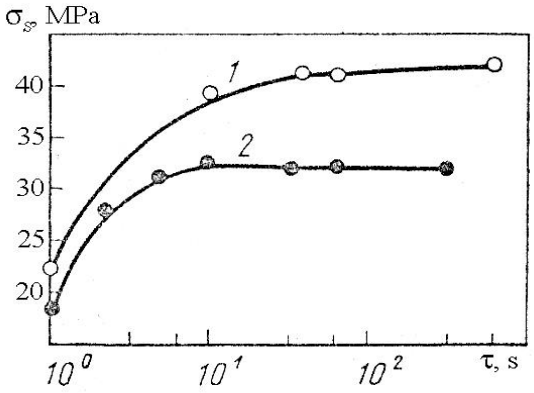

Fig. 2.8 Dependence of the yield limit of copper (1 – stress amplitude $\sigma_m = 67$ MPa) and aluminum (2 – $\sigma_m = 164$ MPa) on the ultrasound action time τ; (Kulemin, 1978).

With the effect of the acoustic energy intensity (stress amplitude) on the ultrasonic hardening, a monotonic increase in the dislocation density, and therefore in yield strength and strength limit, is recorded in experiments (Figs. 2.9 and 2.10). It must be noted that a threshold for minimum vibrating stress amplitude exists, beneath which the hardening effect is absent. For various materials, its value is about 25-50 % of the magnitude of yield strength.

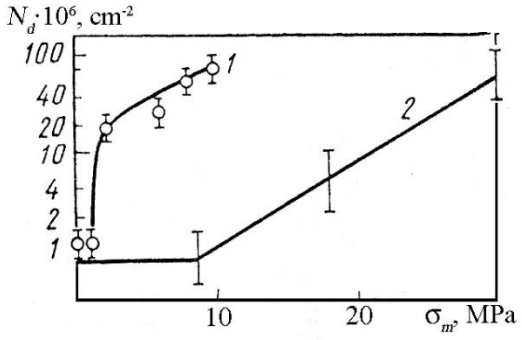

Fig. 2.9 N_d vs. σ_m plot for 1) copper at $t = 450$℃ and 2) aluminum at $t = 20$℃; (Kulemin, 1978).

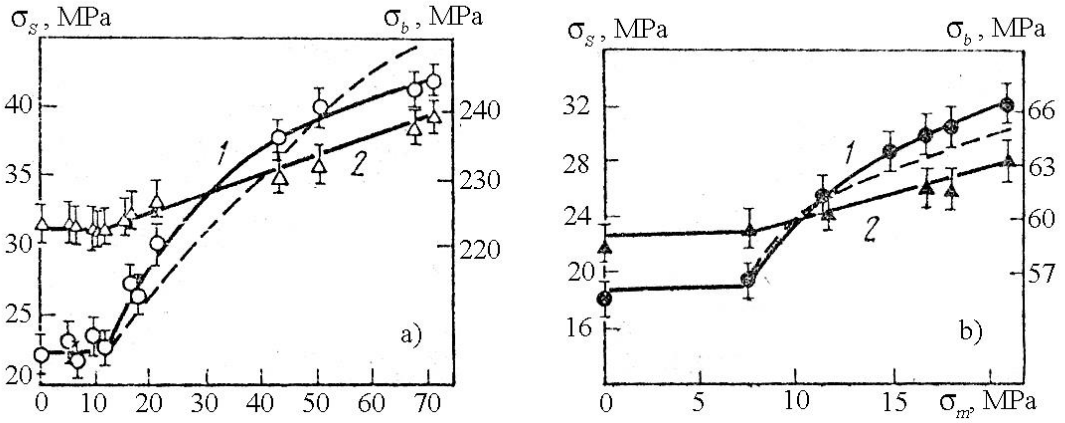

Fig. 2.10 Dependence of the yield strength σ_S (1) and strength limit σ_b (2) of copper (a) and aluminum (b) on the ultrasonic stress amplitude (σ_m); sonication time $\tau = 60$ s; (Kulemin, 1978).

2.3 Acoustic Temporary Softening

Acoustic temporary softening (acoustoplasticity) is observed during the simultaneous action of unidirectional and vibrating load and manifests itself in a considerable decrease in the stress needed to induce/develop plastic deformation.

Fig. 2.11 shows one of the earliest experimental results on the acoustoplasticity obtained by Blaha (1955) and Schmidt (1935). As shown in Fig. 2.11b, heating the specimen can be similar in effect to ultrasonic action. However, according to Kumar et al. (2017) and Zohrevand et al. (2022), acoustic softening is thought to be more efficient than thermal softening-induced plasticity; experimental results reveal that the ultrasonic energy required to produce an identical amount of softening is 10^7 times less than the required thermal energy Yadav et al. (2005). The researchers explain this fact by the difference in the material's thermal and acoustic energy absorption mechanism. While the former leads to the oscillation

of the whole crystalline grid, the latter concentrates on the defects of the metallic structure. Blaha (1955) proposed that preferential absorption of ultrasonic energy at the crystalline lattice defects increases dislocation mobility and allows the metal to deform at a lower load.

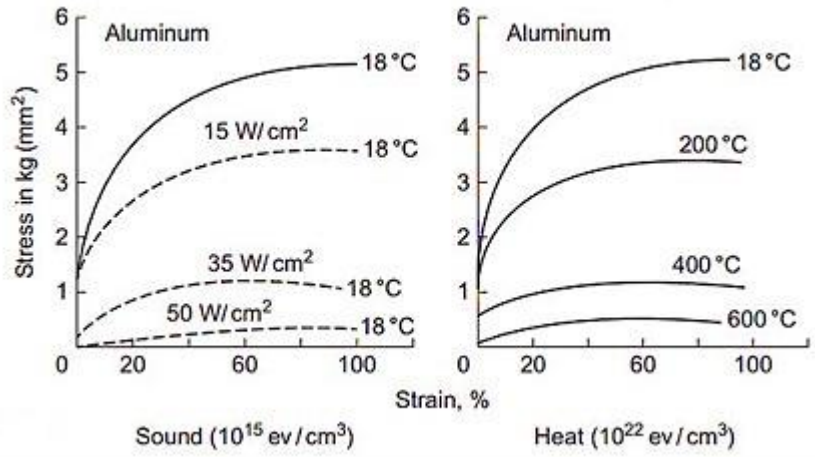

Fig. 2.11 Stress-strain diagrams of (a) zinc (Langenecker, 1963) (Blaha, (1955) and (b) aluminum (Schmid, 1935) in the ultrasonic field. The diagrams from (b) show the equivalence of ultrasound treatment to increased temperature.

The effect of ultrasound temporary softening has been widely used in many branches of contemporary metal-forming processes for decades.

When ultrasonic vibration was used in Dry Creep-Feed Up-Grinding (Abdullah et al. 2013), a reduction of up to 61% in maximum horizontal grinding force and 46% in maximum vertical grinding force for Al 7075 specimens was measured. The reduction in steel X210Cr12 specimens was up to 54% in maximum horizontal grinding force and 75% in maximum vertical grinding force.

The experimental results presented by Malekipour et al. (2020) demonstrated that continuous ultrasonic vibrations with an amplitude of 5 μm during the deep drawing process led to a 5.6% decrease in average forming load and a 50% increase in drawing depth.

Susan et al. (2007) examined cold-rolling of steel strips (yield strength 996 MPa) in the ultrasonic field, Fig. 2.12. They found that the application of ultrasound led to a decrease in the yield strength of the considered material. The yield strength in the acoustic field with the amplitude of the vibration of 10 μm becomes 910 MPa, and for 15 μm is 899 MPa.

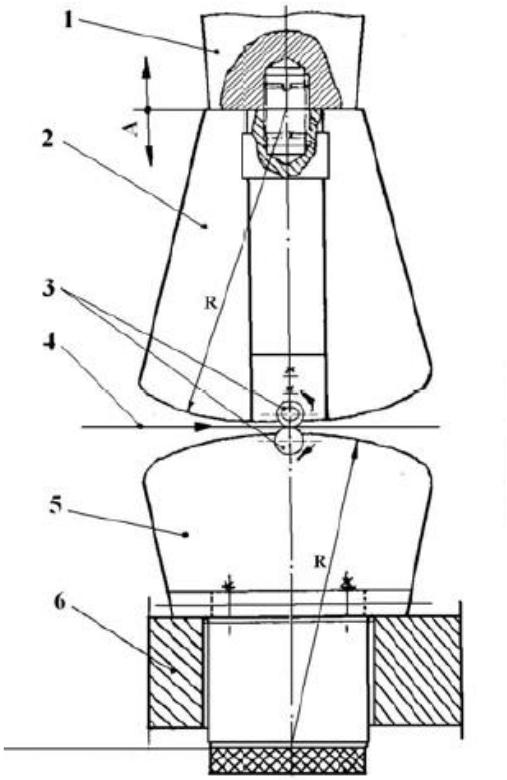

Fig. 2.12 Scheme of the metal strip rolling with ultrasonic activation. 1− transductor PMS 15A-18; 2, 5 − segments of backing-up rolls; 3 − workings rolls; 4 – metal strip; 6− fastening element; Susan et al. (2007)

The results presented above and many other reports in scientific literature led to an important conclusion that the acoustoplastic effect is enhanced by the increase in the ultrasonic energy injected into the material.

Despite numerous experimental and numerical analyses about the potential benefits of applying ultrasonic energy, the underlying physical principles remain elusive. Two categories of interpretation can be indicated: (**i**) stress superposition and (**ii**) direct acoustic softening.

In terms of the stress superposition theories, the softening effect is the outcome of the macroscopic superposition of steady and alternating stress. For example, Malygin (2000) implies that ultrasonic waves activate anchored dislocations hardened under ordinary deformation, thereby reducing the stresses needed for further inelastic deformation.

At the same time, the superposition hypothesis can only partially explain the drop in flow stress that occurs during ultrasonic vibration. The first reason for such a conclusion is the experimental results obtained by Daud et al. (2007), where the total amount of stress reduction on the stress-strain curve is generally higher than the result of stress superposition alone. Furthermore, the superposition hypothesis cannot substantiate residual hardening or softening effects (see the next point) observed after ultrasonic vibration is stopped. These can be attributed to the permanent changes in the material's microstructure

during ultrasonic sonication (direct acoustic softening). Deshpande et al. (2019), Lum et al. (2009), and Huang et al. (2009) suggest that these permanent changes are caused by dynamic annealing/softening induced by heat input from ultrasonic vibration. In other words, they draw an analogy between the effects of hot deformation and ultrasound action and indicate that similar microstructures evolve in thermal and ultrasonic fields.

Another mechanism to be mentioned here that contributes to the permanent changes of a crystalline grid in an acoustic field is the decrease in the number of dislocations via dipole annihilation. Shao et al. (2021) suggest that dislocations travel longer distances in a jerky manner in the presence of UV. As a result, there is a greater probability of opposite dislocation meetings and annihilation, and the dislocation density eventually decreases. The dislocation density drop makes the material's structure softer in the post-sonicated state.

Despite the debates between the supporters of stress superposition and direct acoustic softening, the researchers agree that ultrasound temporary softening is contributed by both factors (Graff, 2015).

2.4 Ultrasonic residual effects

The permanent microstructure changes cumulated during the acoustoplasticity mentioned above result in two phenomena, ultrasonic residual hardening and softening.

Fig. 2.13 shows schematically the phenomena caused by ultrasonic energy. As one can see, switching on the ultrasound incurs a step-wise decrease in acting stress (*AB*). During simultaneous unidirectional and oscillatory load (acoustoplasticity), the material flows at less stress than when mechanical stress acts alone (*BC*). Portions *AB* and *BC* reflect the ultrasonic temporary softening considered in point 2.1. As ultrasound is off, two variants are possible:

(**i**) residual hardening – beyond point *D* curve runs above that corresponding to the ordinary loading (Fig. 2.13a);

(**ii**) residual softening – beyond point *D* curve is located beneath the ordinary one (Fig. 2.13b).

In summary, both figures demonstrate that acoustic softening exists only temporarily while the vibration is applied. At the same time, apart from temporary softening, the residual effects can be observed after the vibration terminates and causes different responses of post-sonicated material.

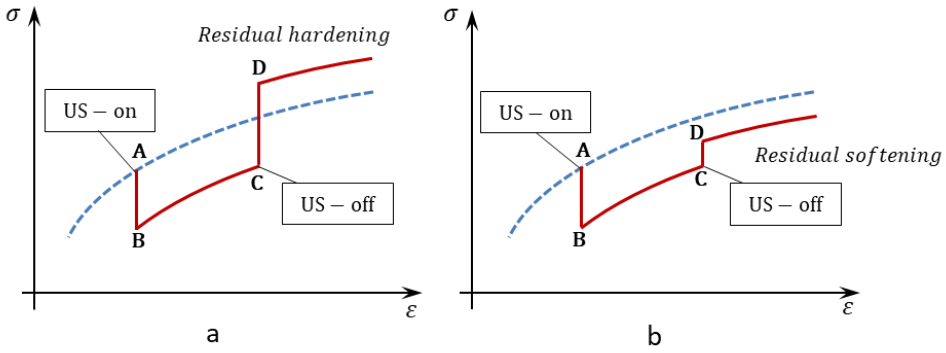

Fig. 2.13 Ultrasonic effects

Researchers attribute the residual acoustic effect to the net balance between ultrasound's dynamic annealing and its potential opposing effect on activating and multiplying dislocations. In other words, the residual effect refers to the phenomenon in which the flow stress rises above or below the flow curve, comparing with the ordinary curve, without ultrasonic agitation involved during the subsequent deformation after the ultrasound is stopped.

The mechanism of ultrasound-assisted dynamic annealing mainly depends on sonicated material's stacking fault energy (SFE). Following Deshpande et al. (2018, 2019), even though aluminum and copper have the same face-centered cubic (FCC) crystal structure, they recover through different annealing mechanisms, which results in a markedly different microstructure after deformation in the presence of ultrasonic energy.

It is well-known how stacking fault energy affects the recovering mechanism metals. Dislocations in the (111) closed packed slip plane for FCC metals move along (110) direction. The stacking fault energy of the material determines whether dislocations move as complete dislocations or by dissociation of dislocations into two partial dislocations (Shockley partial dislocations). The dislocation motion by dissociation into two partials is preferred for metals like gold, nickel, and copper with low to medium stacking fault energy because it requires less energy to create the wide stacking fault associated with dissociation. The dissociation and formation of this stacking fault inhibit climb and cross-slip, restricting recovery and increasing dislocation density. Beyond a specific limit, the local difference in dislocation density results in grain nucleation. This phenomenon of new grain nucleation and growth during deformation is called discontinuous dynamic recrystallization (DDRX). For high stacking fault energy materials like aluminum, the dissociation of dislocations is not energetically favored. Hence the motion of dislocations happens as perfect dislocations or with a stacking fault with a very small width. This promotes climbing and cross-slip, facilitating dynamic recovery (DRV). The resulting microstructure in the high stacking fault energy materials contains subgrains with grain-interiors having much lower dislocation. [Deshpande et al. (2019), Sakai et al (2014), Huang et al. (2016)].

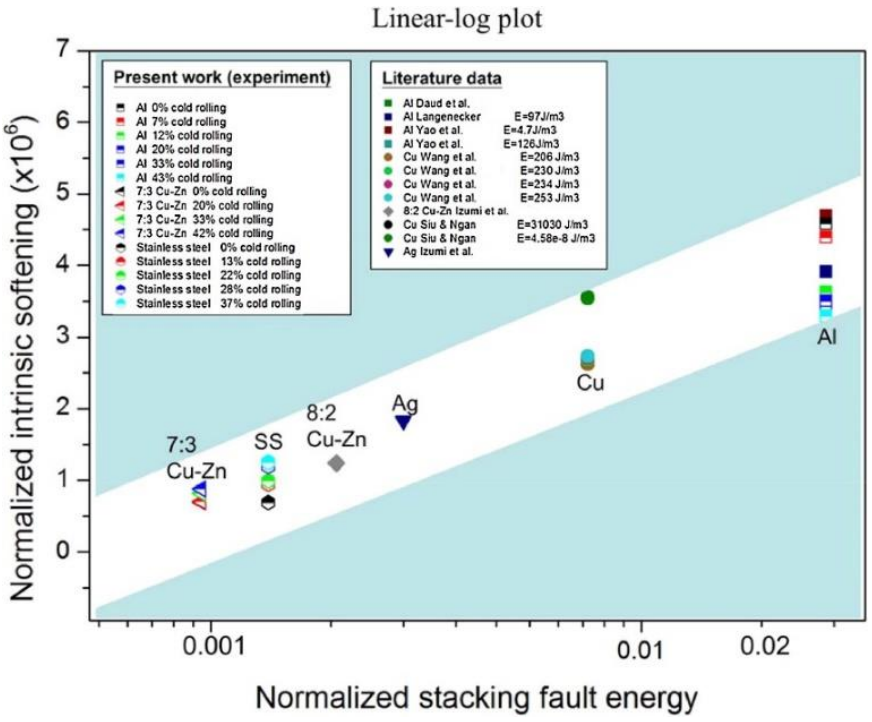

Fig. 2.14 Normalized intrinsic softening vs. normalized stacking fault energy. Siu et al., 2019

Humphreys et al. (2012) sum up: the SFE extent affects the microstructural processes connected to the dislocation activity, such as recovery and recrystallization,

Residual hardening

Consider band contrast maps with grain boundaries of aluminum (a material with high SFE) shown in Fig. 2.15. It is evident that the compression (Fig. 2.15b) as well as the ultrasound-assisted compression (Fig. 2.15c) both introduce low angle (2–15°) grain boundaries to the samples compared with the initial sample (Fig. 2.15a). The most significant number of low-angle grain boundaries appear in the vibrated sample and many of the low-angle grain boundaries have a closed shape within the large grains with high-angle grain boundaries, indicating that the compression increases the number of substructures, such as sub-grain boundaries in the aluminum and that, with the application of ultrasonic vibration, the formation of sub-grain is promoted (Zhou et al., 2017). It is clear that the microstructure from Fig. 2.15c formed during the simultaneous action of static and vibrating load requires greater stress to overcome the post-sonicated state's obstacles and continue plastic flow. This study used commercially pure aluminum Al1060 and titanium ERTA1ELI in an ultrasonic-assisted compression (UAC) test. The aluminum samples were cylinders with a diameter of 4 mm and heights of 2 mm, 4 mm, and 8 mm, while the titanium samples were annealed titanium bars. The ultrasonic-assisted compression test was conducted on a universal testing machine (Hualong-WDW300), with the loading speed adjusted to maintain a constant strain rate of $0.005\ s^{-1}$ for each sample. Three different vibration frequencies were prepared to investigate the influence of vibration frequency on metal plasticity during UAC. For each set of

experiment apparatus, specific ultrasonic horn and transducer were applied to match their resonant frequency to the input current frequency. The surface of the ultrasonic horn was measured using a Doppler Vibro-meter (PSV-400) when a load of 3000 N was applied on the horn. The experiment involved applying transient ultrasonic vibration to an aluminum sample with a height of 8 mm, causing elastic deformation. The sample was compressed until the load reached 200 N, and then held by holding the crosshead. The average engineering stress in the sample was about 15.9 MPa, and the deformation was elastic. A 20 kHz ultrasonic vibration with amplitude about 15.0 μm was applied, and the sample was immediately unloaded. A loading-transient vibrating loading cycle experiment was conducted to study the development of the ultrasonic softening effect. A normal compression was applied to a titanium sample with a height of 2.4 mm, and when the crosshead moved upward by 0.6 mm, a 30 kHz ultrasonic vibration with amplitude of 10.37 μm was applied to the sample. The compressive force immediately dropped due to the applied ultrasonic vibration. To study the transient UAC induced deformation and the ultrasonic softening mechanism, anoindentation tests were conducted along the longitudinal axis of the aluminum and titanium samples. The original aluminum (4 mm in height) and titanium (2.4 mm in height) samples, as well as the compressed and UAC samples, were prepared for the nanoindentation tests. The samples were cut and mounted into resin, mechanically polished to a fine surface, and finally polished with 0.04 μm colloidal silica to reach a mirror-like surface without polishing-induced residual stress. The nanoindentation of the aluminum sample was conducted with a load of 2 mN, while the loading rate and unloading rate were both 2 mN/s. Similar nanoindentation tests were conducted on the titanium samples with a load of 5 mN and loading speed of 5 mN/s. For all the samples a step size of 5 μm was applied between two indents.

For the study investigates metal plasticity under high-frequency vibration using vibration-assisted upsetting (compression) tests, Yao et al. (2012) used a DC motor controls the compression motion, while a magnetostrictive transducer generates high-frequency oscillation applied to the specimen. Stress-strain curves are obtained from force sensors and laser displacement sensors. A titanium horn is used as the compression punch, amplifying the vibration generated by the transducer. The longitudinal and transverse vibration at the horn tip is measured using an inductive displacement sensor connected to a DSP lock-in amplifier. The working frequency is 9.6 kHz, with significant transverse vibration at the horn tip. Commercially pure aluminum (Al 1100) in annealed condition is used in the upsetting tests. The dimensions of each sample is 2.032 mm in diameter and 2 mm in length. The material after annealing usually has a random texture or very weak texture, with an assumed $M = 3.06$, a typical value for polycrystalline FCC metals.

Fig. 2.16 reported by Zhou et al. (2017) vividly demonstrates the residual hardening phenomenon, the σ~ε curves for aluminum after the ultrasound is off run above the ordinary stress-strain diagram. This effect depends on the ultrasonic vibration amplitude and shows an increasing manner.

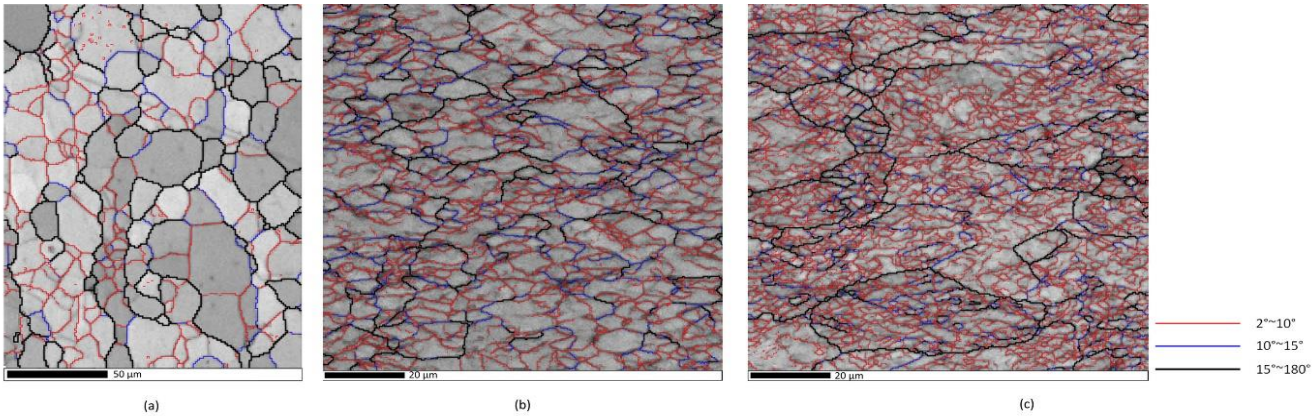

Fig.2.15 Band contrast map for aluminum with grain boundaries for (a) initial state, (b) compression, and (c) ultrasound-assisted compression, Zhou et al. (2017).

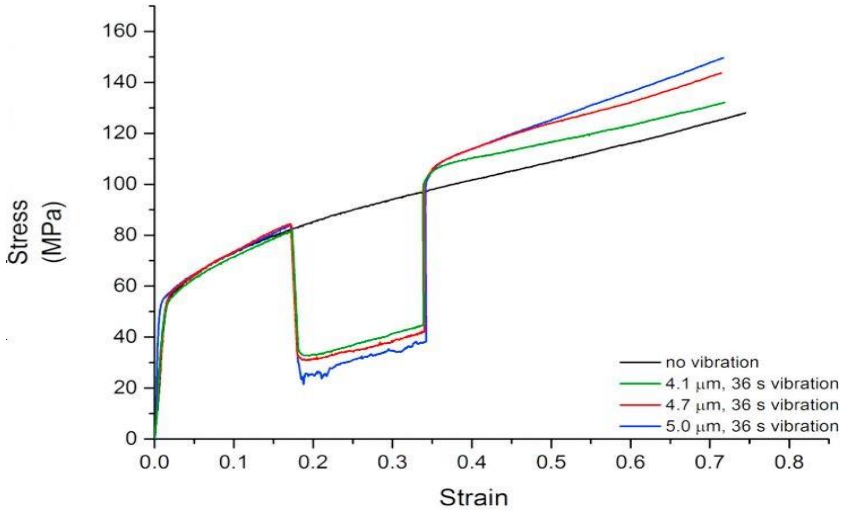

Fig. 2.16 Softening and residual effects of ultrasonic vibration with different vibration amplitudes on aluminum samples, Zhou et al. (2017).

Another factor affecting the amount of residual hardening is the duration of sonication.

Inspect Fig. 2.17, showing schematically the course of vibration-assisted $\sigma\sim\varepsilon$ diagrams. As ultrasound is on at points A_1 and B_1, the stress drop ($\Delta\sigma$) is observed. It must be noted that $\Delta\sigma_{B_1B_2} > \Delta\sigma_{A_1A_2}$ at the same intensity of ultrasound applied. Therefore, the greater stress is acting, the more significant effect from the sonication can be expected. In other words, the greater deformational energy accepts the

additional ultrasonic one, the more remarkable softening occurs. A_2A_3 and B_2B_3 portions show identical tendencies: the simultaneous action of unidirectional and vibrating stresses results in smaller stress values needed to continue the plastic deforming (temporary ultrasonic softening).

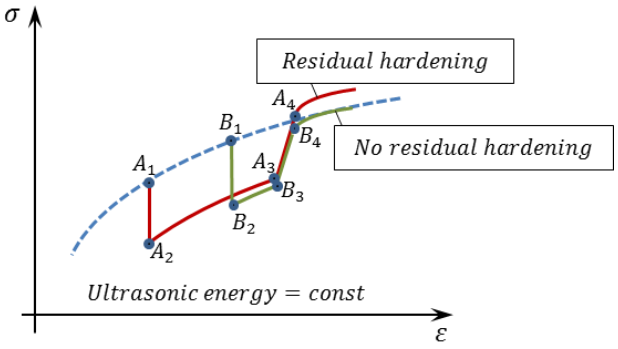

Fig. 2.17 Schematic stress~strain diagrams with the sonications of different duration.

As the ultrasound is off (points A_3 and B_3), the plastic deformation starts after elastic portions A_3A_4 and B_3B_4. That is where the ultrasonic residual hardening can manifest itself. This phenomenon strongly depends, among other things, upon the sonication duration. As the ultrasound is off at points A_3, i.e., after eight seconds of sonication, the plastic straining develops at a higher stress level than at ordinary loading. At the same time, the plastic straining, which follows two-second sonication, returns on $\sigma\sim\varepsilon$ curve corresponding to the ordinary loading. Therefore, the ultrasound intensity and its duration influence post-sonicated material behavior. To put this another way, if the ultrasound energy does not provide substantial changes in the defect structure of the material, the residual effects are not observed.

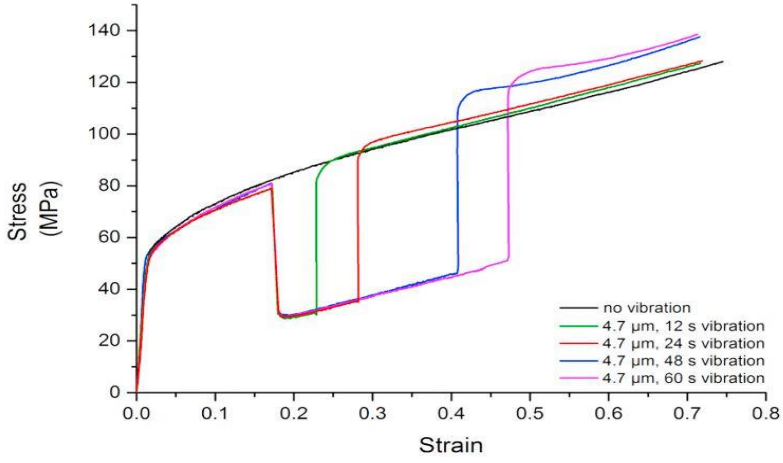

Fig. 2.18 Softening and residual hardening effects of ultrasonic vibration with different vibration durations on aluminum samples, Zhou et al. (2017).

The experimental confirmation of the considerations above is presented in Fig. 2.18, plotted by Zhou et al. (2017). While the time of sonication (τ) is 12 s and 24 s, no residual effect is observed; for $\tau = 48$ s

and $\tau = 60$ s, a considerable increase in stress appears. Thus, together with acoustic intensity, the time of ultrasound application plays an important role. In other words, the amount of ultrasonic energy injected into the material determines the degree of residual effects.

Residual softening

To study this phenomenon, Liu et al. (2022) conducted experimental research for copper (a material with low SFE), ultrasound-assisted tension of 200 μm thick T2 copper foil. Stress-strain parameters revealed the existence of acoustic softening and acoustic residual softening. (Fig. 2.16).

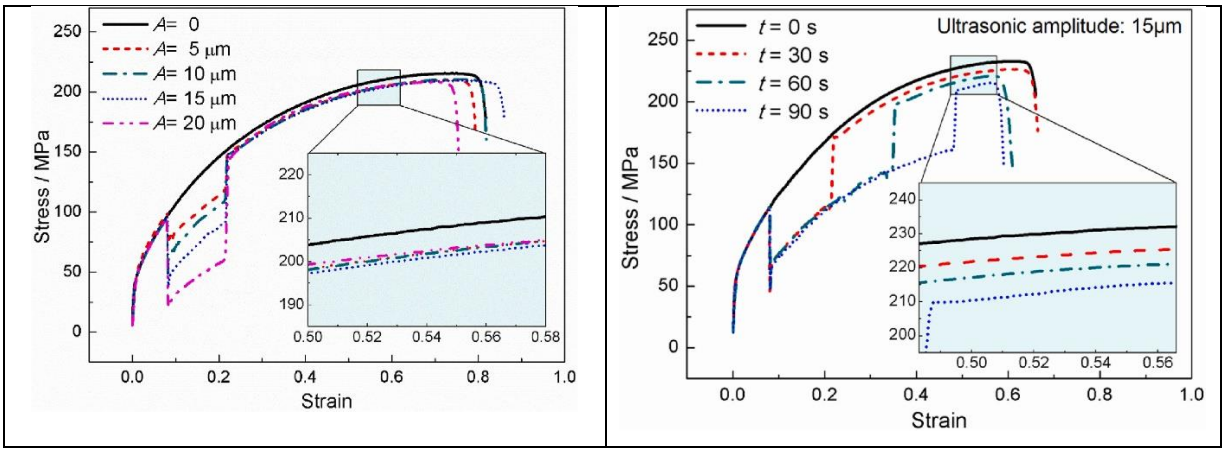

Fig. 2.19 Stress-strain diagrams of copper with different ultrasonic amplitudes (a) and sonication durations (b); Liu et al. (2022).

The ultrasonic-assisted micro-tensile test frame was developed by Kang et al. (2020) from an apparatus originally developed for testing single-crystal materials at Ohio State University. The system is mounted onto a vibration cancellation table to isolate environmental disturbance. A dogbone sample is constrained within grooves machined into two tensile grips, one connected to a magnetostrictive ultrasonic transducer and the other to a high spatial resolution linear actuator. The position of this moving grip is recorded using a capacitance displacement gauge, from which the engineering strain of the specimen can be calculated. A high-speed camera is mounted on the sample for in situ imaging of deformation, slip band formation, and crack initiation. The images are post-processed with Ncorr to obtain full-field displacement and true strain evolution during tensile tests. Displacement and strain mapping are then calculated by tracking subsets of the image in the initial state to a series of images taken during loading. 20 kHz ultrasonic vibration was applied in the study to investigate the effects of different test parameters on material flow stress. Two levels of ultrasonic vibration amplitudes, 1.0 μm, and 1.3 μm, and two levels of strain rate, 0.06/s, and 1/s, were studied. In situ infrared (IR) thermal imaging was performed with an IR camera mounted over the sample to evaluate the thermal effect of ultrasonic vibration. Commercially

available electrolytic tough pitch (ETP) copper with a purity of 99.9% in the tempered annealed condition was used in the study. Small-scale dogbone specimens were prepared from a 0.2 mm copper foil using wire electrical discharge machining (EDM) with an accuracy of 15 μm. Microstructure characterizations were performed with an optical microscope and EBSD analysis (Fig. 2.20).

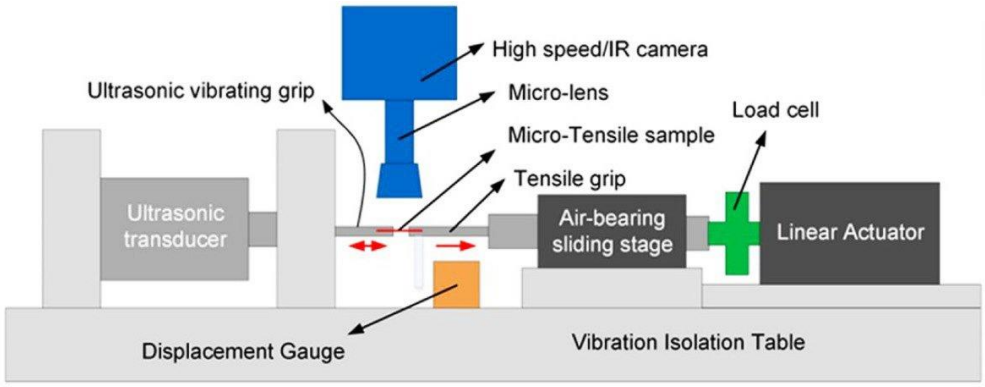

Fig. 2.20 Schematic illustration of the micro-tensile testbed.

Kang et al. (2020) conducted an electron backscatter diffraction (EBSD) analysis for copper plastically deformed in the ultrasound field. They revealed that ultrasonic vibrations promote preferential grain re-orientation and reduce internal misorientation within grains. In addition, the quantity of low-angle boundaries (the obstacles for plastic deformation in post sonicated state) is decreased in the ultrasonically tested circumstances (Fig. 2.21) compared to the same amount of deformation under unidirectional loading. This fact explains why the plastic flow in the post-sonicated states requires less stress value.

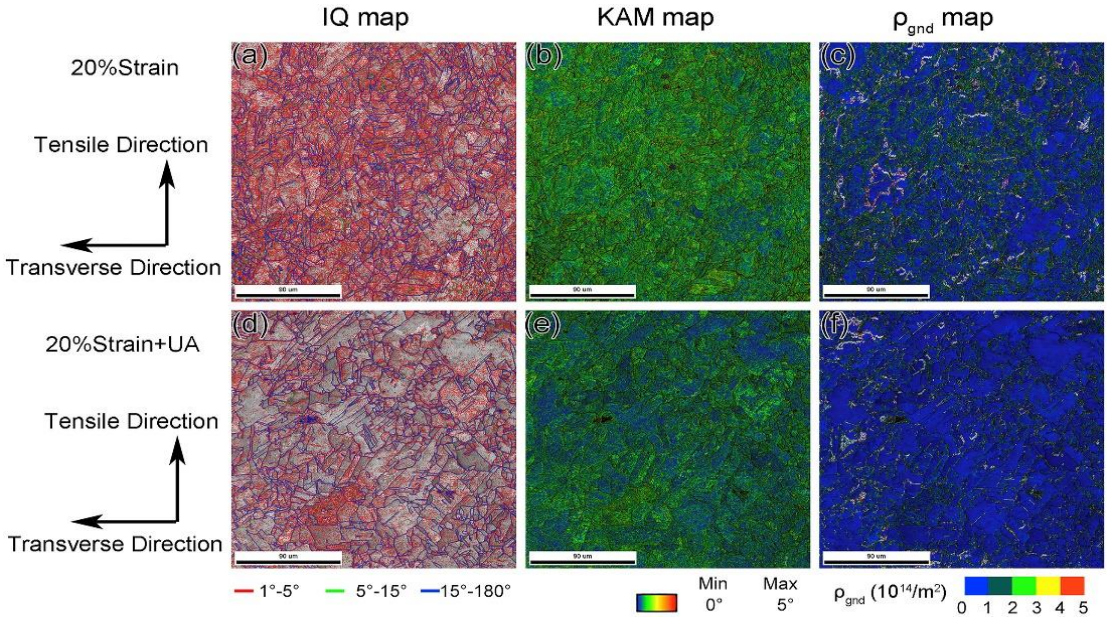

Fig. 2.21 EBSD results: (a), (b), (c) are image quality (IQ) map, average kernel misorientation (KAM) map, and geometrically necessary dislocation (GND) density map without ultrasound, respectively; (b), (d), (f) are the corresponding results with ultrasound, Kang et al. (2020).

Similar results were recorded by Lum et al. (2009) when utilizing ultrasound to superimpose Cu and Au wire bonding. They also explained residual softening by dynamic annealing and dislocation theory. Shao et al. (2021) summarize the above results: "The dislocation density reduction, grain rotation, and misorientation reduction are considered to be the reasons for the residual softening phenomenon."

Another mechanism responsible for the residual softening is twinning, primarily inherent in materials with low SFE. Zhou et al. (2017) examined the fraction of twinning boundaries, abundant in many metals with low stacking fault energy. They showed that ultrasonic vibration promotes the saturation of twinning and reduces the fraction of twinning boundaries. Since the twinning boundary is a hardening factor to titanium, the titanium sample exhibits a residual softening effect with fewer twinning boundaries (Fig. 2.22). As a result, Fig. 2.22 demonstrates that the development of plastic deformation occurs at lower stress values after the ultrasound is off. Again, one can see that the magnitude of the stress reduction after the ultrasonic action depends on two quantities: the ultrasound amplitude and the sonication time.

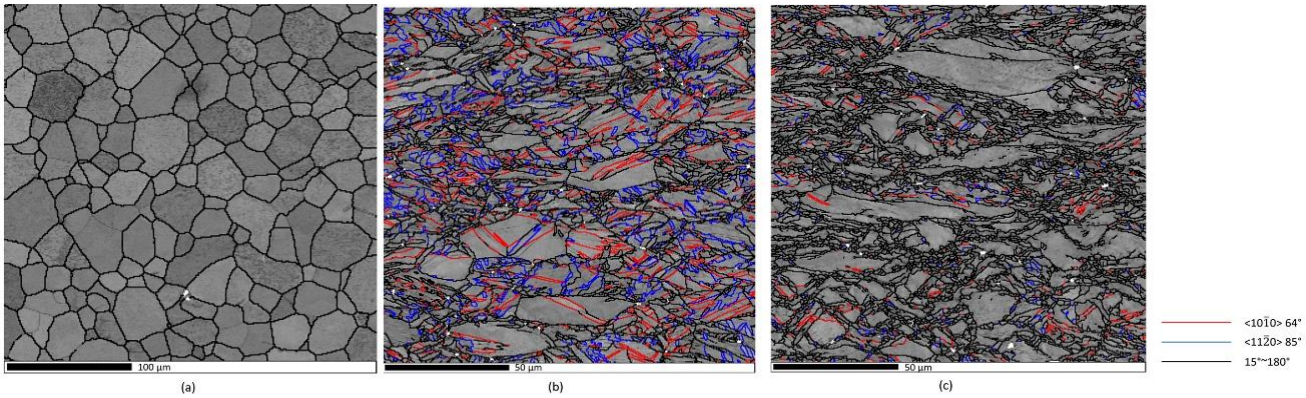

Fig. 2.22 Band contrast map for titanium with twinning boundaries of initial sample(a), compressed sample(b), and the sample compressed with ultrasound (c); Zhou et al. (2017).

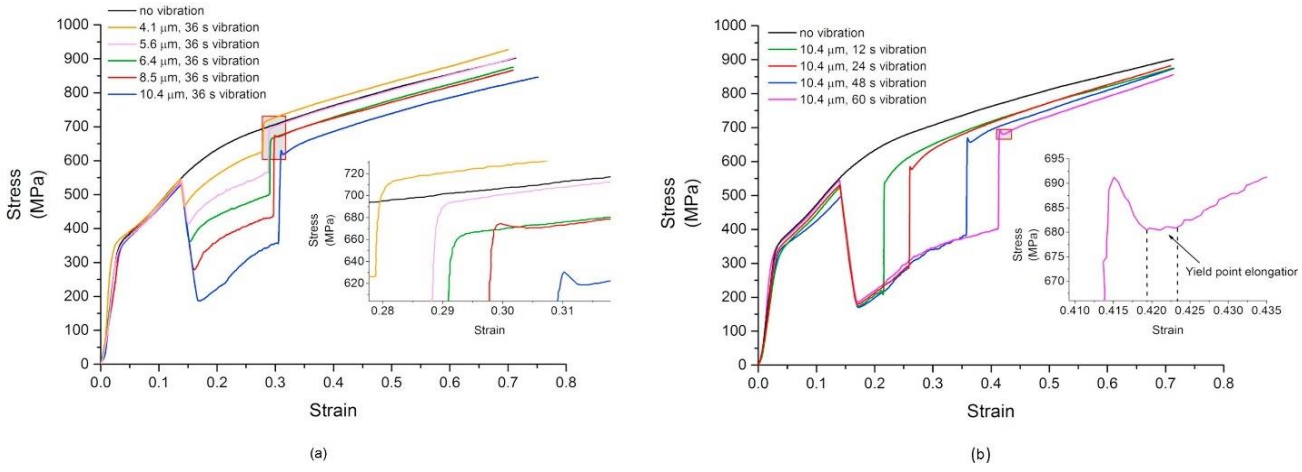

Fig. 2.23 Softening and residual effects of ultrasonic vibration with (a) different vibration amplitudes (b) with different vibration durations on samples of titanium, Zhou et al. (2017).

Recent theoretical research

The acoustic effects have been modeled using a variety of constitutive material theories. Based on the presumption that the absorption of acoustic energy is highly localized at dislocations and grain boundaries, Siddiq et al. (2011) proposed a phenomenological crystal plasticity model. They modified the plastic flow rule so that the critical resolved shear stress for each slip system is reduced in the presence of acoustic energy. A constitutive model based on the thermal activation of dislocation gliding was developed by Sedaghat et al. (2019), where the acoustic energy is included as a decrease of the activation energy. Deshpande et al. (2018) included the ultrasonic effect in their dislocation density evolution model, which predicts how dislocation density relates to the plastic shear strain rates.

Malygin (2000) proposed a stress superimposition mechanism, implying that ultrasonic waves activate blocked dislocations hardened under ordinary deformation and decrease stresses for further plastic deformation. In other words, this theory proposes that dislocations preferentially absorb ultrasonic energy, reducing the activation energy needed for dislocations to overcome lattice impediments and increasing their mobility, both of which contribute to a decrease in macroscale stress.

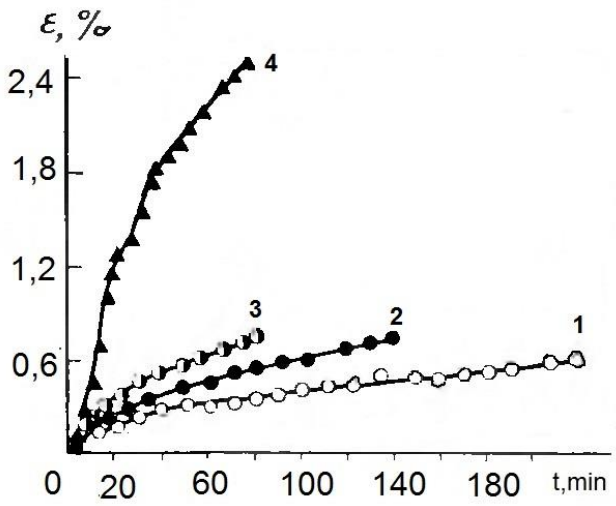

Fig. 2.24 Creep curves of aluminum at a temperature of 40°C and stress $\sigma_0 = 10$ MPa: 1 – ordinary creep 2 - 4 – ultrasound-assisted creep with oscillating stress amplitudes of $\sigma_m = 0.6$ MPa (2), $\sigma_m = 1.3$ MPa (3), $\sigma_m = 2$ MPa (4). (Kulemin, 1978)

2.5 Ultrasound-assisted creep

Like in the case of plastically deforming materials in the acoustic field, ultrasound intensifies the processes governing the development of creep deformation. According to Graff (2015), Tsimbalistyj and

Vlasenko (1983), and Kulemin (1978), the creep deformation coupled with ultrasound shows an increase in both primary and secondary portions (Figs. 2.24 and 2.25).

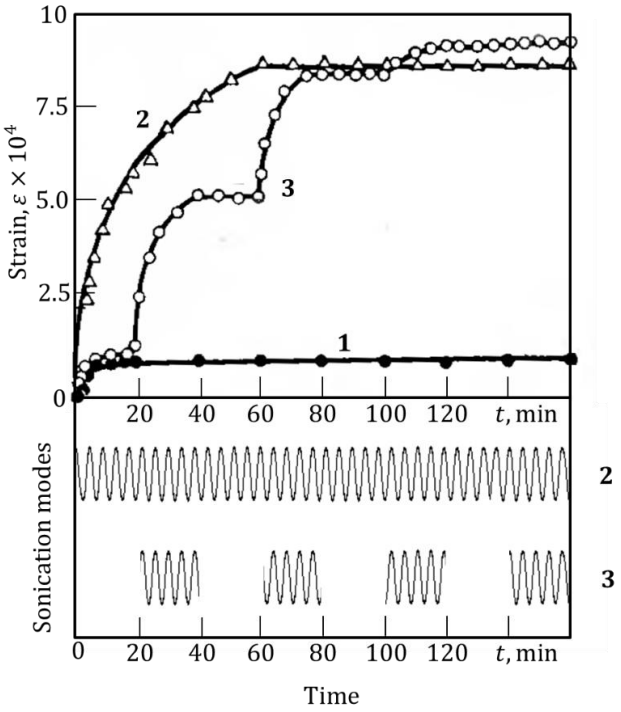

Fig. 2.25 Strain vs. Time curves of copper for ordinary (1) and ultrasound-assisted loading (2,3) (Kulemin, 1978). The creep diagrams are shown alone (without the initial plastic deformation)

Figure 2.25 shows strain-time diagrams for copper at 20℃ in uniaxial tension, $\sigma = 30$ MPa, obtained by Kulemin (1978). Curve **1** in Fig. 2.25 is an ordinary creep diagram under the action of static stress alone. Since the experiments were conducted at room temperature, the steady-state creep rate tends to be zero. Curve **2** depicts the development of deformation with time under the simultaneous action of the static and oscillating load (oscillating stress amplitude $\sigma_m = 2.6$ MPa). It is easy to see that the acoustic energy induces a significant increase in the primary creep deformation compared to the ordinary creep. At the same time, there is no change in the secondary creep rate, which can be attributed to the experiment's low temperature. However, Kulemin's experiments at higher temperatures show that ultrasound increases the secondary creep rate.

Kulemin (1978) studies were carried out on a specially designed installation. The basis of the installation was the АИМА-5-1 machine for testing materials for high-temperature creep, to one rod of which an ultrasonic magnetostrictive transducer / with a conical concentrator 2 fed from the УЗН- 10М generator was attached. The test sample 3 was screwed to the concentrator at one end in the form of a rod with an abruptly changing cross-section, the diameters of the ends $d_1 = 19$ mm, the diameter of the middle part was $d_2 = 7$ mm. The installation had an electric furnace to regulate the temperature of the sample. When vibrations were turned on along the length of the sample, a certain distribution of vibrational

displacement amplitudes was established. During the experiment, the amplitude of displacements along copper and aluminum samples was measured using a non-contact sensor. For the research, polycrystalline copper (99.9% Cu) was chosen, annealed for 5 hours in vacuum at 550°C. The length of the samples $21/2 - 96\ mm$. Polycrystalline aluminum (99.99% Al) was chosen for research. Before creep, all samples were annealed in vacuum at $T - 0.5\ Tm$ for 3 hours and then electropolished. The average grain size after annealing was $0.1\ mm$.

Another distinctive feature of ultrasound-assisted creep is an increase in the duration of its primary portion (≈ 60 min against 20 min for the ordinary creep). Finally, Curve **3** was obtained when the ultrasound with $\sigma_m = 2.6$ MPa is switched on periodically for 20-minute periods: [20-40], [60-80], and [100-120]. One can see that each time the ultrasound is on, the deformation begins to grow, but the values of deformation increments decay with the number of the ultrasound switches, and there comes the point when the ultrasound exerts no effect. Remarkably, the primary creep lasts for 60 seconds for continuous ultrasound and terminates at the end of the third 20-minute portion of the sonication. Another interesting result is that the total effect from the periodic action of ultrasound (3×20 min) is greater than when ultrasound acts continuously for 60 min.

To interpret/explain the results of the experiments, we utilize the dislocation mechanism of irrecoverable deformation. As well known, creep deformation develops mainly via dislocation climbs initiated by vacancy flows. The primary creep's driving force is energy stored in the material during active loading before the creep, and when this energy is exhausted, the material goes into a steady-state creep.

Despite numerous experimental and theoretical research on ultrasonic technology, the ultrasound mechanism is still controversial and requires further investigation. It can be summarized as:

(i) A stress superimposition mechanism proposed by Malygin (2000) implies that ultrasonic waves activate anchored dislocations hardened under ordinary deformation and reduce stresses needed for further inelastic deformation. However, according to Daud et al. (2007), one should avoid adding unidirectional and oscillatory stresses. For example, consider Fig. 2.26, where the creep rate of aluminum at $\sigma = 10$ MPa and $T = 40$℃ is shown as a function of additional static stress $\Delta\sigma$ (1) and ultrasonic stress amplitude σ_m (2). It is easy to see that, for example, the creep rate in the ultrasonic field with $\sigma + \sigma_m$ is about five times greater than that under the action of static stress $\sigma + \Delta\sigma$, where $\Delta\sigma = \sigma_m = 2.0$ MPa.

(ii) Deshpande et al. (2019) draw an analogy between the effects of hot deformation and ultrasound action, and they indicate that similar microstructure evolution can be observed when thermal energy is replaced with ultrasonic energy. As a result, numerous investigators (e.g., Lum et al. (2009) and

Huang et al. (2009)) suggest that ultrasonic vibration induces sufficient heat input to the sample to produce some softening of the microstructure.

(iii) Kulemin (1978) investigated the effect of ultrasound on creep in copper and germanium. The increase in creep rate was supposed to be attributable to the nucleation of point defects.

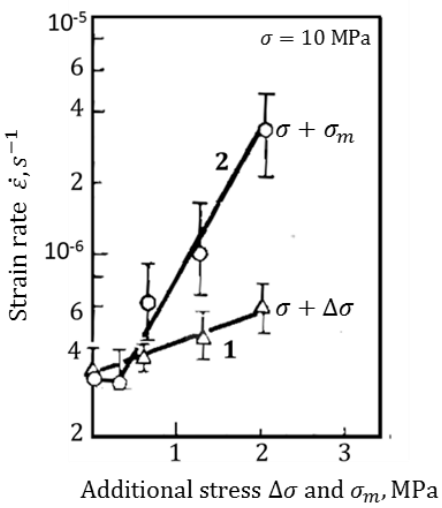

Fig. 2.26 Dependence of the strain rate of aluminum on the additional static loading (1) and the additional ultrasound stress amplitude (2) (Kulemin, 1978).

The greater creep in the acoustic field can be explained by the combined action of the factors proposed above, namely (i) the activation of blocked and hindered dislocation via the inflow of ultrasound-nucleated-vacancies, (ii) sonication boosts slips in the active slip systems and involve new ones, and (iii) ultrasound softens the material, similarly to heat energy. Now, the creep diagrams from Fig. 2.25 become more clear. Injecting acoustic energy into material with some deformation energy leads to an even more significant effect (compare curves **2** and **3** in Fig. 2.25). The increase in the number of defects involved in ultrasound-assisted creep necessarily entails the growth of time needed to transmit the material structure into an equilibrium state inherent to the steady-state creep (about 20 min for the ordinary creep **1** and above 60 min for the ultrasound-assisted creep **2**). The fact that the creep increments decay with the number of ultrasonic actions (sonication for 140-160 minutes period results in no effect on curve **3** good correlates with the peculiarity of the defects nucleated in the ultrasonic field shows a saturation of their number with time (see Fig. 2.8).

2.6 The effect of ultrasound on the strain-hardened metals

Another effect of ultrasonic vibrations on the deformational characteristics of materials is the recovery/softening of plastically deformed metals.

Kulemin's (1978) X-ray investigation studied the evolution of interference patterns for plastically prestrained aluminum specimens in the ultrasonic field at home temperature (Fig. 2.27). Clear interference spots with a 0.3–1.0 mm radius on the annealed specimen fade out to 8 mm and 2-3 mm in the azimuthal and radial directions due to plastic deformation. After the ultrasound action, there is a reduction in interference spot blurring in both the radial and polar directions, which attests to the relaxation of second-kind stresses caused by the elastic distortions of crystalline grids during plastic deformation. The reduction in dislocation density due to the sonication of plastically hardened aluminum at 20°C is shown in Fig. 2.28. As can be seen, as a function of the sonication time, the dislocation density for the deformed material monotonically declines to its original value (annealed state).

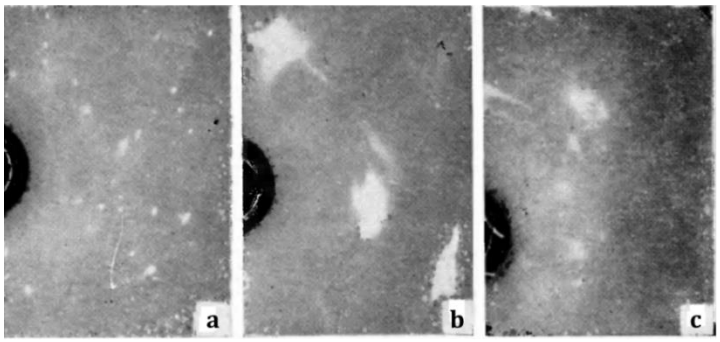

Fig. 2.27 X-ray micrograph of aluminum specimen – a) annealed state, b) plastic deformation of 5 %, c) sonication of the deformed specimen; oscillating stress amplitude 16 MPa, duration 100 min, Kulemin (1978).

For the research, Kulemin chose polycrystalline aluminum (aluminum content 99.9%) annealed at $T = 0.5\ T_m$, and then deformed by cold rolling or uniaxial tension on an Instron machine by 5%. The samples were half-wave rods with a cross-section of $12\text{x}12\ \text{mm}^2$. After deformation, some of the control samples were subjected to isothermal exposure at various temperatures (up to the recrystallization temperature), and the other part was exposed to ultrasound at the same temperatures. The sonicated samples were heated to the appropriate temperatures due to the absorption of sound energy in their material. When exposed to ultrasound at room temperature, the samples were cooled with running water to avoid heating.

One of the possible temporary mechanisms responsible for stress relaxation and material recovery is polygonization when dislocations arrange into low-energy configurations. The plastically deformed lattice is realigned into blocks free of stress and separated by borders made up of the dislocations of one sign. The dislocations must climb parallel planes and leave their slip planes to form the polygonized substructure. The dislocation climbs require active vacancy inflow, which can be stimulated by high thermal energy (for example, in elevated-temperature creep or during annealing). Since the results from Figs. 2.24 and 2.25 were obtained at room temperature, the ultrasonic energy alone may be considered

responsible for the material recovery via polygonization. This suggestion is consistent with the well-known fact that sonication is characterized by an abundance of point defects (vacancies). Fig. 2.29 supports the idea of the dislocation-climb nature of ultrasonic recovery. Indeed, the plastic deformation's straight slip lines (Fig. 2.29a) are divided into several intersecting wavy lines (Fig. 2.29b).

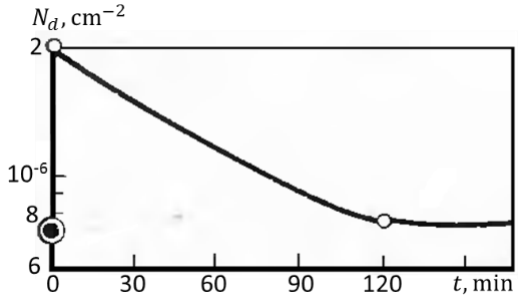

Fig. 2.28 Dislocation density vs. sonication time plot for aluminum at vibrating stress amplitude 16 MPa, initial plastic deformation 5%; Kulemin (1978).

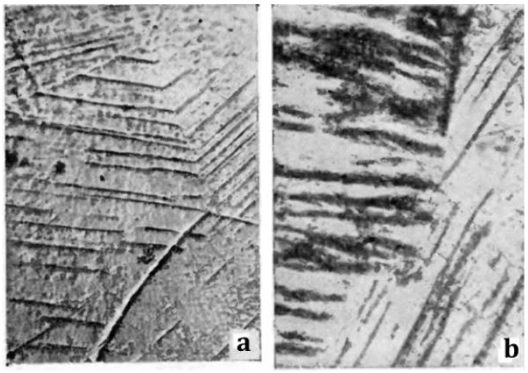

Fig. 2.29 Slip lines on the surface of aluminum specimen – a) after plastic deformation, b) after the sonication of the plastically deformed specimen, t = 20°C. Î 400 Kulemin (1978)

With the intensity of the ultrasonic recovery, the following can be summarized (Kulemin, 1978, Blagoveshchenskii, V., Panin, 2007):

(i) there is a lower limit for the oscillating stress (σ_m) beneath which the recovery effect is not observed (for example, while $\sigma_m = 4.3$ MPa and $\sigma_m = 5.6$ MPa gives no changes in the hardening decrease, $\sigma_m = 8.4$ MPa already yields the recovery effect (Kulemin, 1978);

(ii) the increase in σ_m leads to a much steeper decrease in the hardness/yield strength of the strain-hardened material;

(iii) at a given value σ_m, the acoustic energy causes more intensive recovery for more significant plastic deformations – the ultrasound-assisted recovery mechanisms accelerate at greater deformation energy cumulated in the material;

Consider the experimental results of Zohrevand et al. (2021) for 304SS and 316SS alloys. Tensile specimens were initially strained to 10%, and after unloading, the samples were sonicated with the input power of 300 W for 4 min.

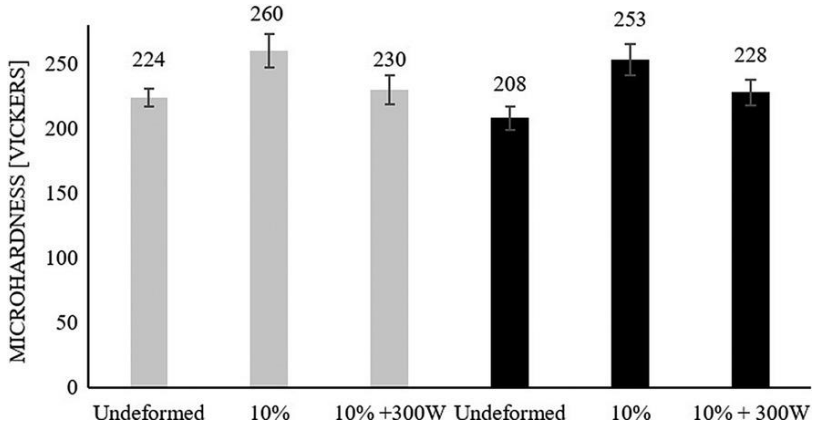

Fig. 2.30 Microhardness test results for 316SS (gray columns) and 304SS (black columns), Zohrevand et al. (2021).

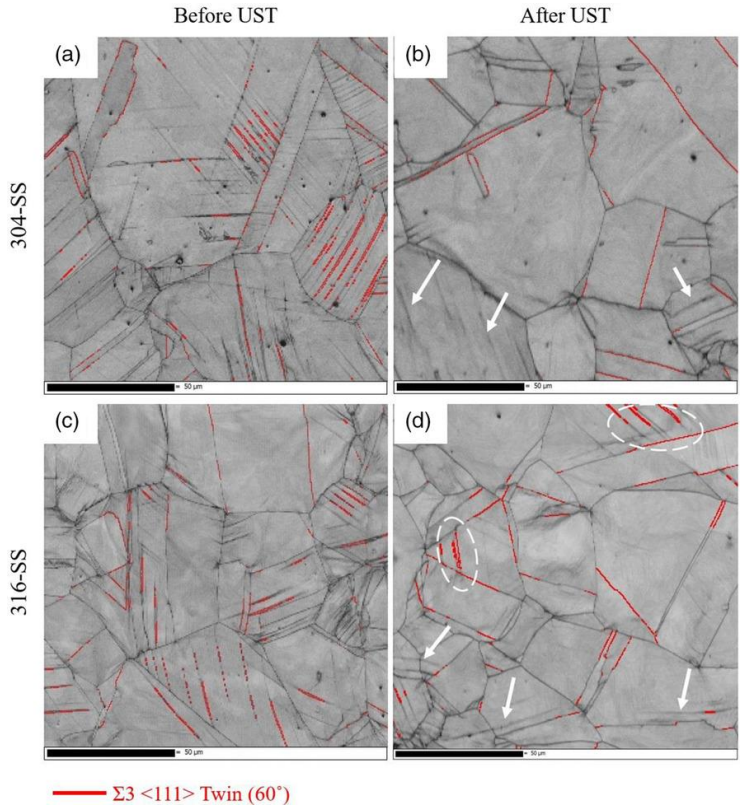

Fig. 2.31 Twining boundary map for steels 304SS and 316SS; (a and c) plastically deformed specimens, (b and d) after the ultrasound action (Zohrevand et al., 2021).

The following conclusions can be made from this research. 1) Microhardness tests evidently show the softening effect of ultrasound on the strain-hardened structure (Fig. 2.30). 2) The XRD peak shifting to lower angles after the ultrasonic action reflects the relaxation of tensile residual stress in both alloys. 3) Active de-twining processes are observed during sonication, which can be attributed to the oscillatory shear stress induced by the ultrasonic vibration (Fig. 2.31). 4) Low-strain regions formed on triple junctions and near the grain boundaries imply the static recrystallization in the 316SS alloy during ultrasonic irradiation (Fig. 2.32).

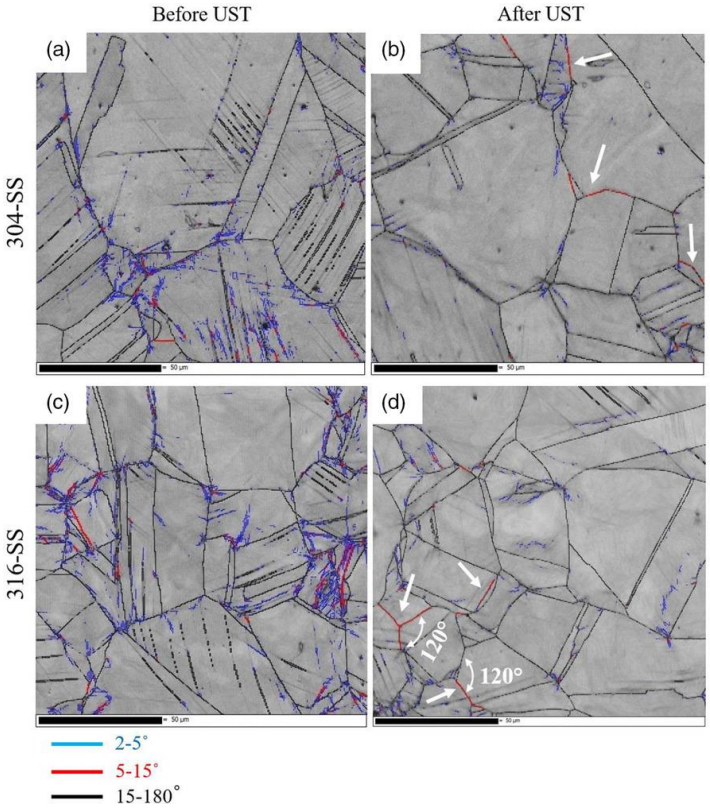

Fig. 2.32 The grain boundary map for 304SS and 316SS; (a and c) plastically deformed specimens, (b and d) after the ultrasound action (Zohrevand et al., 2021).

2.7 The effect of ultrasound on the phase transformations in shape memory alloys

Today Shape Memory Alloys (SMAs) are already commercially applied in many technical fields. SMAs have been developed since the early 1960s, and since then, they have been successfully used for medical (Bansiddhi et al. 2008, Morgan 2004 and Sun et al. 2012), robotic (Kim et al. 2006, Qin et al. 2004 and Wang et al. 2008), aerospace (Hartl et al. 2007, 2010a and 2010b), and automobile applications (Bellini et al. 2009 and Stoeckel, 1990).

The superior property of SMA is that it can go through solid-state phase transformations, meaning it can be stretched, bent, heated, cooled, and still remember its original shape. SMAs are widely used for medical implants due to their kink resistance, stress constancy, high elasticity, and corrosion resistance.

If we speak of electronic devices and robotic systems, SMA actuators, sensors, and controllers have drawn significant attention and interest due to their unique properties and are expected to be equipped in many modern vehicles at competitive market prices (Jani et al. 2014). The essential advantage is that active elements (e.g., SMA wire or spring) can be deformed by applying minimal external force and retain their previous form when subjected to certain stimuli such as thermomechanical or magnetic changes. In aerospace, SMA release devices can be actuated slowly, avoiding satellite shock failures. This application is essential for satellites because it can also be used for 'microsatellites' since compact separation devices with minimal SMA release triggers can be made (Wanhill et al. 2017).

In this thesis, I deal with the following two cases:

(i) The effect of ultrasound on the austenite transformation.

(ii) Pseudoelastic deformation (martensite transformation) in ultrasonic field.

Ultrasound-assisted austenite transformation

As mentioned above, SMAs can recuperate their original shape while heating above specific critical temperatures (shape memory effect). In other words, they can recover a large inelastic deformation or create high recovery stress on heating within the temperature range of martensitic transformation. However, heating the SMA elements cannot be carried out for many applications. Other ways to initiate shape memory effects may be applied in these cases. It is known that strain recovery may be initiated by neutron irradiation, hydrostatic pressure, and ultrasonic action (Belyaev et al. 2014). The last method is the most attractive because ultrasonic vibration does not require expensive equipment like other methods.

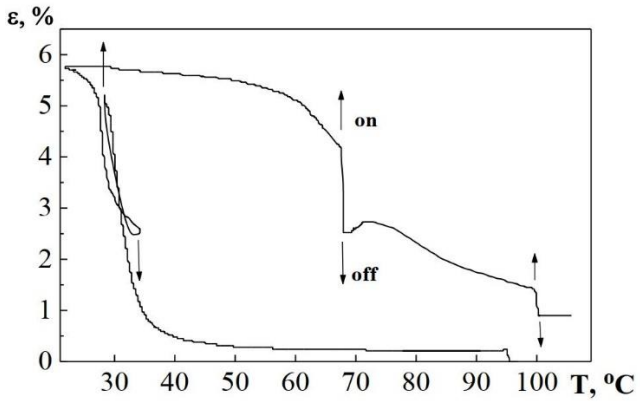

Fig. 2.33 State diagram of NiTi alloy in deformation-temperature coordinate. The sample is subjected to uniaxial tension $\sigma = 30$ MPa. The arrows show the moments of switching-on (↑) and switching-off (↓) of ultrasonic vibrations. (Rubanik et al. 2008).

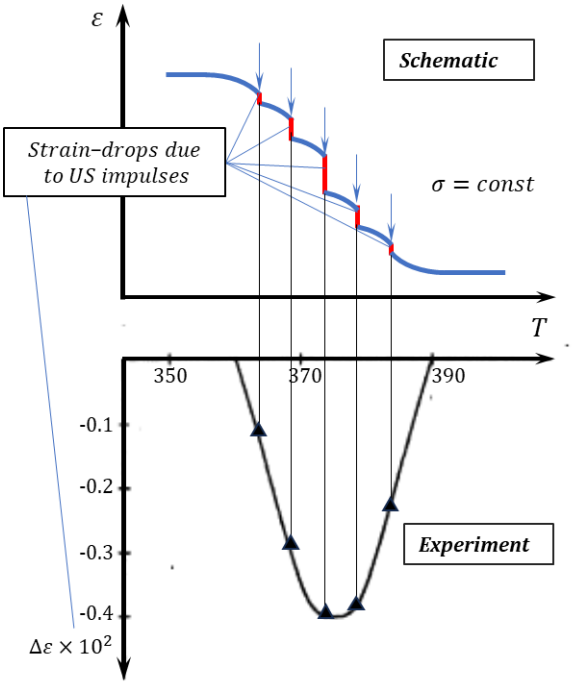

Fig. 2.34 Phase transformation in Ni-Ti alloy with ultrasonic impulses and the deformation drop distribution. The amplitude of ultrasonic deformation is 5×10^{-5} , $\sigma = 100$ MPa $=$ const. Steckmann et al. (1999).

Experimental observations (Figs. 2.33 and 2.34) on effect of ultrasonic impulses on the reverse (austenite) transformation – the deformation recovery (decrease) is considered on heating at constant stress – can be summarized as follows (Klubovich et al. 1997, Rubanik et al. 2008, Buchelnikov et al. 2004, Steckmann et al. 1999, Breczko et al. 1999 and Bao et al. 2013):

I. Ultrasonic vibrations impulsively added to austenitic transformation result in negative strain jumps. In other words, acoustic energy can initiate strain variations of SMA. The lattice is very soft during transformation, and the phase boundaries are easily movable. In this case, any external action, for instance, alternate stress, results in the appearance of an additional quantity of preferably oriented domains, which leads to a further strain variation.

II. The magnitude of the strain jumps increases with the ultrasonic vibration amplitude.

III. The effect of insonation strongly depends on the moment the ultrasound is applied. Acoustic energy has no effect if it acts outside the austenite transformation temperature range. Further, the magnitude of the ultrasound-induced strain jumps is not distributed uniformly within the austenite transformation temperature range. This phenomenon reaches its maximum if the alternate stresses are applied approximately in the middle of the temperature range of phase transformations. It can be explained by the fact that the number of phase boundaries reaches its maximum when half of the alloy is transformed into the austenite phase (Belyaev et al. 2014), and ultrasound manifests itself in full force.

IV. It was found that the series of ultrasonic impulses led to the finish temperature being less than during conventional heating. Since acoustic energy boosts the transformation processes, it is logical to assume that they sooner reach their completeness. In other words, the temperature needed to finish the transformation is partially compensated by ultrasound heating.

V. After switching of ultrasound, the further realization of SME occurs according to the reverse transformation kinetics. However, immediately after the ultrasound is off, some "backsliding" in austenitic deformation, a slight increase of deformation, is observed; 67-77°C temperature range in Fig. 2.33. This aftereffect is assumed to be due to a) the decrease in temperature after ultrasound is off and b) the action of ultrasound which "left a trail" in the form of ultrasound-assisted defect conglomeration, reducing the development of the phase transformations. Therefore, while the central portion of acoustic energy converts irreversibly into the phase deformation increment, some fraction of it recovers.

Experimental investigations clearly show that stress and temperature are equal stimuli for initiating austenite transformations, i.e., the same mechanical effects can be achieved by employing both stress and temperature. Since ultrasound is a carrier of both these effects – alternating stress and increase in temperature caused by them – the physical substantiation of the phenomena observed above can be summarized as follows (Klubovich et al. 1997, Rubanik et al. 2008, Buchelnikov et al. 2004, Steckmann et al. 1999, Breczko et al. 1999 and Bao et al. 2013):

I. The variation (increase) in austenite deformation can be explained by ultrasonic heating of the sample due to ultrasound waves' energy dissipation.

II. Acoustic energy increases the mobility of interfaces (phase and domains) by decreasing the efficient friction force caused by alternate stresses.

III. The superposition of alternate stresses induces the movement of interface and martensitic domain boundaries (within the temperature range of reverse martensitic transformations).

Ultrasound-assisted martensite transformation

Consider the ultrasound-assisted $\sigma \sim \varepsilon$ diagram of Ni-Ti-Re alloy in uniaxial stress at constant temperature recorded by Steckmann et al. (1999). While line **1** in Fig. 2.35 illustrates the ordinary pseudoelastic course of deformation, line **2** is obtained when unidirectional and vibrating stresses act

simultaneously from the beginning of the experiment. It is simple to notice the following characteristics of the pseudoelasticity in combination with ultrasound:

(j) The initial and middle portions of line **2** run beneath line **1**, and the inelastic deformation in the acoustic field starts at a lower stress than for the static loading (compare 48 MPa for line **2** to about 100 MPa for line **1**).

(ii) Line **2** crosses line **1** at the deformation of about 6.3% and has a steeper slope angle than line **1**, i.e., greater stress values are required at the final stage of martensite transformation.

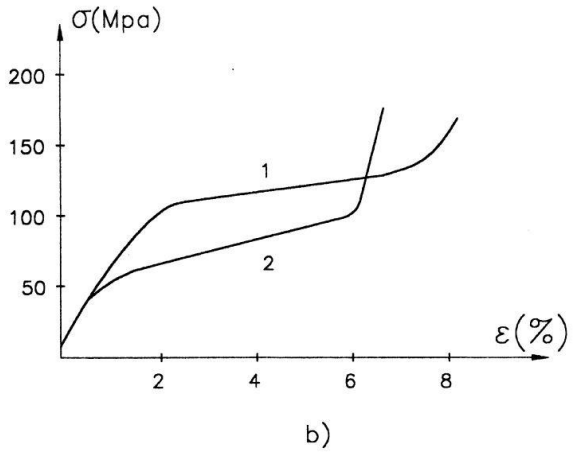

Fig. 2.35 Pseudoelastic deformation of Ni-Ti-Re alloy in uniaxial tension, temperature 283 K; **1** – without ultrasound, **2** – under superimposed ultrasound with the deformation amplitude of $\varepsilon_m = 2 \times 10^{-4}$; Steckmann et al. (1999).

Steckmann et al. (1999) used rectangular cross-sectioned samples for the study. The samples were aged in vacuum for 2 hours at $500°\ C$ after quenching from $1000°\ C$ for 20 minutes in water. An ultrasonic generator supplied ultrasonic vibrations to both sides of the sample using a magnetostrictor with step-like acoustic horns. The left magnetostrictor was fixed, while the right one could move easily along guide skids. The moving vibrator was stressed by weight for thermal cycling studies and linked to an electric motor for a fixed rate of deformation. The sample and sample holders were placed in a special thermostat chamber to maintain temperature. The amplitude of ultrasonic vibrations was controlled by a magneto dynamic system calibrated by a microscope. The applied stress was measured using a strain gauge attached to an elastic element of the lead, and elongation was controlled by an inductance transducer.

The kinetics investigation of the direct and reverse thermoelastic phase transformation of the TiNi samples in ultrasonic field was carried out by Rubanik et al. (2008), at fixed static stress on a designed experimental bench. This bench allowed realizing the automatic control of length and temperature changes in different sample points with subsequent computer data processing considering time dependence. The sample was fixed in the holders of the bench. One holder served as a waveguide and

static load was applied through the other one. The temperature was controlled by a chromel–alumel thermocouple fixed to the sample with the help of spot welding. Heating was performed at a rate of $1\ \mathrm{K/min}$. Within the temperature range from 15 to $150°\ \mathrm{C}$. An induction sensor was used for extension measuring. The tests were performed with Ti–50.4 at.% Ni wire samples 120mm long and 0.50mm in diameter. Characteristic temperatures measured by differential scanning calorimetry were: $\mathrm{As} = 50°\ \mathrm{C}$, $\mathrm{Af} = 76°\ \mathrm{C},\ \mathrm{Ms} = 30°\ \mathrm{C},\ \mathrm{Mf} = 21°\ \mathrm{C}$. The procedure of tests was the following. The wire sample in the high-temperature austenite state was subjected to load with subsequent cooling. In the temperature range $\mathrm{Ms}-\mathrm{Mf}$ mechanical ultrasonic vibrations were produced in the samples impulsively. The system was sustained in resonance at a frequency of 22.2 kHz and a vibrational amplitude of 5m. After cooling, the sample was brought into austenitic condition by heating in loading or unloading condition. In the temperature range $\mathrm{As}-\mathrm{Af}$ ultrasonic vibrations were produced in the sample impulsively upon heating. Deformation, temperature, and timing were measured during the ultrasound influence. The kinetics investigation of reverse transformation at ultrasonic shape recovery was carried out on the Ti–50.4 at.% Ni belt 0.75mm thick, 2.1mm wide, and 100mm long. The transformation temperatures were $\mathrm{As} = 30°\ \mathrm{C}, \mathrm{Af} = 45°\ \mathrm{C}, \mathrm{Ms} = 37°\ \mathrm{C}, \mathrm{Mf} = -3°\ \mathrm{C}$. A preliminary 3.4% residual strain was set to the sample using uniaxial tension at $20°\ \mathrm{C}$. Then we obtained full shape recovery with the help of ultrasound.

Experimental studies (Rubanik et al. (2003, 2008), Mercier et al. (1979), Breczko et al. (1999), Steckmann et al. (1999), Belyaev et al. (2014), Buchelnikov et al. 2004, Klubovich et al. (1997), Samigullina et al. (2018)) describe the mechanisms driving the ultrasound-assisted martensite transformation as follows:

(i) Ultrasound increases the mobility of interfaces (phases and domains) by decreasing the efficient friction force caused by alternate stresses.

(ii) The superposition of alternate stresses induces the movement of defects (dislocations and twins) and martensitic domain boundaries (within the temperature range of martensitic transformation). In addition, acoustic energy results in the appearance of an additional quantity of preferably oriented domains that leads to further strain variation.

Further, Malygin's (2001) and Sapozhnikov's (1996) investigations show that the superimposed ultrasound can favor increasing or decreasing the static stress needed to develop pseudoelastic deformation. This is because, at the initial stage of pseudoelastic deformation, the oscillatory stress causes the fraction of the martensite phase to increase during positive half-cycles, which leads to an additional deformation and, hence, to a decrease in the applied stress. In the case of large stresses, the effect of the oscillatory stress is more significant during negative half-cycles leading to a decrease in the

volume fraction of martensite and, hence, an increase in the applied stress. Therefore, the sign of the effect of acoustic energy on the development of martensite transformation varies during pseudoelastic deformation. This result correlates with that indicated by Steckmann et al., (1999), where the ultrasound-assisted stress-strain diagram (line **2** in Fig. 2.35) has a greater hardening coefficient at the final stage of the transformation and, therefore, crosses the ordinary diagram.

Using relationships obtained by Lichachev and Malinin (1993) in the framework of the Structural-analytic theory of elasticity, Rusinko A and Rusinko K. (2012) developed a model to describe phase transformation in terms of the Synthetic theory.

Summary

The first steps in modeling ultrasonic effects were made in terms of the synthetic theory of inelastic deformation: a new term, ultrasonic defect intensity, is introduced into the constitutive relationships, Rusinko (2011). In this form, the theory catches the temporary ultrasonic softening alone when the ultrasound is superimposed from the very beginig of loading. At the same time, it does not cover the ultrasound-induced stress drops on the stress~strain diagram, acoustic residual hardening effects, and phenomena occurring at ultrasound-assisted creep and phase deformation

My research within this dissertation focuses on the further extension of synthetic theory to model the peculiarities of metal deformation in the acoustic field indicated in points 2.3-2.6.

Chapter III. The synthetic theory of inelastic deformation

3.1 Basic principles

The analytical description of the phenomena listed in the previous chapter is presented in terms of the synthetic theory of inelastic deformation outlined in Rusinko, A. & Rusinko, K.'s monography (2011). The synthetic theory incorporates the Batdort-Budiansky slip concept (Batdorf & Budiansky, 1949) and the Sanders (1954) flow theory and falls within the category of models for strain-hardened materials.

The synthetic theory works in the Ilyushin three-dimensional stress and strain deviator space (Ilyushin, 1963), $\mathcal{S}^3$ and $\mathcal{E}^3$ respectively. The components of the stress and strain vector $\vec{\boldsymbol{S}} = S_i\vec{\boldsymbol{g}}_i$ and $\vec{\boldsymbol{e}} = e_i\vec{\boldsymbol{f}}_i$ (the vectors $\vec{\boldsymbol{g}}_i$ and $\vec{\boldsymbol{f}}_i$ are unit vectors; they are coaxial but have different dimensions) can be defined as follows:

$$S_1 = \sqrt{3/2}\,S_{xx}, \quad S_2 = S_{xx}/\sqrt{2} + \sqrt{2}S_{yy}, \quad S_3 = \sqrt{2}S_{xz}, \tag{3.1.1}$$

$$e_1 = \sqrt{3/2}\,e_{xx}, \quad e_2 = e_{xx}/\sqrt{2} + \sqrt{2}e_{yy}, \quad e_3 = \sqrt{2}e_{xz}, \tag{3.1.2}$$

where S_{ij} and e_{ij} $(i, j = x, y, z)$ denote the stress and strain deviator tensor components. These are:

$$S_{ij} = \sigma_{ij} - \sigma\delta_{ij}, \tag{3.1.3}$$

$$e_{ij} = \varepsilon_{ij} - \varepsilon\delta_{ij}, \tag{3.1.4}$$

where δ_{ij} is the Kronecker delta,

$$\sigma = \frac{1}{3}\sum_{k=1}^{3}\sigma_{kk}, \tag{3.1.5}$$

$$\varepsilon = \frac{1}{3}\sum_{k=1}^{3}\varepsilon_{kk}\,. \tag{3.1.6}$$

The length of the vector $\vec{\boldsymbol{S}}$ is related to the second scalar invariant J_2 of the stress deviator tensor as

$$\left|\vec{\boldsymbol{S}}\right| = 2\sqrt{3}J_2. \tag{3.1.7}$$

Like the slip concept, the synthetic theory has a two-level nature, i.e., macro deformation is affected by the processes occurring on the micro level of the material. In the case of plastic or creep flowing, deformation at a point of the body (macrodeformation) is calculated as a sum (three-fold integration) of plastic shifts in active slips systems (microdeformations):

$$\vec{\boldsymbol{e}} = \iiint_V \varphi_N \vec{\boldsymbol{N}} dV. \tag{3.1.8}$$

In Eq. (3.1.8), φ_N – plastic strain intensity – is an average measure of plastic deformation within one slip system, which, according to the Schmidt law, takes place if the resolved shear stress exceeds the material yield strength. The orientation of the slip system is defined through the unit vector $\vec{\boldsymbol{N}}$. dV is an elementary set of slip systems involved in the plastic flow.

Yield criterion

In the framework of the synthetic theory, following Sanders's ideas, we work not with a yield surface itself but with its tangent planes, i.e., the yield surface is treated as an inner envelope of the tangent planes. Therefore, the von-Mises yield criterion, which is adopted in terms of the synthetic theory,

$$S_1^2 + S_2^2 + S_3^2 = S_S^2, \tag{3.1.9}$$

is treated as a set of equidistant planes in all directions (Fig. 3.1a); $S_S = \sqrt{2/3}\,\sigma_S$, where σ_S is the yield strength of material in uniaxial tension.

Hardening rule

During loading, the stress vector moves (shifts) at its endpoint (load point) a set of planes from their initial position. The movements of the planes located at the endpoint of the vector $\vec{\boldsymbol{S}}$ are translational, i.e., the plane orientations remain unchangeable. Those planes which are not at the endpoint of the vector $\vec{\boldsymbol{S}}$ remain unmovable.

The plane's displacement at the stress vector's endpoint symbolizes the development of plastic microdeformation within the corresponding slip system. Figs. 3.1b and 3.2 show the loading surface for the case when the loading trajectory is a straight line (proportional loading). It consists of two parts: a) a sphere that is the inner envelope of stationary planes and b) a cone whose generators are formed by the boundary planes shifted by the vector $\vec{\boldsymbol{S}}$. The planes shifted by the stress vector are located on the top of this cone.

The loading surface's transformation described above has a great advantage over the theories where the loading surface kinetics is prescribed in advance.

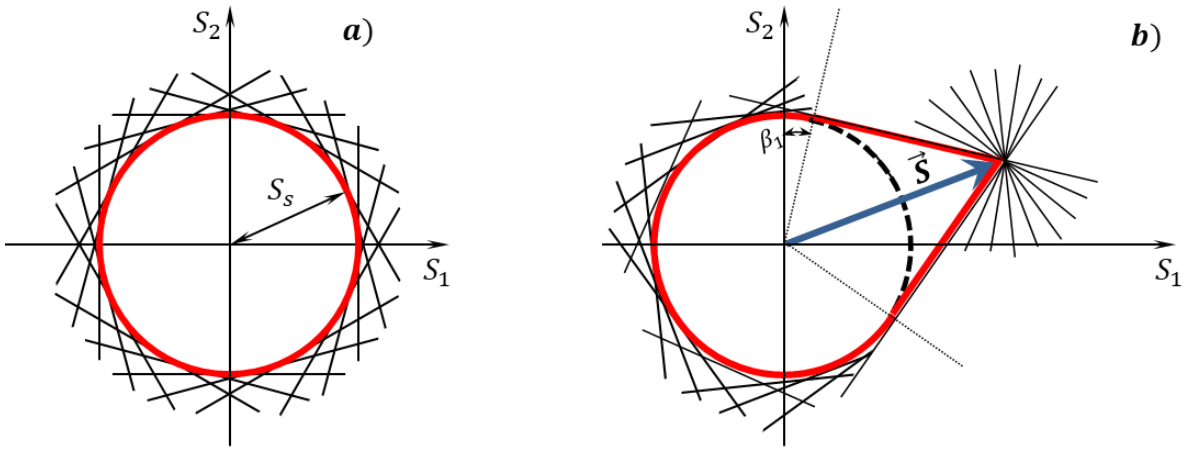

Fig 3.1 Yield and loading surfaces in S_1-S_2 coordinate plane.

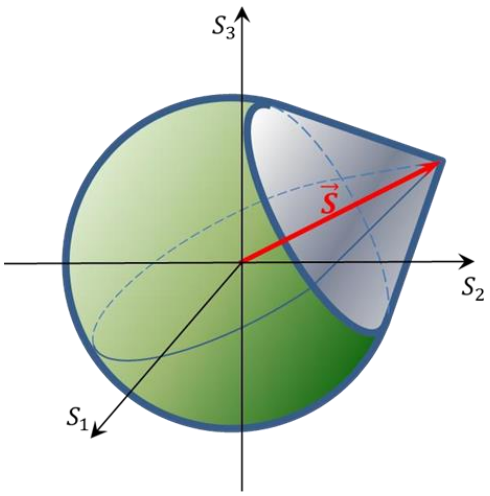

Fig. 3.2 Loading surface in $\mathcal{S}^3$ (planes are not shown).

The position of the planes is defined via their distances (H_N) and unit normal vectors ($\vec{N}$) as shown in Fig. 3.3.

A brief word about the angle λ. Even though we work with the condition $\vec{S} \in \mathcal{S}^3$, the planes tangential to the five-dimensional yield surface must also be considered. Consider Fig. 3.4 where, for simplicity, the yield surface in $\mathcal{S}^5$ is shown as a sphere, and its projection in $\mathcal{S}^3$ is a circle. To distinguish between the plane tangential to the yield surface in $\mathcal{S}^3$ (red) and that from $\mathcal{S}^5$ (blue), the angle λ is introduced.

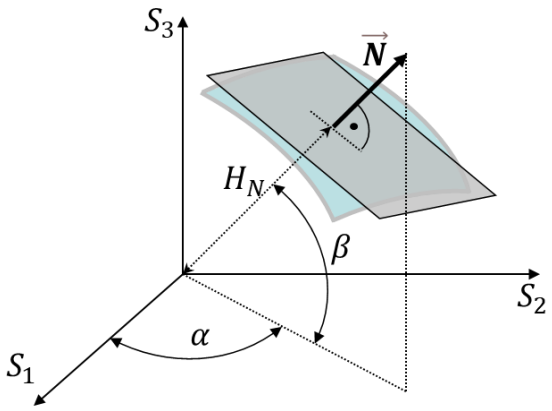

Fig. 3.3 Orientation of $\vec{N}$ in $\mathcal{S}^3$.

The coordinates of the unit vector $\vec{N}$ in $\mathcal{S}^3$ are defined through spherical angels α, β, and λ as follows (Rusinko, A and Rusinko, K., 2011)

$$N_1 = \cos\alpha \cos\beta \cos\lambda\,, \qquad N_2 = \sin\alpha \cos\beta \cos\lambda\,, \qquad N_3 = \sin\beta \cos\lambda. \tag{3.1.10}$$

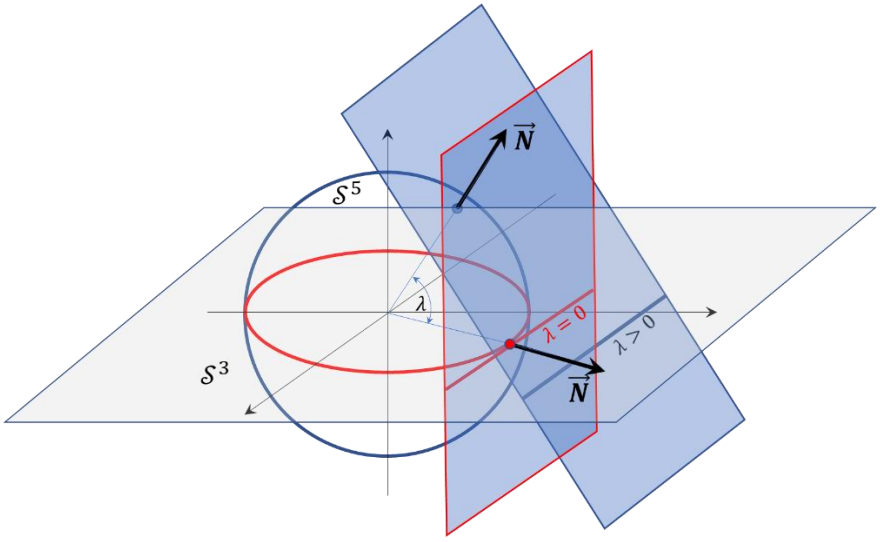

Fig. 3.4 Interplay between the tangent planes from $\mathcal{S}^5$ and $\mathcal{S}^3$.

Fig. 3.5 demonstrates the notions presented above for the case of one plane. It is assumed that an elementary plastic strain vector is perpendicular to the plane translated by the stress vector. The fact that a tangent plane is located at the endpoint of the stress vector $\vec{S}$ is expressed by the following relationship:

$$H_N = \vec{S} \cdot \vec{N}. \tag{3.1.11}$$

The scalar product $\vec{S} \cdot \vec{N}$ determines the resolved shear stress acting within one slip system. It is clear that the plane distance H_N reflects the hardening of the material because the greater H_N is, the grater $\vec{S}$ is needed to reach the plane.

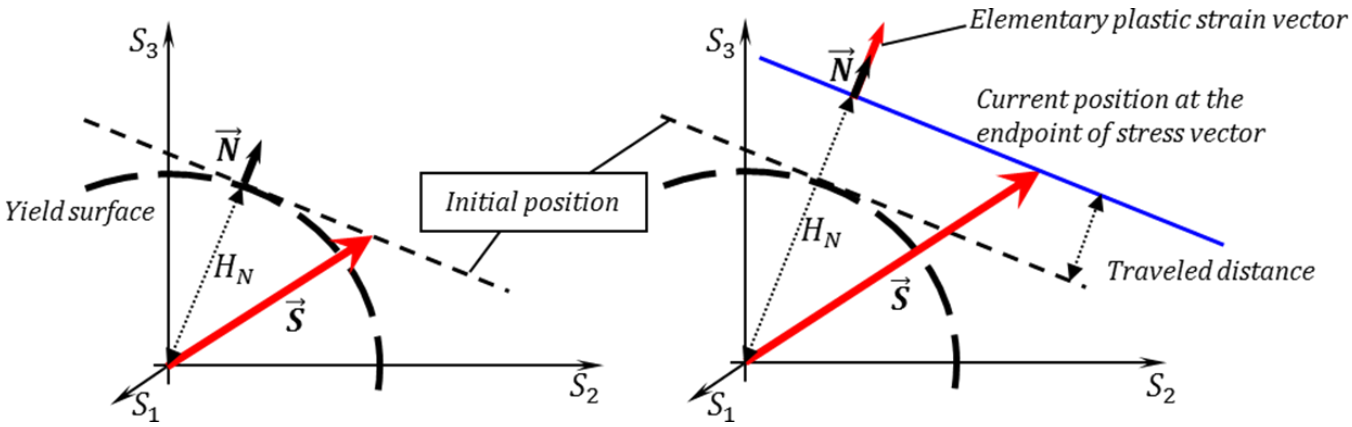

Fig. 3.5 Movement of tangent plane at the endpoint of stress vector.

The elementary set of planes displaced during infinitesimal increment in load is determined by the elementary volume dV standing in Eq. (3.1.8):

$$dV = \cos\beta \, d\alpha d\beta d\lambda. \tag{3.1.12}$$

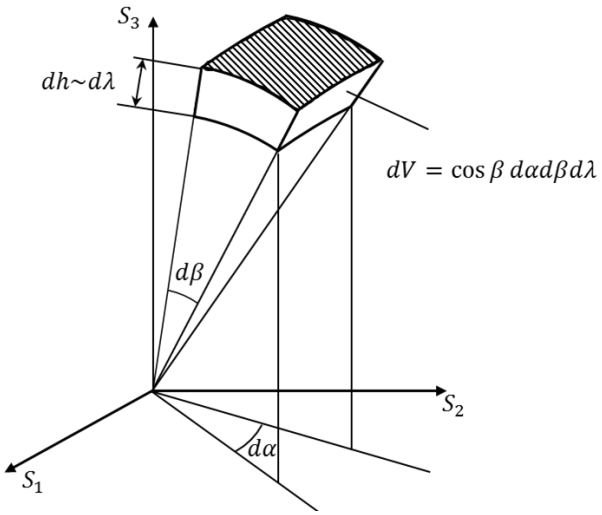

Fig. 3.6 Elementary volume of planes expressed via angles α, β, and λ.

Flow rule

To formulate the flow rule accepted in the framework of the Synthetic theory, the plastic strain intensity φ_N from Eq. (3.1.8) must be defined. For this purpose, the Synthetic theory proposes the following differential equation:

$$d\psi_N = r d\varphi_N - K\psi_N dt, \tag{3.1.13}$$

where ψ_N is defect intensity, t is time, r is the material constant, and K is a function of the homologous temperature and the effective stress (see below).

The defect intensity reflects an average scalar continuous measure of the number of dislocations, vacancies, interstitial defects, and other structural defects that form during inelastic straining in a slip system.

To relate the extent of material's strain hardening (H_N) to the development of crystalline grid defects ψ_N, the following relationship is proposed:

$$\psi_N = H_N^2 - I_N^2 - S_P^2 = \begin{cases} \left(\vec{\boldsymbol{S}} \cdot \vec{\boldsymbol{N}}\right)^2 - I_N^2 - S_P^2 & for\ planes\ reached\ by\ \vec{\boldsymbol{S}}\colon H_N = \vec{\boldsymbol{S}} \cdot \vec{\boldsymbol{N}} \\ 0 & for\ planes\ not\ reached\ by\ \vec{\boldsymbol{S}}\colon H_N > \vec{\boldsymbol{S}} \cdot \vec{\boldsymbol{N}} \end{cases}. \quad (3.1.14)$$

In the formula above, the term I_N is another element affecting the material's hardening, referred to as rate integral. I_N reflects the extent of the crystalline grid distortions induced by the development of crystal imperfections. It is defined as

$$I_N(t) = B \int_0^t \frac{d\vec{\boldsymbol{S}}}{ds} \cdot \vec{\boldsymbol{N}} \exp\left(-p(t-s)\right) ds, \quad (3.1.15)$$

where $0 < B < 1$ and p are model constants.

By integrating in (3.1.15) for the loading regime from Fig. 3.7 ($\dot{\vec{\boldsymbol{S}}} \geq 0$ for $t \in [0, t_M]$ and $\dot{\vec{\boldsymbol{S}}} = 0$ for $t > t_M$) we get the following formulae:

$$I_N = \frac{B}{p}\left(\dot{\vec{\boldsymbol{S}}} \cdot \vec{\boldsymbol{N}}\right)[1 - \exp(-pt)], \qquad t \in [0, t_M] \quad (3.1.16)$$

$$I_N = \frac{B}{p}\left(\dot{\vec{\boldsymbol{S}}} \cdot \vec{\boldsymbol{N}}\right)[\exp(pt_M) - 1]\exp(-pt), \quad t \geq t_M \quad (3.1.17)$$

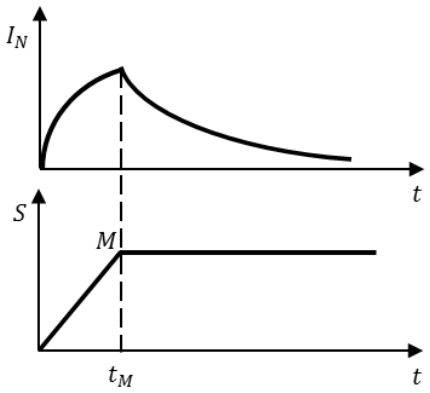

Fig. 3.7 $I_N \sim t$ plot (S is the length of the stress vector).

The formulae (3.1.16) and (3.1.17) mirror temporary deformation properties of materials as a function of the loading rate $\dot{\vec{\boldsymbol{S}}}$, namely:

1) During active loading ($\dot{\vec{S}} \geq 0$), when the number of tangled and locked dislocations increases monotonically, the rate integral grows, expressing the increase in the crystalline grid distortion. Therefore, Eq. (3.1.16) correctly reflects the well-known fact that the distortion's extent directly depends on the loading rate.

2) Under constant stress ($\dot{\vec{S}} = 0$), I_N decreases, reflecting the reduction of the crystalline grid distortion – favorable conditions arise to unlock the dislocations from their obstruction toward more favorable energetic positions, i.e., material relaxation/recovery takes place. The condition $I_N \to 0$ implies that $\psi_N(t) =$ const in Eqs. (3.1.14), indicating that recovery balances hardening. A condition like this is typical for steady-state creep; therefore, the transition between primary and secondary creep can be expressed as $I_N \to 0$.

Now, we can explain the term S_P from (3.1.14) and relate it to the yield strength S_S. S_P is the yield strength of a material as the loading rate tends to zero; its other name is creep limit. S_S. and S_P are related to each other as

$$S_S^2 = S_P^2 + I_N^2. \tag{3.1.18}$$

Table 3.1 shows the units of the terms included in the formulae (3.1.13) -(3.1.15)

Table 3.1 Units in terms of the synthetic theory

Quantity	Unit
H_N	MPa
ψ_N	MPa^2
φ_N	1
r	MPa^2
K	s^{-1}
p	s^{-1}
B	1

3.2 Partial cases

Let us examine the constitutive relationship of the synthetic theory (3.2.3) for different types of deformation

I. Steady-state creep

Since a balance between the work hardening and recovery processes is peculiar to the secondary creep,

the defect intensity is assumed to be constant, $\psi_N(t) = \text{const}$. As a result, $d\psi_N = 0$, and Eq. (3.1.13) leads to a constant value of the strain intensity rate:

$$r\dot{\varphi}_N = K\psi_N = \text{const}, \tag{3.2.1}$$

or

$$r\varphi_N = K\psi_N t. \tag{3.2.2}$$

This formula, together with (3.1.8), models a linear portion on the $\varepsilon{\sim}t$ creep diagram. The slope of the secondary creep diagram is regulated by the function K, which is defined as (Rusinko, A. and Rusinko, K., 2011)

$$\begin{gathered} K = K_1(T)K_2(\tau_0), \qquad K_1 = \exp\left(-\frac{Q}{RT}\right), \\ K_2 = \frac{9\sqrt{3}cr}{2\sqrt{2}\pi}\tau_0^{k-2}, \qquad c \text{ and } k = \text{const}, \end{gathered} \tag{3.2.3}$$

where Q is the creep activation energy, and τ_0 is effective stress.

II. Primary creep deformation

The integration in (3.1.13) gives

$$r\varphi_N = \psi_N + K\int_0^t \psi_N dt. \tag{3.2.4}$$

Since, as it was found out above, the term K governs the secondary creep rate (which, as well known, takes extremely small values), the second term on the right-hand side of Eq. (3.2.4) can be ignored as primary creep deformation is considered alone. If so, we obtain

$$r\varphi_N = \psi_N, \tag{3.2.5}$$

The temporary change in the strain rate φ_N is governed by the rate integral I_N included in ψ_N.

III. Plastic deformation

As the duration of plastic deformation is far less than that in creep condition ($t \to 0$), we can ignore the rate integral I_N in the formula for the defect intensity (3.1.14). In this case, we write down Eq. (3.2.5) as

$$r\varphi_N = \psi_N = (H_N^2 - S_S^2). \tag{3.2.6}$$

IV. Stress relaxation

After complete or partial unloading, when the increment in permanent deformation is terminated, $d\varphi_N = 0$, Eq. (3.1.13) becomes

$$d\psi_N = -K\psi_N dt. \tag{3.2.7}$$

This formula correctly mirrors the processes occurring in the work-hardened crystalline grid after removing the external load. Namely, the temporary relaxation processes occurring via the annihilation of opposite-sign dislocations, grain boundary collapse, lowering the effectiveness of barriers to hinder dislocation motion, etc.

In summary, as shown above, the synthetic theory, via the sole equation (3.1.13), covers a large circle of the material deformation states:

a) plastic straining (3.2.6),

b) primary (3.2.5) and secondary (3.2.1) creep,

c) defect relaxation (3.2.7).

The use of Eq. (3.2.4) can be found in Rusinko's paper (2015), where modeling the deformation of materials with low melting points, such as tin, at room temperature is considered.

Once again, it must be emphasized that in terms of the Synthetic theory, a single term is used – irrecoverable deformation –which manifests itself as an "instantaneous" or time-dependent deformation depending on the concrete loading/temperature regime.

3.3 The isotropy postulate and formulae for uniaxial stress states

According to Ilyushin (1963), the isotropy postulate reads that if the stress path is rotated in the stress deviator space, then the corresponding strain path is rotated by the same amount (this postulate is valid for only von Mises's medium).

Consider an arbitrary loading path as shown in Fig. 3.8. Let the corresponding strain vector be $\vec{\boldsymbol{e}}$, which makes angle η with the stress vector $\vec{\boldsymbol{S}}$. Now, we rotate the loading path by a certain angle, δ. To demonstrate the fulfillment of the isotropy postulate, we rotate the coordinate system by the same angle δ. Within the rotated coordinate system, we obtain an analog of the previous loading, and therefore, it is easy to conclude that the angle between vectors $\vec{\boldsymbol{S}}'$ and $\vec{\boldsymbol{e}}'$ must be the same as in the initial case. It is clear that the strain value strongly depends on the inner geometry of the loading path, but the rotation of the loading path as a rigid figure does not affect the relationship between vectors $\vec{\boldsymbol{S}}$ and $\vec{\boldsymbol{e}}$ and $\vec{\boldsymbol{S}}'$ and $\vec{\boldsymbol{e}}'$

at any point of loading trajectory.

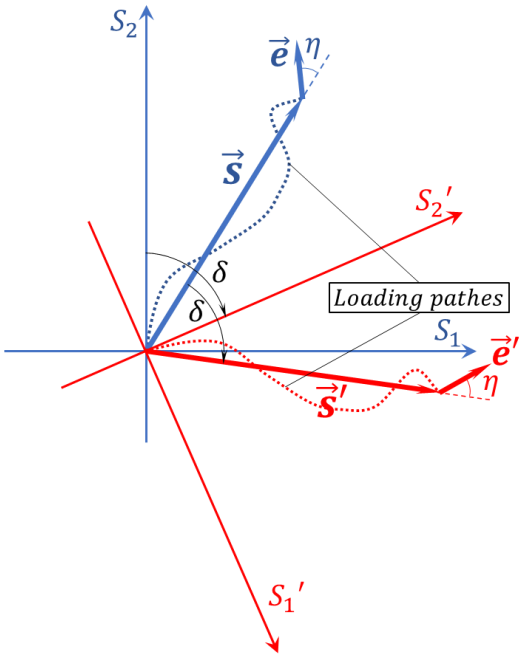

Fig. 3.8 On the postulate of isotropy

Consider two uniaxial stress states, torsion (pure shear) and tension. For the former, according to Eq. (3.1.1), the stress vector has coordinate $\vec{S}(0,0,\sqrt{2}\tau)$, i.e., is aligned along the S_3-axis. For the latter, the stress vector $\vec{S}\left(\sqrt{2/3}\,\sigma,0,0\right)$ elongates along the S_1-axis. The loading surfaces for the considered stress states, Fig. 3.9, show that the loading surface for tension can be obtained from that for pure shear by rotating the latter as a rigid object. Consequently, the postulate of isotropy can be utilized, and the formulae derived for the tension can be directly used for the uniaxial tension.

Pure shear is more convenient for the integration in (3.1.8) due to the formula for the plane distance (3.1.11), together with (3.1.10),

$$H_N = S_3 N_3 = \sqrt{2}\tau \sin\beta \cos\lambda, \tag{3.3.1}$$

does not contain angle α, and instead of triple integral, we have double integral over angles β and λ. In the case of plastic deformation, Eqs. (3.3.1), (3.2.6) and (3.1.8) give

$$e_3 = 2\pi \int_{\lambda}\int_{\beta} \varphi_N N_3 dV = \frac{4\pi}{r}\int_0^{\lambda_1}\int_{\beta_1}^{\pi/2} [(\tau \sin\beta\cos\lambda)^2 - \tau_S^2]\sin\beta\cos\lambda\cos\beta\, d\beta d\lambda, \tag{3.3.2}$$

where τ_S is the yield strength of material in pure shear.

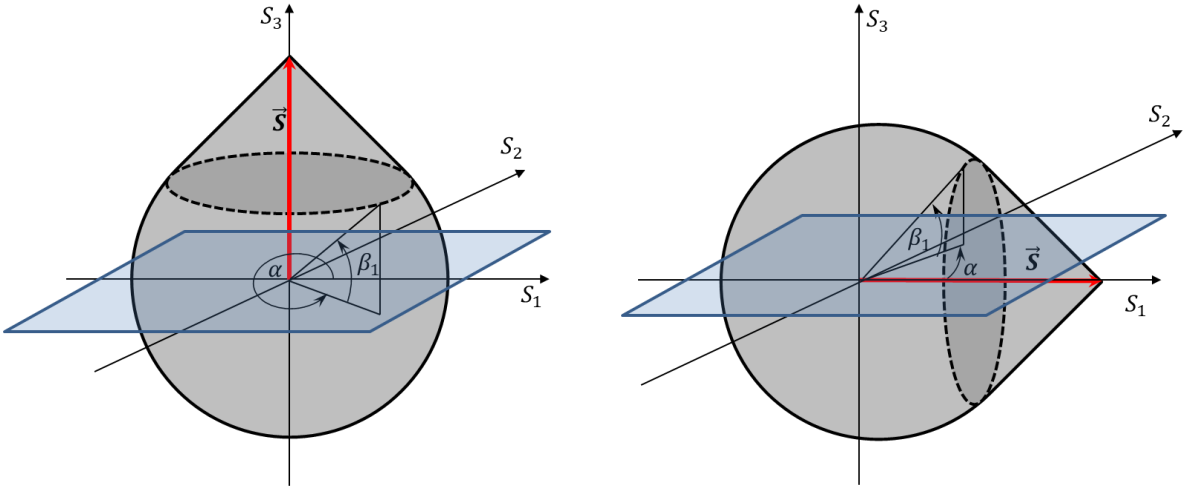

A B

Fig. 3.9 Loading surfaces for torsion (A) and tension (B)

According to the isotropy postulate, the formulae above hold if to replace the S_3 by S_1 and τ_S by $\sigma_S/\sqrt{3}$ (the von Mises medium):

$$r\varphi_N = \frac{2}{3}[(\sigma \sin\beta \cos\lambda)^2 - \sigma_S^2], \tag{3.3.3a}$$

$$e_1 = \frac{2\pi}{r}\int_{\beta_2}^{\pi/2}\int_{0}^{\lambda_2} \varphi_N \sin\beta \cos\lambda \cos\beta \, d\lambda d\beta =$$

$$= \frac{4\pi}{3r}\int_{0}^{\lambda_1}\int_{\beta_1}^{\pi/2} [(\sigma \sin\beta \cos\lambda)^2 - \sigma_S^2]\sin\beta \cos\lambda \cos\beta \, d\beta d\lambda \tag{3.3.3b}$$

$$= \frac{4\pi\sigma_S^2}{3r}\int_{0}^{\lambda_1}\int_{\beta_1}^{\pi/2} \left[\frac{\sin^2\beta\cos^2\lambda}{b^2} - 1\right] \sin\beta \cos\lambda \cos\beta \, d\beta d\lambda.$$

The boundary value λ_1 and β_1 are defined from the conditions $\psi_N = 0$ and $\lambda = 0$ (Rusinko, A. & Rusinko, K., 2009, 2011):

$$\sin\beta_1 = \frac{\sigma_S}{\sigma} \equiv b, \quad \cos\lambda_1 = \frac{\sigma_S}{\sigma \sin\beta}. \tag{3.3.4}$$

Integrating (3.3.3) for the boundary (3.3.4) yields

$$e_1 = a_0\Phi(b), \tag{3.3.5}$$

$$a_0 = \frac{\pi\sigma_S^2}{9r}, \tag{3.3.6}$$

$$\Phi(b) = \frac{1}{b^2}\left[2\sqrt{1-b^2} - 5b^2\sqrt{1-b^2} + 3b^4 \ln\frac{1+\sqrt{1-b^2}}{b}\right]. \quad (3.3.7)$$

Total elastoplastic deformation for the case of a uniaxial stress state is calculated as

$$e = a_0\Phi(b) + \frac{\sigma}{E} \quad (3.3.8)$$

Fig. 3.10 shows the plot of $\Phi(b)$, a monotone decreasing function of b. Therefore, the increase in σ implies the decrease in the b , which, in turn, means the growth of Φ and, consequently, deformation.

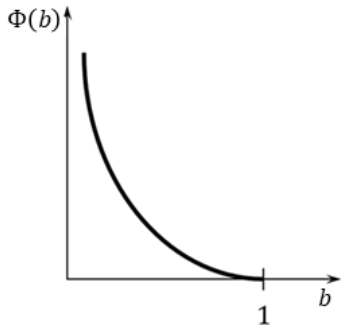

Fig. 3.10 $\Phi(b)$ plot

Creep deformation

Again, consider the case of uniaxial tension when the stress vector components (3.1.1) are $(S_1, 0,0)$, $S_1 = \sqrt{2/3}\,\sigma$. Eq (3.1.14), together with (3.1.15), takes the following form (Rusinko, A. & Rusinko, K., 2011):

$$\begin{aligned} r\varphi_N = \psi_N &= \frac{2}{3}[(\sigma \sin\beta\cos\lambda)^2 - (I\sin\beta\cos\lambda)^2 - \sigma_P^2] = (S_1^2 - I^2)\Omega^2 - S_P^2 \\ &= S_P^2\left(\frac{\Omega^2}{b^2} - 1\right), \end{aligned} \quad (3.3.9)$$

where $\Omega = \sin\beta\cos\lambda$, $I = B\int_0^t \dot{S}_1\, e^{-p(t-s)}ds$,

$$b = \frac{S_P}{\sqrt{S_1^2 - I^2}} = \frac{\sigma_P}{\sigma\sqrt{1 - B^2e^{-2pt}}}. \quad (3.3.10)$$

The incremental form of (3.1.13) is

$$\Delta\psi_N = 2(S_1\Delta S_1 - I\Delta I)\Omega^2. \quad (3.3.11)$$

Here we use the symbol Δ to distinguish the increments due to the acting stress and time from those over angles (d) in integral (3.1.8). Eqs. (3.3.9) and (3.1.13) give

$$r\Delta\varphi_N = 2(S_1\Delta S_1 - I\Delta I)\Omega^2 + KS_P^2\left(\frac{\Omega^2}{b^2} - 1\right)\Delta t. \tag{3.3.12}$$

Simple manipulations lead to

$$r\Delta\varphi_N = S_P^2\Delta\left(\frac{\Omega^2}{b^2} - 1\right) + KS_P^2\left(\frac{\Omega^2}{b^2} - 1\right)\Delta t. \tag{3.3.13}$$

Integration in (3.1.8) with (3.3.13) gives the deformation increment as

$$\Delta e = \frac{1}{r}\iiint\limits_{\alpha\beta\lambda}\left[S_P^2\Delta\left(\frac{\Omega^2}{b^2} - 1\right) + KS_P^2\left(\frac{\Omega^2}{b^2} - 1\right)\Delta t\right]\Omega\cos\beta\, d\alpha d\lambda d\beta = a_0(\Delta\Phi + K\Phi\Delta t), \tag{3.3.14}$$

where a_0 and Φ are expressed via (3.3.6) and (3.3.7) because the integrands in (3.3.14) are identical to that in (3.3.3b), with the only difference being that now $b(t)$ is defined via (3.3.10).

Finally, creep deformation in uniaxial tension, Eq. (3.2.4), takes the following form:

$$e = a_0\left[\Phi(b) + \int\limits_{t_S}^{t} K\Phi(b)dt\right], \tag{3.3.15}$$

where t_S is the instant of the start of plastic deformation.

To model the creep deformation alone, we subtract from the formula above the value of plastic deformation:

$$e_{Creep} = a_0\left[\Phi(b) - \Phi(b_M) + \int\limits_{t_M}^{t} K\Phi(b)dt\right], \tag{3.3.16}$$

where b_M is calculated by (3.3.10) at the end of active loading, $t = t_M$ (Fig. 3.7).

We can write the formula above as

$$e_{Creep} = a_0\left[\Phi(b) - \Phi(b_M) + K\int\limits_{t_M}^{t}\left(\Phi(b) - \Phi\left(\frac{S_P}{S_1}\right)\right)dt + K\Phi\left(\frac{S_P}{S_1}\right)(t - t_M)\right], \tag{3.3.17}$$

where fraction S_P/S_1 is obtained from b as $I \to 0$, i.e., it corresponds to the secondary creep.

So, we decompose the creep deformation into two portions, primary and secondary:

$$e_{Creep} = e_{CreepI} + e_{CreepII}$$
$$= a_0 \left[\Phi(b) - \Phi(b_M) + K \int_{t_M}^{\tilde{t}} \left(\Phi(b) - \Phi\left(\frac{S_P}{S_1}\right) \right) dt \right] + a_0 K \Phi\left(\frac{S_P}{S_1}\right)(t - t_M), \quad (3.3.18)$$

where $\tilde{t}$ is the moment of the transition to stationary creep.

Since the active loading and primary creep account for a small portion of the whole duration of creep experiments, we simplify the above equation as follows:

$$e_{Creep} = a_0 \left[\Phi(b) - \Phi(b_M) + K \Phi\left(\frac{S_P}{S_1}\right) t \right]. \quad (3.3.19)$$

Further througout, we use

$$e_{CreepI} = a_0 [\Phi(b) - \Phi(b_M)] \quad (3.3.20)$$

and

$$e_{CreepII} = a_0 K \Phi\left(\frac{S_P}{S_1}\right) t. \quad (3.3.21)$$

3.4 Mathematical Model of Deformation under Phase Transformations

As SMAs find ever-wider applications, the challenge of predicting their behavior when thermal and/or mechanical loadings are applied emerges. Numerous mathematical models have been developed to explain the deformation of SMAs (Liang et al., 1997, Muller ,1979,1980,1985, 1987, Achenbach et al., 1986). It is important to highlight the V.A. Lichachov and V.G. Malinin (1993) monographs since certain key ideas from them were used to create the model of PT-induced deformation using the synthetic theory presented in the following works: Goliboroda et al. (1999), Rusynko and Shandrivskyi (1996), Rusinko, A., and Rusinko, K. (2011). The following are the central tenets of this theory regarding phase transformations.

To apply Eq. (3.1.8) to the description of deformations induced by phase transformations, we relate the strain intensity rate to the rate of martensite fraction (Φ):

$$r\dot{\varphi}_N = \dot{\Phi}, \quad (3.4.1)$$

where r is the model constant. We define $\dot{\Phi}$ as

$$\dot{\Phi} = -\frac{\dot{T}_e}{M_s - M_f}, \tag{3.4.2}$$

where M_s and M_f are the martensite start and finish temperatures, respectively, and $\dot{T}_e$ is the rate of effective temperature, which will be defined below. Formula (3.4.2) holds for martensitic transformation at

$$\dot{T}_e < 0 \text{ and } M_f < T_e < M_s. \tag{3.4.3}$$

For austenitic transformation, we write

$$\dot{\Phi} = -\frac{\dot{T}_e}{A_f - A_s}, \qquad \dot{T}_e > 0 \text{ and } A_s < T_e < A_f, \tag{3.4.4}$$

where A_s and A_f are the austenite start and finish temperatures, respectively.

Formulae (3.4.2)-(3.4.4) give a linear relationship between the martensite fraction and effective temperature, which is widely accepted in the scientific community (Fig. 3.11).

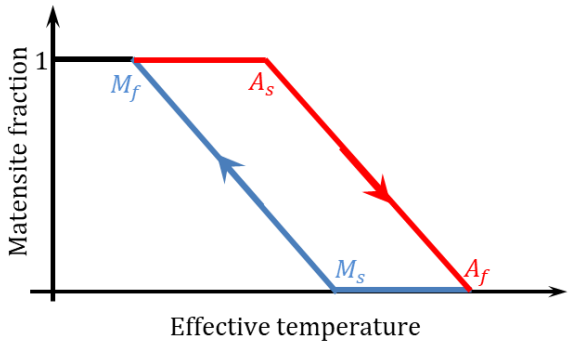

Fig. 3.11 $\Phi \sim T_e$ graph plotted via Eqs. (3.4.2)-(3.4.4)

In Eq. (3.4.4), T_e is effective temperature proposed in terms of the structural-analytic model by Likhachov, V.A. and Malinin, V. G. (1993), through the Clausius-Clapeyron equation, as

$$T_e = T\left(1 - D\vec{\boldsymbol{S}} \cdot \vec{\boldsymbol{N}}\right), \tag{3.4.5}$$

where D is the model constant. Eq. (3.4.5) enables one to account for the shift of the characteristic temperatures caused by loading. Summarising, formulae (3.4.2)-(3.4.5) define the amount of martensite as a single-valued function of temperature and acting load. The scalar product $\vec{\boldsymbol{S}} \cdot \vec{\boldsymbol{N}}$ gives the resolved shear stress acting in the element with $\vec{\boldsymbol{N}}$-orientation. This fact reflects the well-known fact that external load manifests differently depending on how preferable the element's/slip system's orientation is.

Austenite transformation

Differentiating in (3.4.5), formulae (3.4.1) and (3.4.4) give

$$r\dot{\varphi}_N = -\dot{T}_e = -\dot{T}\left(1 - D\vec{\boldsymbol{S}}\cdot\vec{\boldsymbol{N}}\right) + DT\dot{\vec{\boldsymbol{S}}}\cdot\vec{\boldsymbol{N}}. \tag{3.4.6}$$

In the formula above, the constant r includes $A_f - A_s$.

Consider austenitic transformation on heating when the material is under the action of constant stress, $\dot{\vec{\boldsymbol{S}}} = 0$.Eq. (3.4.6) gives

$$r\dot{\varphi}_N = -\dot{T}\left(1 - D\vec{\boldsymbol{S}}\cdot\vec{\boldsymbol{N}}\right) \tag{3.4.7}$$

Let us apply the above formula for the case of uniaxial tension (Fig. 3.12) when the stress vector, according to (3.1.1), has only one non-zero component, $S_1 = \sqrt{2/3}\,\sigma \equiv S = const$. We have

$$r\dot{\varphi}_N = -\dot{T}(1 - DS\sin\beta\cos\lambda). \tag{3.4.8}$$

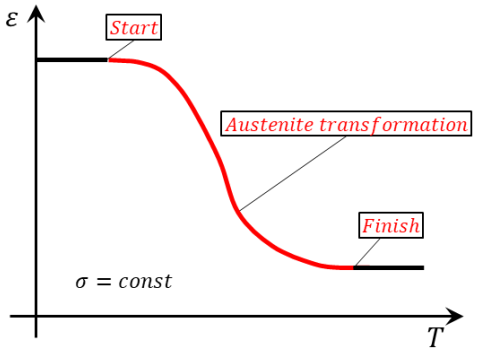

Fig. 3.12 Strain-temperature diagram in austenite transformation

The effective temperature from (3.4.5) for uniaxial tension is

$$T_e = T(1 - DS\sin\beta\cos\lambda). \tag{3.4.9}$$

Fig. 3.13 demonstrates the change in effective temperature from (3.4.9) for differently orientated elements (for simplicity, we set $\lambda = 0$). As one can see, the start and finish of the transformation strongly depend on the orientation of the element we consider.

On integrating in (3.4.8), we have

$$r\varphi_N = -T(1 - DS\sin\beta\cos\lambda) + C. \tag{3.4.10}$$

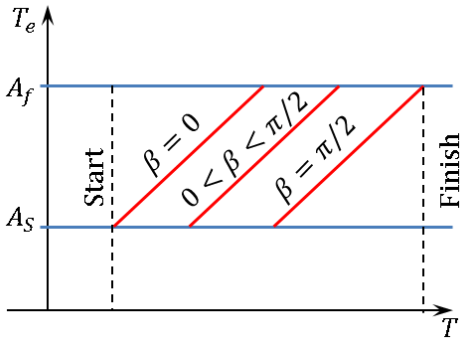

Fig. 3.13 Effective temperature for different directions ($\vec{S}$ = const).

The integration constant C is determined from the condition that the austenite reaction terminates ($\varphi_N = 0$) as the effective temperature reaches the austenite finish temperature, A_f. Since the transformation completion takes place at $\beta = \pi/2$ and $\lambda = 0$, we can calculate the austenitic transformation finish temperature, T_f. Equating T_e from (3.4.9) for the specified angle values to A_f, we obtain $T_f = A_f/(1 - DS)$. Now, Eq. (3.4.10) at $\varphi_N = 0$, $T = T_f$, $\beta = \pi/2$, and $\lambda = 0$ gives $C = A_f$. So

$$r\varphi_N = -(T - A_f) + TDS \sin\beta \cos\lambda. \tag{3.4.11}$$

Fig. 3.14 schematically shows the $\varphi_N \sim T$ graphs plotted with Eq. (3.4.11) for different values of β. Again, it is easy to see that different elements are involved in the transformation for different temperature ranges. Fig. 3.14 demonstrates the $\varphi_N \sim \beta$ graphs plotted with Eq. (3.4.11) for different effective temperatures. As one can see, at the start of the austenite transformation, φ_N takes non-zero values over the whole diapason of angle β (lines 1 and 2). As the temperature increases, the domain of angles β with positive strain intensities decreases and finally shrinks into the point $\beta = \pi/2$ where $\Phi = 0$). The boundary values of angles λ and β (points 1, 1′, 1″ for lines 3-5) are obtained from conditions $\varphi_N = 0$ and $\lambda = 0$:

$$\cos\lambda_1 = \frac{1}{DS\sin\beta}\left(1 - \frac{A_f}{T}\right), \qquad \sin\beta_1 = \frac{1}{DS}\left(1 - \frac{A_f}{T}\right). \tag{3.4.12}$$

Here we assume that $T > A_f$; for $T < A_f$ we let $\beta_1 = 0$ and $\lambda_1 = \pi/2$.

Therefore, the initial stage of the martensite-austenite transition is described by Eq. (3.1.8) with the integration diapason $0 \le \alpha \le 2\pi$, $0 \le \beta \le \pi/2$, and $0 \le \lambda \le \pi/2$ (lines 1 and 2 in Fig. 3.15), and in the course of temperature increase, when the domain of non-zero strain intensities shrinks (lines 3-5 in Fig. 3.15), the integral (3.1.8) becomes

$$e = \int_0^{2\pi} \int_0^{\lambda_1} \int_{\beta_1}^{\pi/2} \varphi_N \sin\beta \cos\lambda \cos\beta \, d\alpha d\beta d\lambda. \tag{3.4.13}$$

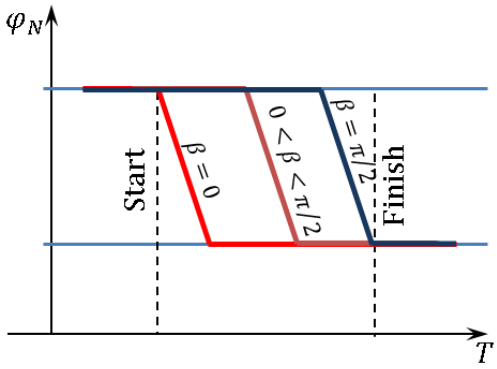

Fig. 3.14 $\varphi_N \sim T$ plots for different angles β ($\lambda = 0$, $\vec{S} = \text{const}$).

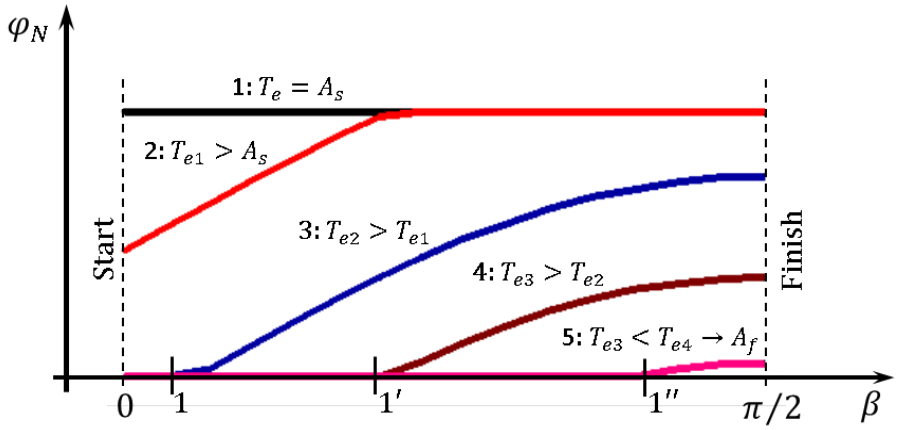

Fig. 3.15 $\varphi_N \sim \beta$ plots for different effective temperatures ($\lambda = 0$, $\vec{S} = \text{const}$).

Martensite transformation (pseudoelastic deformation)

Consider a material in a full austenite state at a constant temperature T_0. To induce martensite transformation, we apply load to the material, and the martensite fraction will increase according to Eq. (3.4.2) starting from the condition that the effective temperature achieves the martensite start temperature M_s. Eqs. (3.4.1), (3.4.2), and (3.4.5) in uniaxial tension give

$$T_e = T_0(1 - DS \sin\beta \cos\lambda), \tag{3.4.14}$$

$$r\varphi_N = M_s - T_e = M_s - T_0(1 - DS \sin\beta \cos\lambda). \tag{3.4.15}$$

In the formula (3.4.15), the constant r includes $M_s - M_f$.

First, derive a formula for the first value of tensile stress (S_Φ) inducing martensitic transformation in the material (Fig. 3.16). Equating the minimum value of T_e from (3.4.14) – $\beta = \pi/2$ and $\lambda = 0$ – to M_s, we obtain

$$S_\Phi = \frac{1}{D}\left(1 - \frac{M_s}{T_0}\right). \tag{3.4.16}$$

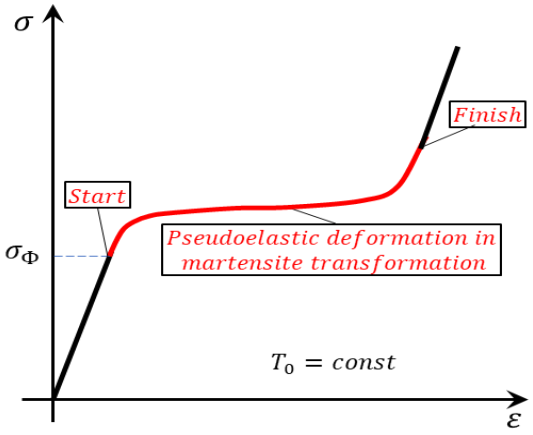

Fig. 3.16 Pseudoelastic stress-strain diagram

The range of the angles β and λ giving positive values for φ_N from (3.4.15) are

$$\beta_1 \le \beta \le \pi/2 \text{ and } 0 \le \lambda \le \lambda_1, \tag{3.4.17}$$

where λ_1 and β_1 are calculated from conditions $\varphi_N = 0$ and $\lambda = 0$, respectively:

$$\cos\lambda_1 = \frac{1}{DS\sin\beta}\left(1 - \frac{M_s}{T_0}\right), \qquad \sin\beta_1 = \frac{1}{DS}\left(1 - \frac{M_s}{T_0}\right). \tag{3.4.18}$$

Outside the range (3.4.17), we set $\varphi_N = 0$.

Substituting the strain intensity φ_N from formula (3.4.15) to Eq. (3.1.8), we get the pseudoelastic strain component in uniaxial tension ($e_1 \equiv e$) as

$$e = \frac{2\pi}{r}\int_0^{\pi/2}\int_0^{\pi/2} [M_s - T_0(1 - DS\sin\beta\cos\lambda)]\sin\beta\cos\lambda\cos\beta\, d\beta d\lambda \tag{3.4.19}$$

The factor 2π stands here because Equation (3.4.15) does not contain angle α.

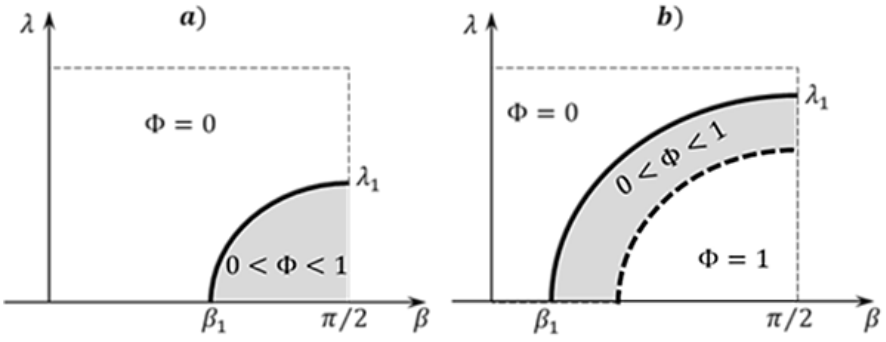

Fig. 3.17 Development of martensite transformation in the angle coordinates.

Fig. 3.17 explains what angles give positive values of the strain intensity during the integration by formula (3.4.19). In the initial stages of transformation (Fig. 3.17a), the integration is conducted on the angle range determined via Equations (3.4.17) and (3.4.18) as

$$e = \frac{2\pi}{r}\int_{0}^{\lambda_1}\int_{\beta_1}^{\pi/2} [M_s - T_0(1 - DS\sin\beta\cos\lambda)]\sin\beta\cos\lambda\cos\beta\, d\beta d\lambda \tag{3.4.20}$$

At the same time, as Φ becomes equal to 1 for given microvolumes, the further development of martensite trans-formation terminates, and there is no further increment in the deformation for these directions (Fig. 3.16b, domain $\Phi = 1$). When the condition $\Phi = 1$ extends to the whole range of angles – $0 \le \beta \le \pi/2$, and $0 \le \lambda \le \pi/2$ – we obtain a fully martensitic state of the material. The further increase in the loading will result in elastic deformation only. The first moment (stress S_f) when the condition $\Phi = 1$ fulfills is calculated from Equation (3.4.14) by letting $T_e = M_f$ at $\beta = \pi/2$ and $\lambda = 0$:

$$S_f = \frac{1}{D}\left(1 - \frac{M_f}{T_0}\right). \tag{3.4.21}$$

Summary

Beyond the problems considered above, Synthetic theory has proved itself a powerful tool for modeling a wide range of non-classical problems such as negative creep, the creep delay, the Feigin phenomena, the Haazen-Kelly effect, and the impact of direct current on inelastic deformation (Rusinko, A., 2012,2014 and 2016; Rusinko, A., Varga, P. 2018 and 2019; Varga, P., Rusinko, A., 2019).

My next chapter is devoted to extending Synthetic theory to the mathematical description of the inelastic deforming of metals in the ultrasonic field.

Chapter IV. Extension of the Synthetic theory to the ultrasound-assisted inelastic deformation

This chapter aims to model phenomena recorded in the experiments from Chapter II: ultrasound-assisted plastic and creep deformation and deformation during phase transformation. To accomplish this goal, a new term – common designation U – is entered into the equation that governs the development of the carriers of inelastic deformation, the defects of the crystalline grid. The logic for the presentation of U is dictated by the kinematics of the nucleation and multiplication of the crystal's imperfections in the ultrasound field. According to numerous experiments, see Figs. 2.4-2.7, ultrasonic defect intensity increases as a function of the ultrasonic energy intensity and time. A power function can model the impact of the former factor. The latter can be mathematically described through an exponential function, which mirrors that the ultrasonic defect intensity comes to saturation with sonication time. Therefore, the term U, responsible for the inelastic deformation superimposed by acoustic vibrations, is a product of ultrasound energy (power function) and sonication duration (exponential function).

4.1 Extension of the Synthetic theory to the case of plastic deformation with ultrasonic temporary and residual phenomena

In order to model the effects of ultrasound on the plastic straining of metals, we extend Eqs. (3.1.14) by two terms, U_t and U_r, as follows

$$\psi_{NU} = H_N^2 + U_t^2 + f(\gamma)U_r^2 - S_S^2, \tag{4.1.1}$$

where γ is stacking fault energy. Now Eq. (3.2.6) – flow rule within one slip system – gets

$$r\varphi_{NU} = H_N^2 + U_t^2 + f(\gamma)U_r^2 - S_S^2. \tag{4.1.2}$$

The term U_t reflects the temporary softening action of ultrasound because its presence in the formula above makes it possible to maintain a given value of strain intensity at less value of unidirectional stress $\vec{\boldsymbol{S}}$. We define U_t as

$$U_t = A_1 U^{A_2}(2 - e^{-pt})\left(\vec{\boldsymbol{u}} \cdot \vec{\boldsymbol{N}}\right), \quad t \in [0, \tau] \tag{4.1.3}$$

where U is ultrasonic energy density $\mathrm{J/m^3}$, $\vec{\boldsymbol{u}}$ is a unit vector indicating the vibration mode (longitudinal, torsional, etc.). For longitudinal sonication, the $\vec{\boldsymbol{u}}$ vector has $(1,0,0)$ coordinates in $\mathcal{S}^3$. The ultrasonic energy is readily expressed via vibration- or stress-amplitude (A and σ_m, respectively: $U = (1/2)\rho A^2 \omega^2$ and $\sigma_m = EA\omega/c$; Fitzpatrick (2018)). Further, τ is the sonication duration, and p and A_k $(k = 1,2)$ are model constants. If to denote through $\vec{\boldsymbol{U}}$ the vector $A_1 U^{A_2}(2 - e^{-pt})\vec{\boldsymbol{u}}$, Eq. (4.1.3) becomes $U_t = \vec{\boldsymbol{U}} \cdot \vec{\boldsymbol{N}}$, i.e., the action of ultrasound is presented by a vector whose component depends on acoustic energy/vibration amplitude and time.

Eq. (4.1.3) reflects numerous studies carried out on many metals (zinc, cadmium, aluminum, copper, and steel (Bagherzadeh et al. (2015), Geibler et al. (2009), Huang et al. (2009), Lum et al. (2009), Yao et al. (2012), Zhou et al. (2018)). They report that the magnitude of ultrasonic temporary softening depends on the vibration amplitude. According to this, we relate the temporary softening effect to the ultrasonic energy (stress amplitude) via power function, $2A_1 U^{A_2}$. Further, the product $A_1 U^{A_2} e^{-pt}$ corresponds to the temporary multiplication of ultrasound-induced defects (ψ_{NU}), which is proposed in Rusinko's early work (2011). The e^{-pt} function reflects the well-known fact that the number of ultrasound defects increases with time and then reaches a plateau (Tyapunina et al.,1982, Kulemin, 1978). Therefore, Eq. (4.1.3) is of dual nature. On the one hand, the ultrasound defects harden the material, but on the other hand, they become centers of softening processes. As evident from (4.1.3), since the term $(2 - e^{-pt})$ is always positive, the net effect is a prevalence of softening mechanisms during simultaneous action of unidirectional and oscillating load.

We define U_r as

$$U_r = h(\varepsilon - U) \times A_3 \int_0^{\tau} U^{A_4} dt, \tag{4.1.4}$$

where h is the Heaviside step function, ε is any positive infinitesimally small number so that ultrasound of any intensity results in a negative value of $\varepsilon - U$ difference. The presence of $h(\varepsilon - U)$ function means that the term U_r takes effect only after the ultrasound is off. Again, we propose a power function to express the dependence of ultrasonic residual hardening upon the ultrasound intensity with model constants A_3 and A_4. At the same time, the intensity of sonication is not the only parameter governing the magnitude of the hardening effect. Namely, the duration of sonication plays a vital role as well. In other words, the time-integral in (4.1.4) reflects the time-dependent magnitude of ultrasonic energy injected into the material. Summarizing, U_r reflects a post-sonicated defect pattern leading to the change in material characteristics/response after the acoustoplasticity.

Fig. 4.1 demonstrates the temporary behavior of functions U_t and U_r, which is based on Eqs. (4.1.3) and (4.1.4). For vibrating-assisted deformation, $t \in [0, \tau]$, U_t increases in the way prescribed by (4.1.3). At the same time, due to $h = 0$, $U_r = 0$ for $t \in [0, \tau]$. For the post-sonication period, we have an opposite situation. While, due to $U = 0$ for $t > \tau$, $U_t = 0$, the integral from (4.1.4) gives a nonzero value ($h(\varepsilon) = 1 \Rightarrow U_r > 0$).

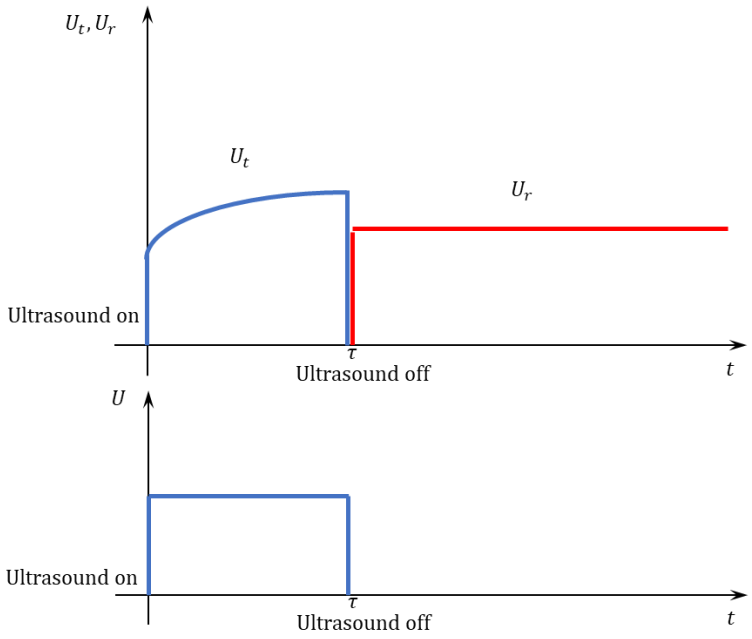

Fig.4.1 Temporary and residual terms in Eq. (4.1.2) as a function of ultrasonic action

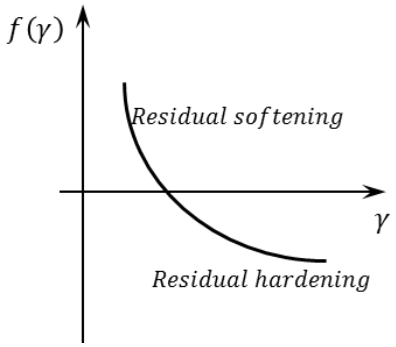

Fig.4.2 $f(\gamma)$ function

The effect from the product $f(\gamma)U_r^2$ in Eq. (4.1.2) depends on its sign. If to define $f(\gamma)$ as a decreasing function of γ, see its schematical plot in Fig. 4.2, it takes a negative value for high stacking fault energies. In this case, we obtain the case of residual ultrasonic hardening because the negative term $f(\gamma)U_r^2$ in Eq. (4.1.2) suppresses the development of plastic slips φ_{NU}. Or vice versa, for positive values of $f(\gamma)$, which is typical for materials with small γ, we arrive at the case of residual softening. Alas, so far, there is not enough experimental data on the effect of SFE upon the post-sonicated deformation for a wide

range of metals. If so, further we propose a linear relationship for $f(\gamma)$, when the comparison between the plastic deformation of titanium and aluminum will be studied.

Now, let ultrasound inspect how formula (4.1.2) works at points $A_1, A_2 \cdots$ in Fig. 2.14.

4.1.1 Acoustoplasticity

As vibration starts, formulae (4.1.2) and (4.1.3) at $t = 0$ give for uniaxial stress state (e.g., ultrasound-assisted compression or tension)

$$r\varphi_{NU} = H_N^2 + U_t^2 - S_S^2 =$$

$$= \left(\vec{\boldsymbol{S}} \cdot \vec{\boldsymbol{N}}\right)^2 + \left[A_1 U^{A_2}\left(\vec{\boldsymbol{u}} \cdot \vec{\boldsymbol{N}}\right)\right]^2 - S_S^2 = \tag{4.1.5}$$

$$= \frac{2}{3}\left[(\sigma_U \sin\beta \cos\lambda)^2 + \frac{3}{2}[A_1 U^{A_2} \sin\beta \cos\lambda]^2 - \sigma_S^2\right].$$

The boundary angles β and λ where $\varphi_{NU} = 0$ are

$$\sin\beta_{1U} = \frac{\sigma_S}{\sqrt{\sigma_U^2 + \frac{3}{2}(A_1 U^{A_2})^2}} \equiv b_U,$$

$$\cos\lambda_{1U} = \frac{\sigma_S}{\sqrt{\sigma_U^2 + \frac{3}{2}(A_1 U^{A_2})^2 \sin\beta}}. \tag{4.1.6}$$

To ensure the stress drop at the constant value of deformation, we demand that φ_{NU} equal φ_N from (3.2.6) at the same set of planes where the strain intensity is positive ($\beta_{1U} = \beta_1$, compare Figs. 4.3a and b). Equating b_U and b from (4.1.6) and (3.3.4) yields the value of stress (σ_U) which maintains the same deformation as before the ultrasound was On:

$$\sigma_U = \sqrt{\sigma^2 - \frac{3}{2}(A_1 U^{A_2})^2}. \tag{4.1.7}$$

The formula above enables ultrasound to calculate the ultrasound-induced stress drop.

As seen from Fig. 4.3b, the loading surface preserves its shape due to the compensation element $\vec{\boldsymbol{u}}$, i.e., less unidirectional stress is needed to keep the deformation at the instant as the ultrasonics vibration starts.

During simultaneous action of unidirectional loading and ultrasound, $t \in [0, \tau]$, Eq. (4.1.5) gets

$$r\varphi_{NU} = \frac{2}{3}\left[(\sigma_U \sin\beta \cos\lambda)^2 + \frac{3}{2}[A_1 U^{A_2}(2 - e^{-pt}) \sin\beta \cos\lambda]^2 - \sigma_S^2\right]. \qquad (4.1.8)$$

Plastic deformation in acoustoplasticity (e_U) is calculated by Eq. (3.3.3b), which is a partial case of Eq (3.1.8) for a uniaxial stress state, with the integrand from (4.1.8). As a result,

$$e_U = a_0 \Phi(b_U), \qquad b_U = \frac{\sigma_S}{\sqrt{\sigma_U^2 + \frac{3}{2}\left(A_1 U^{A_2}(2 - e^{-pt})\right)^2}}. \qquad (4.1.9)$$

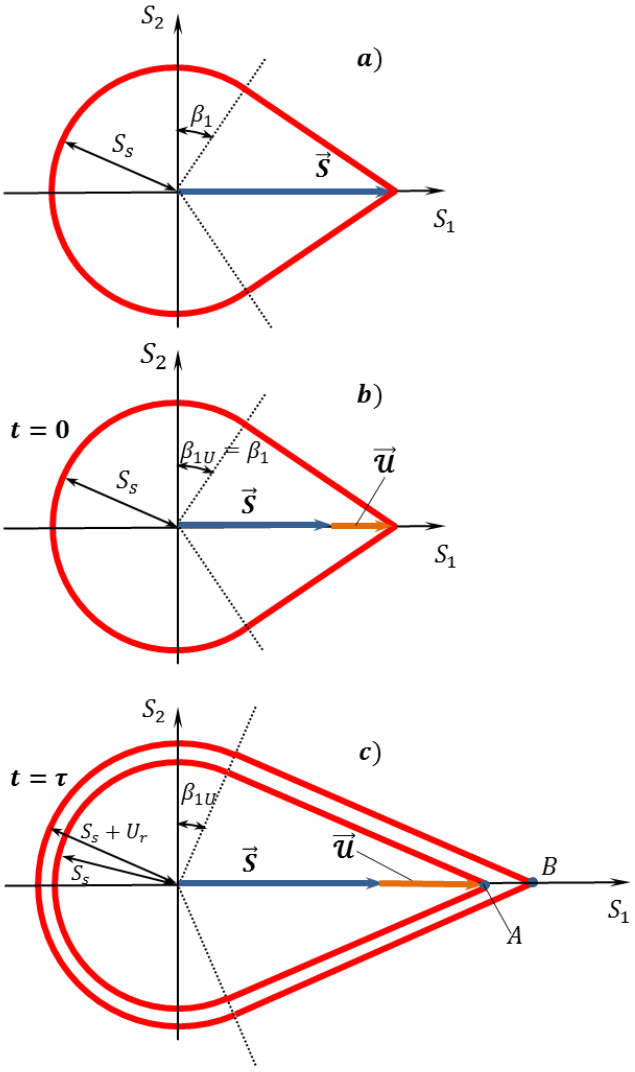

Fig.4.3 Evolution of loading surface during the sonication (tangent planes are not shown): **a**) ordinary plastic strain, **b**) ultrasound On, **c**) simultaneous action of static and vibrating load (A) and ultrasound Off (B).

Comparing Eq. (4.1.8) to (3.3.3a), we have that the presence of ultrasonic energy requires less stress to develop plastic deformation of a specimen (portion A_2-A_3 in Fig. 2.14). The inner surface in Fig. 4.3c, which corresponds to the end of sonication, clearly demonstrates that the loading point A is reached by the joint action of static ($\vec{S}$) and acoustic ($\vec{u}$) vector-portions.

It is the Eqs. (4.1.5)-(4.1.9) that describe the phenomenon of temporary ultrasonic softening analytically.

4.1.2 Residual hardening[1]

For simplicity, suppose that $f(\gamma) = -1$, i.e., consider the case of residual ultrasonic hardening alone when the term U_r enters Eq. (4.1.2) with a negative sign:

$$r\varphi_{NU} = H_N^2 + U_t^2 - U_r^2 - S_S^2. \tag{4.1.10}$$

After the ultrasound is Off ($t \geq \tau$), $U_t = 0$ and $U_r > 0$ (Fig. 4.1), the plastic strain intensity (4.1.10) loses the term U_t, which facilitated the strain intensity, but includes the negative U_r. As a result, the plastic strain intensity becomes of negative sign, i.e., the development of plastic deformation ceases. Eqs. (4.1.2) and (4.1.4) give that

$$H_N^2 = r\varphi_{NU} + \frac{3}{2}[A_3 U^{A_4}\tau]^2 + S_S^2, \tag{4.1.11}$$

where φ_{NU} is the plastic strain intensity cumulated during the acoustoplasticity. Eq. (4.1.11) says that, as the ultrasound is Off, the plane distances obtain jump-wise increments in all directions by the magnitude of U_r (Fig. 4.3c). Therefore, now, the endpoint of the stress vector is inside the loading surface, and plastic deformation will resume only when the stress vector reaches the first tangent plane, point B. In other words, till plastic strain intensity from (4.1.10),

$$r\varphi_{NU} = \frac{2}{3}\left[(\sigma \sin\beta \cos\lambda)^2 - \frac{3}{2}[A_3 U^{A_4}\tau]^2 - \sigma_S^2\right], \qquad (\sigma > \sigma_U) \tag{4.1.12}$$

remains negative, we have only an elastic deformation increment corresponding to the linear portions A_3-A_4 in Fig. 2.14. Comparing (4.1.12) to (3.3.3a), it is clear that the material has been harder after the sonication, i.e., greater stresses are needed to develop the same deformation as for the ordinary $\sigma{\sim}\varepsilon$ diagram. This fact reflects the phenomenon of ultrasonic residual hardening.

The increment in plastic strain intensity ($\Delta\varphi_{NU}$), after the elastic portion (beyond the point A_4 in Fig. 2.14), is calculated as the difference of strain intensities from Eqs. (4.1.12) and (4.1.8)

$$\Delta\varphi_{NU} = \frac{2}{3r}\left\{(\sigma \sin\beta \cos\lambda)^2 - \left[(\sigma_U \sin\beta \cos\lambda)^2 + \frac{3}{2}[A_1 U^{A_2}(2 - e^{-p\tau}) \sin\beta \cos\lambda]^2\right] - \frac{3}{2}(A_3 U^{A_4}\tau)^2\right\}. \tag{4.1.13}$$

[1] Relationships to calculate the plastic deformation under the simultaneous action of unidirectional and oscillating loading remains the same as in point 4.1.1.

where σ_U is the stress value at $t = \tau$.

Plastic strain increment (Δe) after the elastic portion is calculated by Eq. (3.3.3b) as

$$\Delta e = \frac{2\pi}{r} \int_{\beta_2}^{\pi/2} \int_{0}^{\lambda_2} \Delta\varphi_{NU} \sin\beta \cos\lambda \cos\beta \, d\lambda d\beta. \tag{4.1.14}$$

The integration boundaries in (4.1.14) are determined from Eq. (4.1.13) at $\Delta\varphi_N = 0$ and $\lambda = 0$.

The total deformation starting from the instant the ultrasound is Off takes the following form

$$e = e_U + \Delta e + \frac{\sigma}{E}, \tag{4.1.15}$$

where e_U is calculated via (4.1.9) at the end of sonication ($t = \tau$).

4.1.3 Model results: stress drop, acoustoplasticity, residual hardening. Material – Aluminum

This point aims (i) to construct model stress~strain curves in the compression tests for pure aluminum according to the sonication regimes shown in Fig. 2.14, (ii) to compare the analytic results with those obtained by Yao et al. (2012).

A) First, select the constant model r to fit the ordinary (base) $\sigma\sim\varepsilon$ diagram to the experimental one as best as possible. The analytic $\sigma\sim\varepsilon$ curve in Fig. 4.4, which is plotted via Eqs. (3.3.4)-(3.3.7) at $r = 1.3 \times 10^4$ MPa^2, $E = 6.8$ GPa, and $\sigma_S = 45$ MPa, shows good agreement with experimental data.

B) The next step is the instant when the ultrasound is On. I utilize Eq. (4.1.7) to calculate the ultrasound-induced stress drop for ultrasonic energy $U = 126.6\,\mathrm{J/m^3}$; the ultrasonic vibration starts at $\sigma_1 = 93.9$ MPa. Constants $A_1 = 18.5$ m^3/J and $A_2 = 0.25$ in Eq. (4.1.7) lead to the correct result (point 2 in Fig. 4.4). Further, Eq. (4.1.9) serves as an analytical tool to plot $\sigma\sim\varepsilon$ diagram under the action of ultrasound. Portion 2-3 in Fig. 4.4 is constructed at $p = 0.034$ s^{-1} for sonication time $\tau = 8$ s.

C) Finally, the deformation of post-sonicated material, portion 3-4 in Fig. 4.4, is plotted via Eqs. (4.1.13)-(4.1.15) at $A_3 = 3.5 \times 10^{-7}$ m^3/J and $A_4 = 4$. It can be clearly seen that the model result shows good agreement with experimental data.

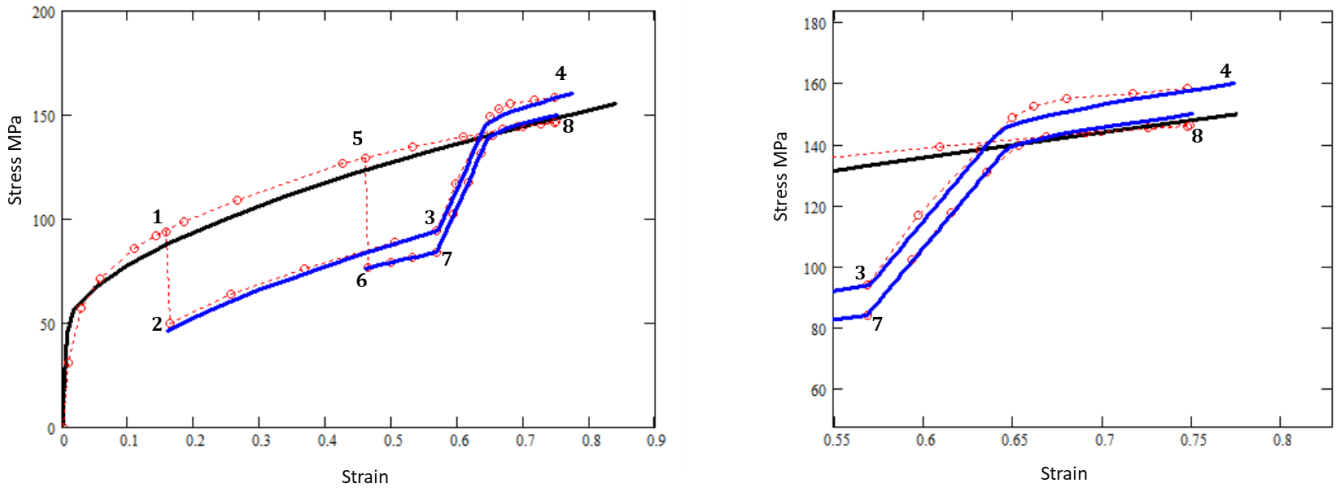

Fig.4.4 Vibration-assisted stress~strain diagrams for aluminum; lines – model, ○ – experiment (Yao et al., 2012).

D) To test the model constants selected above, first, we utilize Eq. (4.1.7) to calculate the ultrasound induced stress drop for different values of ultrasonic energy: $U_k = 5.89, 22.0, 60.33, 126.6\,\mathrm{J/m^3}$ (ultrasound is On at $\sigma_1 = 93.9$ MPa). Figure 4.5, plotted via Eq. (4.1.7) with the model constants selected above, demonstrates that the magnitudes of stress drops correlate well with the experiment.

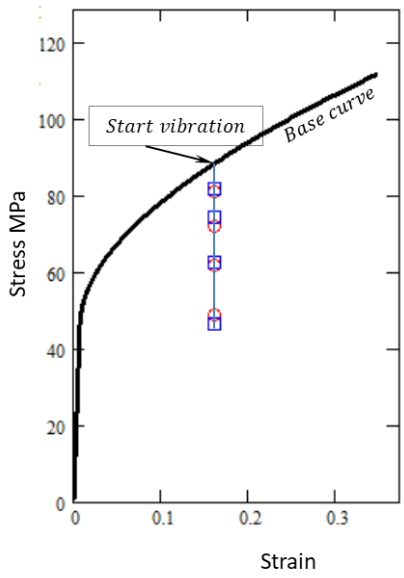

Fig. 4.5 Stress-drop due to different values of ultrasound energy; ☐ – model, ○ - experiment (Yao et al., 2012).

E) Inspect the deformation of aluminum for the case when the ultrasound with $U = 126.6\,\mathrm{J/m^3}$ starts at $\sigma_5 = 128.7$ MPa and acts only for 2 seconds ($\tau = 2$ s). As stated above, the deformation state of the material impacts the magnitude of the stress drop caused by ultrasonic energy. To take this into account, we enter constant A_1', which is related to A_1 as $A_1' = A_1\left(1 + a_1\frac{\sigma_5}{\sigma_1}\right)$. Now, Eq. (4.1.7) at $a_1 = 0.205$

gives a more significant stress drop (5-6) compared to that observed at σ_1. The further deformation portion (6-7-8) is plotted through the same formulae and constants as in points **A)-C)**. As evident from Fig. 4.4, the sonication of duration $\tau = 2$ s leads to a negligible deviation from the base $\sigma \sim \varepsilon$ diagram, i.e., the effect of residual hardening is not observed, which is in full conformity with the experimental record.

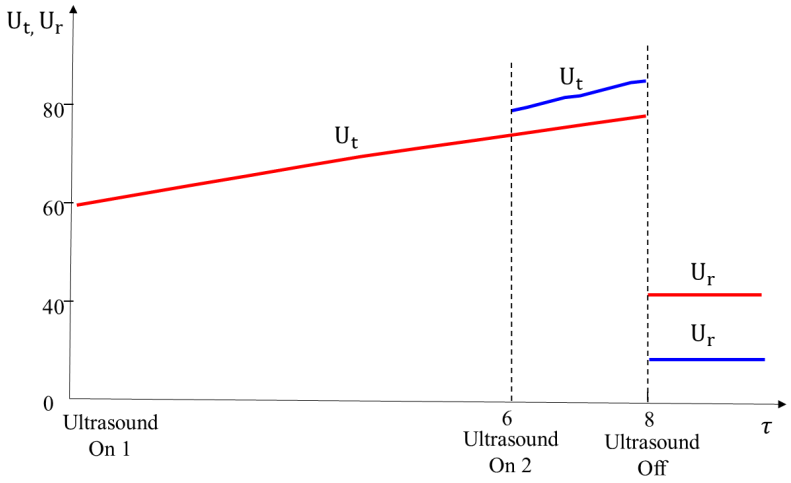

Fig.4.6 U_t and U_r plots for different sonication times

Fig. 4.6 gives relations between U_t and U_r, Eqs. (4.1.3) and (4.1.4), for the 8 and 2 seconds sonication time. As one can see, the value of U_t, when the ultrasound starts at the greater deformation (ultrasound On 2 – ultrasound Off), exceeds that for ultrasound On 1 – ultrasound Off. This fact correlates with experimental observations saying that the stress drop increases with the plastic deformation cumulated in the material. Another fact fitting the experiments is the value of U_r for 2-seconds-sonication is in order of magnitudes lower than that for 8 seconds. This means that the material structure transformations occurring during short sonication times do not affect the material deforming in the post-sonicated state.

4.1.4 Residual softening[2]

Now, suppose that $f(\gamma) = 1$, i.e., consider the case of residual ultrasonic softening alone when the term U_r enters Eq. (4.1.2) with a positive sign:

$$r\varphi_{NU} = H_N^2 + U_t^2 + U_r^2 - S_S^2. \tag{4.1.16}$$

[2] Relationships to calculate the plastic deformation under the simultaneous action of unidirectional and oscillating loading remains the same as in point 4.1.1.

As the ultrasound is Off, similar to the previous point, the plastic straining ceases because of the termination of ultrasonic energy inflow. At the same time, according to Eq. (4.1.16) at $U_t = 0$ and $U_r > 0$ and Eq. (4.1.4), the plane distances move in a jump-wise manner toward the origin of coordinates (Fig. 4.7d) by the magnitude of $\frac{3}{2}[A_3 U^{A_4}\tau]^2$:

$$H_N^2 = r\varphi_{NU} - \frac{3}{2}[A_3 U^{A_4}\tau]^2 + S_S^2. \tag{4.1.17}$$

This fact means that the stress vector reaches the loading surface in the post-sonicated state at less stress value. In other words, the plastic straining will be restored at the stress less than that without the residual softening effect: $\sigma_C < \sigma_A$ (Fig. 4.7d).

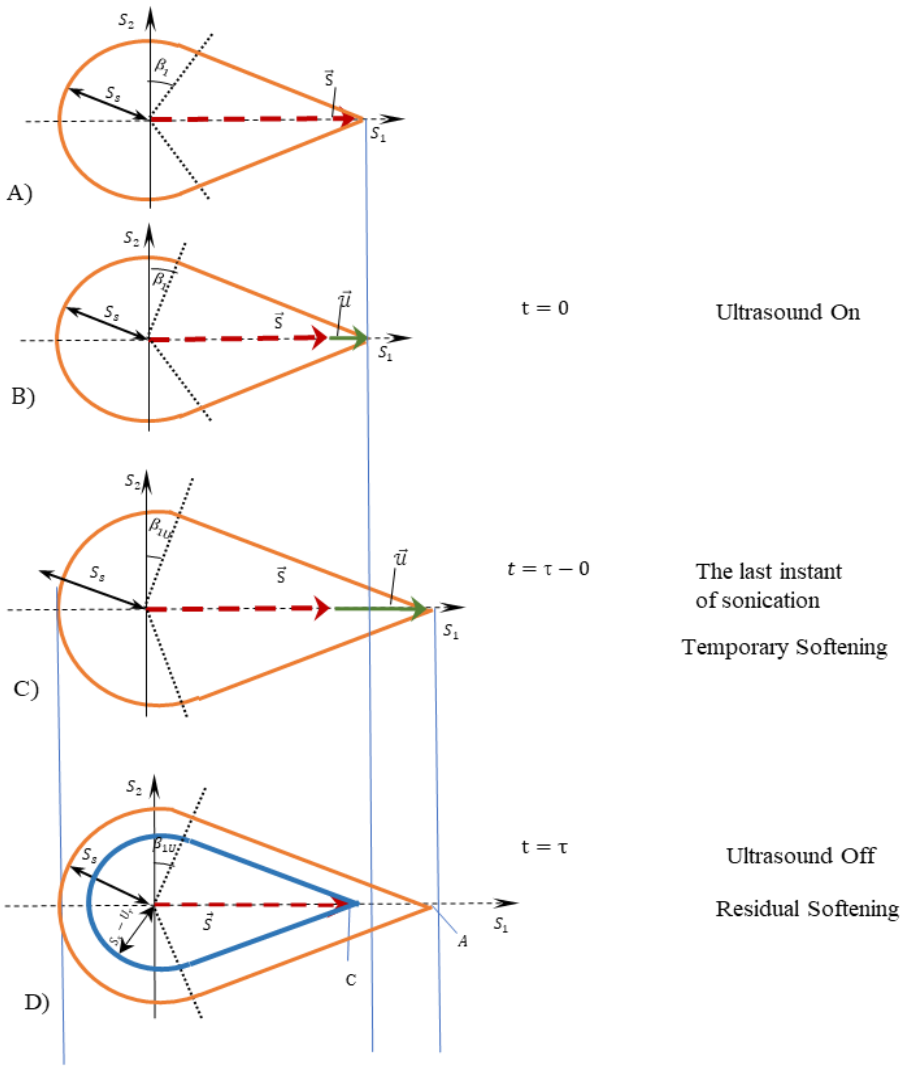

Fig.4.7 Evolution of loading surface during and after the sonication (tangent planes are not shown)

The strain intensity (4.1.16) in the uniaxial stress state for the post-sonicated period is

$$r\varphi_{NU} = \frac{2}{3}\left[(\sigma \sin\beta \cos\lambda)^2 + \frac{3}{2}[A_3 U^{A_4}\tau]^2 - \sigma_S^2\right] \tag{4.1.18}$$

Comparing formula (4.1.18) and (3.3.3a) it is clear that $\varphi_{NU} > \varphi_N$, meaning that plastic deformation occurs with less stress compared to the case of unidirectional load alone. Therefore Eqs. (4.1.17) and (4.1.18) model the effect of the ultrasonic residual softening when the $\sigma{\sim}\varepsilon$ curve locates beneath that, where unidirectional load acts alone.

The last step is to utilize Eqs. (4.1.14) and (4.1.15) where

$$\Delta\varphi_{NU} = \frac{2}{3r}\left\{(\sigma \sin\beta \cos\lambda)^2 - \left[(\sigma_U \sin\beta \cos\lambda)^2 + \frac{3}{2}[A_1 U^{A_2}(2 - e^{-p\tau}) \sin\beta \cos\lambda]^2\right] + \frac{3}{2}(A_3 U^{A_4}\tau)^2\right\}. \tag{4.1.19}$$

4.1.5 Model results: stress drop, acoustoplasticity, residual softening. Material – Copper

This point aims to inspect the relationships derived from the synthetic theory regarding their compatibility with experimental data obtained for the plastic deforming of copper in the ultrasonic field.

Consider Fig. 4.8 showing the compression test results recorded by Kang et al. (2020). Once the stress reaches 218 MPa, the ultrasound with oscillating amplitude and frequency $A = 1.3$ μm and $f = 20$ kHz, respectively, is On (point **1**). At point **2**, the ultrasound action terminates, and the plastic straining continues under static loading alone. It is easy to see that the phenomenon of ultrasound residual softening is observed.

Utilizing formulae from previous points, I start to construct the model curve.

A) Initially, the value of model constant r must be selected to achieve the best fit to the ordinary experimental $\sigma{\sim}\varepsilon$ curve (without ultrasound). The theoretical $\sigma{\sim}\varepsilon$ diagram in Fig. 4.8, which is plotted via Eqs. (3.3.4)-(3.3.8) at $r = 40000$ MPa^2 shows good agreement with experimental data (the Young modulus and yield strength are $E = 2.5$ GPa, and $\sigma_S = 160$ MPa, respectively).

B) To plot the acoustoplastic stress-strain diagram, we use formula (4.1.9), where the oscillating stress amplitude (σ_m) replaces the ultrasound energy intensity. These quantities are easily interchangeable due to the well-known relationships: $U = (1/2)\rho A^2\omega^2$ and $\sigma_m = EA\omega/c$ (Fitzpatrick, 2018). The oscillating stress amplitude is related to A through the following formula (Fitzpatrick, 2018):

$$\sigma_m = E\frac{2\pi f}{c}A, \tag{4.1.20}$$

where c is the speed of sound in copper $c = 4760$ m/s (Nevil et al., 1957). As a result, $\sigma_m = 4.39$ Mpa.

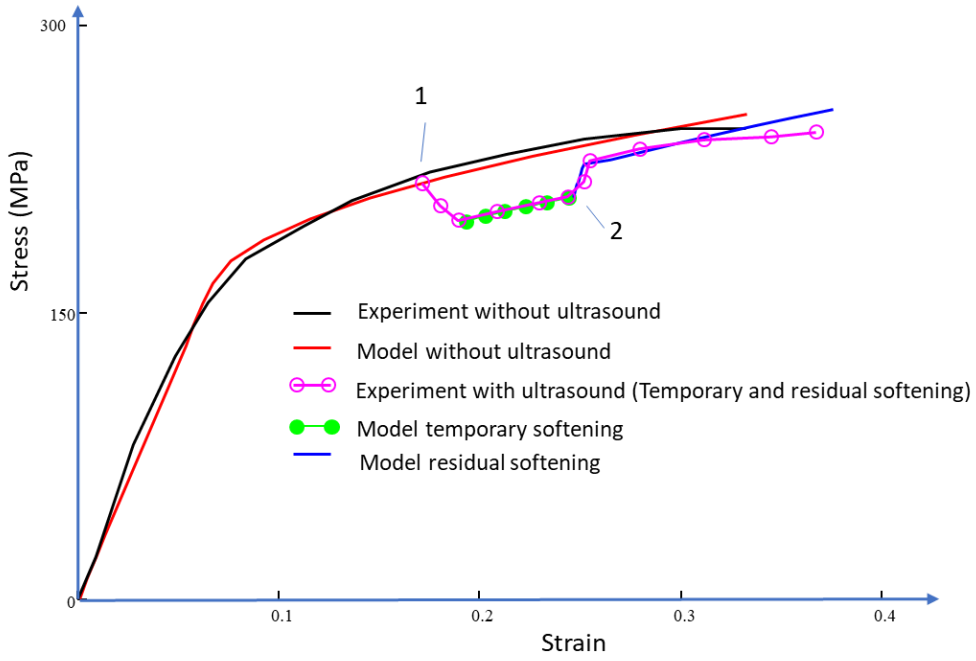

Fig. 4.8 Stress~strain compression diagrams for copper.

Formula (4.1.9) with the model constants

$A_1 = 43 \times 10^{-2}$ MPa$^{1-A_2}$, $A_2 = 0.5$, and $p = 1 \times 10^{-3}$ s^{-1}

leads to accurate results (see Fig. 4.8).

C) Finally, to model the deformation of post-sonicated material (residual softening) Eqs. (4.1.14), (4.1.15) and (4.1.19) to be used. To obtain the best fit with the test result, I selected the model constants $A_3 = 2.1 \times 10^{-7}$ MPa$^{1-A_4}$ and $A_4 = 1.1$.

Again, Fig. 4.8 indicate satisfactory agreement between the model results and experimental data.

4.1.6 General case

Let ultrasound utilize formula (4.1.2) in its general form, i.e., including $f(\gamma)$, for two materials – aluminum and titanium – that possess high and low stacking fault energy (SFE) values, respectively.

Since the term $f(\gamma)U_r^2$ enters into force only after the ultrasound is Off, this formula for the post-sonicated deformation ($U_t = 0$) gives

$$r\varphi_{NU} = H_N^2 + f(\gamma)U_r^2 - S_S^2. \tag{4.1.21}$$

Due to the absence of reliable information about the effect of SFE on what type of deformation reaction for different materials will be observed after the ultrasound is off, residual hardening or softening, we propose to define $f(\gamma)$ for two materials only. Relying on the experimental results conducted by Zhou et al. (2017), where aluminum demonstrates residual hardening and titanium residual softening, we define $f(\gamma)$ in a linear manner as

$$f(\gamma) = k(\gamma_{\mathrm{Al}} - \gamma) - 1, \tag{4.1.22}$$

where $k > 0$ is a model constant, i.e., we take γ_{Al} as a base value. It is easy to see that $f(\gamma_{\mathrm{Al}}) = -1$, and $f(\gamma_{\mathrm{Ti}})$ takes a positive value because $\gamma_{\mathrm{Al}} > \gamma_{\mathrm{Ti}}$.

Now, Eqs. (4.1.21) and (4.1.22) lead to the following strain intensities of aluminum and titanium in the post-sonication state when they are deformed under static load alone.

Aluminum:

$$r\varphi_{NU} = \frac{2}{3}\left[(\sigma \sin\beta \cos\lambda)^2 - \frac{3}{2}[A_3 U^{A_4}\tau]^2 - \sigma_S^2\right]. \tag{4.1.23}$$

Titanium:

$$r\varphi_{NU} = \frac{2}{3}\left[(\sigma \sin\beta \cos\lambda)^2 + \frac{3}{2}f(\gamma_{\mathrm{Ti}})[A_3 U^{A_4}\tau]^2 - \sigma_S^2\right]. \tag{4.1.24}$$

All that is left now is to compare Eqs. (4.1.23) and (4.1.24) to (3.3.3a).

Comparing formula (4.1.23) to (3.3.3a), it is evident that the strain intensity of aluminum after the sonication is less than that for ordinary loading. In other words, greater stress values are needed to maintain the plastic deforming, i.e., the stress~strain curve runs above that corresponding to ordinary loading. Therefore, formula (4.1.23) models the phenomenon of ultrasonic residual hardening, which is observed for aluminum.

With titanium, it is clear from (4.1.24) and (3.3.3a) that $\varphi_{NU} > \varphi_N$. Therefore, less stress plastically deforms the material in the post-sonicated state compared to ordinary loading, i.e., the stress~strain curve locates beneath that where unidirectional load acts alone. Here, we obtain the case of ultrasonic residual softening typical for aluminum.

Therefore, depending on SFE, function $f(\gamma)$ (4.1.22) correctly regulates, at least for two materials, their deformation behavior in the post-sonication state.

4.1.7 Model results: stress drop, acoustoplasticity, residual hardening and softening. Materials – Aluminum and Titanium

This section aims to plot ultrasound-assisted stress~strain curves for a pair of materials, aluminum and titanium, i.e., to inspect formulae (4.1.21) and (4.1.22) about their ability to catch the ultrasonic residual hardening and softening depending on the stacking fault energy value. The model results will be compared to those obtained in Zhou's experiments for ultrasound-assisted compression (Zhou et al., 2017). Since the relationships for the case of acoustoplasticity are the same as in the previous points, we only write down the formulae for the inelastic strain intensities in the post-sonicated period.

Aluminum:

$$\Delta\varphi_{NU} = \frac{2}{3r}\left\{(\sigma \sin\beta\cos\lambda)^2 - \left[(\sigma_U \sin\beta\cos\lambda)^2 + \frac{3}{2}[A_1{\sigma_m}^{A_2}(2-e^{-p\tau})\sin\beta\cos\lambda]^2\right] - \frac{3}{2}(A_3{\sigma_m}^{A_4}\tau)^2\right\}. \quad (4.1.25)$$

Titanium:

$$\Delta\varphi_{NU} = \frac{2}{3r}\left\{(\sigma \sin\beta\cos\lambda)^2 - \left[(\sigma_U \sin\beta\cos\lambda)^2 + \frac{3}{2}[A_1{\sigma_m}^{A_2}(2-e^{-p\tau})\sin\beta\cos\lambda]^2\right] + \frac{3}{2}f(\gamma_{\mathrm{Ti}})(A_3{\sigma_m}^{A_4}\tau)^2\right\}. \quad (4.1.26)$$

The difference between the above equations lies in the sign of the last term on their right-hand sides. While this term is of negative sign for aluminum, meaning the suppression of plastic straining (residual hardening), for titanium, the positive sign symbolizes that the plastic strain develops at less stress than in the ordinary case (residual softening).

Aluminum

A) The first step is to select the appropriate value of r to match the ordinary $\sigma\sim\varepsilon$ diagram (no vibration) to the experimental one. The theoretical $\sigma\sim\varepsilon$ curve in Fig. 4.9, which is plotted ultrasounding Eqs. (3.3.4)-(3.3.8) at $r = 6700$ MPa^2, $E = 70$ GPa, and $\sigma_S = 45$ MPa, exhibits good agreement with experimental data.

B) According to Zhou's records, the ultrasound starts when the unidirectional stress is about 79.2 MPa and acts for 24 seconds ($\tau = 24$ s). Four ultrasound amplitudes (A) with frequency $f = 30$ kHz were applied: $4.06, 4.36, 4.65, 4.97$ μm . Eq. (4.1.20) gives the following vibrating stress amplitudes corresponding to the values of A – $\sigma_{m1} = 8.3$ Mpa, $\sigma_{m2} = 8.9$ Mpa, $\sigma_{m3} = 9.6$ Mpa, $\sigma_{m4} = 10.2$ Mpa – which are obtained at the speed of sound for aluminum $c = 6420$ m/s.

Now, via formula (4.1.9) with the constants $A_1 = 1.9515 \times 10^{-2}$ MPa$^{1-A_2}$, $A_2 = 0.5$, and $p = 5.5 \times 10^{-3}$ s^{-1}, we plot $\sigma \sim \varepsilon$ diagrams for the plastic straining coupled with acoustic energy. As is seen from Fig. 4.9, the selected model constants lead to correct results for different values of ultrasound intensity (stress amplitude).

C) The final step is the deformation of post-sonicated material, which is calculated via Eqs. (4.1.14), (4.1.15), and (4.1.25). These relationships at $A_3 = 2.1 \times 10^{-7}$ MPa$^{1-A_4}$ and $A_4 = 4$ agree with experimental data (see Fig. 4.9), i.e., the model curves correctly model the phenomenon that the post-sonicated plastic straining requires great stress than in ordinary loading. In other words, after the sonication, the stress-strain curves locate above the ordinary $\sigma \sim \varepsilon$ plot, and this tendency increases with the amplitudes of the applied ultrasound.

Titanium

The titanium specimens were sonicated with the following amplitudes A: $5.63, 6.44, 8.49, 10.37$ μm. The frequency and duration of ultrasound were $f = 30$ kHz and $\tau = 24$ s, respectively. Eq. (4.1.20) at $c = 3300$ m/s gives the following values of stress amplitude: $\sigma_{m1} = 37.3$ Mpa, $\sigma_{m2} = 42.6$ Mpa, $\sigma_{m3} = 56.25$ Mpa, $\sigma_{m4} = 68.7$ Mpa.

A) Similarly to the previous case, first, we choose an appropriate value of r to match the model stress~strain diagram to the experimental one. Calculations in Eqs. (3.3.4)-(3.3.8) at $r = 4.6 \times 10^5$ MPa^2 , $E = 116$ GPa and $\sigma_S = 350$ MPa exhibit good agreement with the experimental data (Fig. 4.10, no vibration).

B) As ultrasound starts, which is about at $\sigma = 538$ MPa in Fig. 4.10, temporary ultrasonic softening occurs. Now, Eq. (4.1.9) comes into play, which, with constants $A_1 = 59$ MPa$^{1-A_2}$, $A_2 = 0.5$, and $p = 1.0 \times 10^{-3}$ s^{-1}, leads to correct results (see Fig. 4.10).

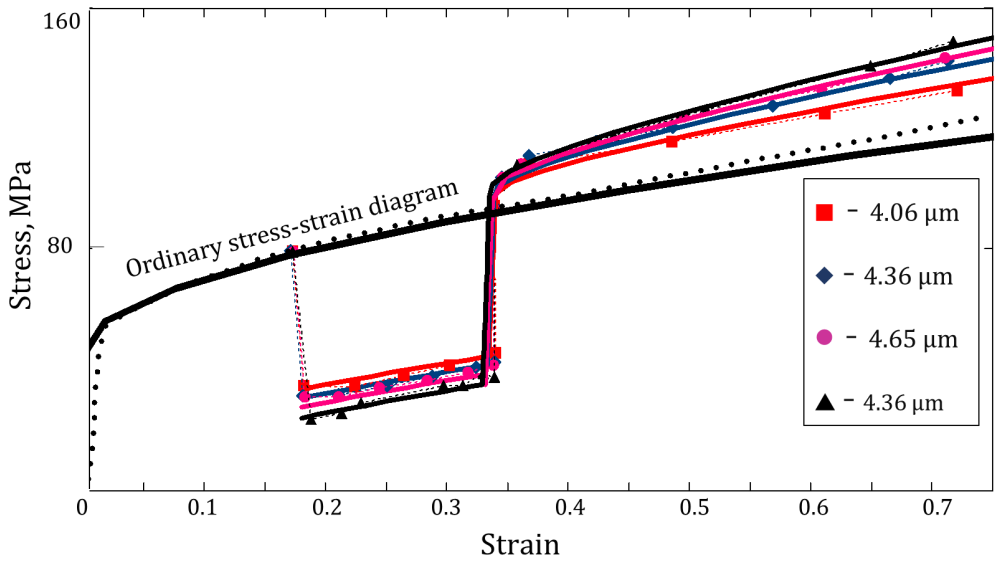

Fig. 4.9. Stress~strain compression diagrams of aluminum in the ultrasonic field (points – experimental data , Zhou et al. (2017); lines – model curves).

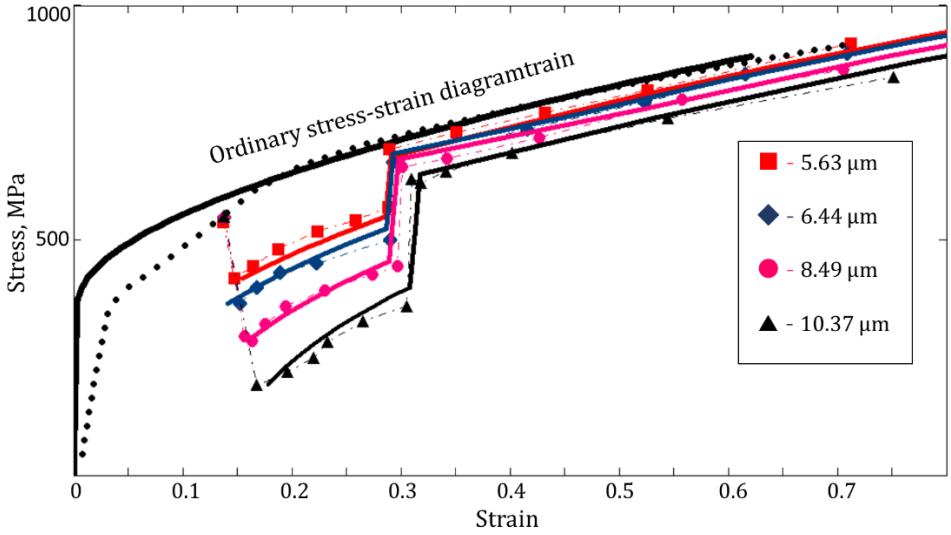

Fig. 4.10 Stress~strain compression diagrams for titanium in the ultrasonic field (points – experimental data, Zhou et al. (2017); lines – model curves).

C) Finally, we plot $\sigma\sim\varepsilon$ diagrams for the post-sonicated period. If to utilize Eqs. (4.1.14), (4.1.15), and (4..1.26) at $\gamma_{\mathrm{Al}} = 166\ \mathrm{mJ/m^2}$, $\gamma_{\mathrm{Ti}} = 15\ \mathrm{mJ/m^2}$, $A_3 = 2.5\times10^{-5}\ \mathrm{MPa}^{1-A_4}$, $A_4 = 2$, and $k = 1.0\ \mathrm{m^2/mJ}$, we achieve the conformity of the analytical results to experimental ones (see Fig. 4.10).

The results regarding section 4.1 are published in

Rusinko, A. & Alhilfi, A. (2020)

Alhilfi, A. & Rusinko, A. (2021)

Alhilfi, A. & Rusinko, A., (2022) a,b

Thesis I

In terms of the Synthetic theory, a model for the analytical description of the plastic flow of metals in the ultrasound field has been developed. The proposed extension of the Synthetic theory leads to correct results when considering the following phenomena:

(i) Stress drop on the stress~strain diagram as the ultrasound is On

(ii) Acoustoplasticity – stress~strain diagrams under the simultaneous action of unidirectional and vibrating load

(iii) Ultrasound residual hardening/softening – stress~strain diagram for the post-sonicated state of the metals.

4.2 Extension of the synthetic theory to the case of ultrasound-assisted time-dependent processes

Here, the modeling of time-dependent processes in an acoustic field is presented. Two cases are considered:

(i) creep deformation coupled with ultrasound.
(ii) relaxation processes of the work-hardened material under the action of ultrasound.

4.2.1 Ultrasound-assisted primary creep

Adhering to the overall concept of modeling ultrasound's effect on irrecoverable deformation, the basic relationship of the synthetic theory, Eq. (3.1.14), is to be extended by the term responsible for acoustic energy:

$$\psi_N = H_N^2 - I_N^2 - S_P^2 + U_C^2. \tag{4.2.1}$$

We define U_C (index C stands for *Creep*) as

$$U_C = \vec{\boldsymbol{u}} \cdot \vec{\boldsymbol{N}}, \tag{4.2.2}$$

where is defined via ultrasound-induced defects intensity proposed by Rusinko in its early work (2011) as

$$\vec{\boldsymbol{u}} = A_1 {S_m}^{A_2} (1 - e^{-wt}) \vec{\boldsymbol{u}}. \tag{4.2.3}$$

In the formula above, S_m is the oscillating stress vector amplitude, and $\vec{\boldsymbol{u}}$ is a unit vector indicating the vibration mode (longitudinal, torsional, etc.). For longitudinal sonication, the $\vec{\boldsymbol{u}}$ vector has $(1,0,0)$ coordinates in $\mathcal{S}^3$, and $S_m = \sqrt{2/3}\,\sigma_m$. A_1, A_2, and w are model constants to be chosen to fit the theoretical results to experimental ones. The scalar product in (4.2.2) means that the ultrasound effect strongly depends on the slip system orientation.

U_C from (4.2.1) symbolizes the increase of plastic slip within one slip system (ultrasonic softening) caused by the nucleation and development of ultrasound-induced defects. To avoid misunderstanding

that the increasing number of defects would harden the material, we address Kulemin's (1978) explanation: "When external loading couples with ultrasonic irradiation, both hardening and softening occur. The softening, however, is more intensive, and we observe the phenomenon of temporary softening". Therefore, Eq. (4.2.1) is dual; on the one hand, the ultrasound defects harden the material, but on the other hand, they become centers of softening processes.

To reflect the fact that the effect of sonication depends on the material's deformation state, we propose to write down A_1 from (4.2.3) as a linear function of deformation

$$A_1 = A_1'|\vec{\boldsymbol{e}}| + A_1'', \quad A_1', A_1'' = \text{const.} \tag{4.2.4}$$

Remark. The proposition to modify/extend the rate integral in (4.2.1) by "ultrasound parameters" is not promising because, according to the experiment in Fig. 2.22, the periodic sonication starts at the end of the primary creep portion, $I_N \to 0$, and there is no effect from the rate-integral. Besides, when the ultrasound is off, the creep develops with the same velocity as during ordinary loading.

4.2.2 Primary creep coupled with ultrasound

A) Simultaneous action of unidirectional loading and ultrasound

According to (4.2.1)-(4.2.3) and (3.2.5), the strain intensity in the acoustic field (φ_{NU}) for the case of uniaxial tension and longitudinal sonication is

$$\varphi_{NU} = \frac{2}{3r}[(\sigma \sin\beta \cos\lambda)^2(1 - B^2e^{-2pt}) + (A_1{\sigma_m}^{A_2}(1 - e^{-wt})\sin\beta\cos\lambda)^2 - \sigma_P^2] \tag{4.2.5}$$

The range of non-zero values of φ_{NU} is

$$0 \le \lambda \le \lambda_{1U}, \qquad \beta_{1U} \le \beta \le \frac{\pi}{2}, \tag{4.2.6}$$

where

$$\cos\lambda_{1U} = \frac{\sigma_p}{\sin\beta\sqrt{\sigma^2(1 - B^2e^{-2pt}) + \left(A_1{\sigma_m}^{A_2}(1 - e^{-wt})\right)^2}},$$
$$\sin\beta_{1U} = \frac{\sigma_p}{\sqrt{\sigma^2(1 - B^2e^{-2pt}) + \left(A_1{\sigma_m}^{A_2}(1 - e^{-wt})\right)^2}} \equiv b_U. \tag{4.2.7}$$

Formulae (3.1.8) and (4.2.5)-(4.2.7) give the ultrasound-assisted inelastic deformation as

$$\mathcal{E}_U = a_0\Phi(b_U). \tag{4.2.8}$$

Comparing the creep deformation from the formula above to that obtained for ordinary creep – $a_0\Phi(b)$ from (3.3.19) – it is easy to conclude that the appearance of U_C in (4.2.5) lead to greater creep deformation values because of

(i) $\varphi_{NU} > \varphi_N$ (3.3.9), acoustic intensity increases deformation within active slip systems

(ii) $b_U < b$ (3.3.10), ultrasound increases the number of active slip systems where irrecoverable deformation occurs.

To obtain graphs as in Fig. 2.22, we use the following formula:

$$e_U = a_0[\Phi(b_U) - \Phi(b_{U0})], \tag{4.2.9}$$

where $b_{U0} = b_U(t = 0)$.

Formally, the fact that both $\Phi(b_U)$ and $\Phi(b_{U0})$ are greater than $\Phi(b)$ and $\Phi(b_0)$, respectively, does not necessarily mean the same for their differences. To simplify derivations, let us apply the approximated relationship for function Φ (Rusinko, A, and Rusinko, K., 2011):

$$\Phi \approx \left(\frac{1}{x} - 1\right)^2. \tag{4.2.10}$$

Using formulae (4.2.9), (3.3.20), and (4.2.10), inspect the sign of

$$\Delta = e_U - e, \tag{4.2.11}$$

where index "*M*" in (3.3.20) corresponds here to "0".

The result is

$$\Delta = a_0\frac{2\sigma}{\sigma_P}\left\{\sqrt{(1-B^2)}\left(\sqrt{1+\frac{U^2}{\sigma^2(1-B^2)}}-1\right) - \sqrt{(1-B^2e^{-2pt})}\left(\sqrt{1+\frac{U^2}{\sigma^2(1-B^2e^{-2pt})}}-1\right)\right\}. \tag{4.2.12}$$

Since $e^{-2pt} < 1$ as $t > 0$, one can conclude from the formula above that $\Delta > 0$.

B) Periodic switch of ultrasound during creep deformation

Consider the following regime of sonication

$$U_C = \begin{cases} U_{Ci} & \text{for } \ t \in [t_i, t_i + \tau] \\ 0 & \text{for } \ t \in [t_i + \tau, t_i + \tau + T] \end{cases} \tag{4.2.13}$$

where τ is the sonication duration, and T is the ultrasound-free period.

Now, formula (4.2.9) takes the form as follows:

$$e_{Ui} = a_0\left[\Phi(b_{Ui}) - \Phi\left(b_{U(i-1)}\right)\right], \ \ i = 1,2,3 \tag{4.2.14}$$

where b_{Ui} is calculated via (4.2.7) at $t = t_i + \tau$, and b_{U0} corresponds to the beginning of sonication, i.e., is taken from (3.3.10).

Now, inspect the formula above for conformity with experimental data. As it follows from (4.2.2) and (4.2.3), the increment in creep deformation decreases with each subsequent sonication, since $(1 - e^{-wt})$ tends to 1 with time. Further, after the ultrasound is off, the creep deformation ceases to increase, preserving its value obtained at the end of the previous sonication. Finally, formula (4.2.4), where the ultrasound effect is related to the material's deformation state, ensures that the creep deformation gains a greater increment at the periodic sonication than during the continuous action of ultrasound. If we ignored Eq. (4.2.4), both creep diagrams would tend to a common value, which contradicts the experiment results.

4.2.3 Results. Discussion

This point deals with plotting creep diagrams for copper and aluminum in the ultrasonic field obtained in the framework of the synthetic theory.

Copper

First, consider the following cases of copper creep coupled with ultrasound:

(i) ordinary creep at stress $\sigma = 30$ MPa,

(ii) ultrasound-assisted creep: the ultrasound of oscillating stress amplitude $\sigma_m = 2.6$ MPa acts continuously from the very beginning of the creep,

(iii) ultrasound-assisted creep: the ultrasound of oscillating stress amplitude $\sigma_m = 2.6$ MPa acts periodically – $t_1 = 20$ min, $t_2 = 60$ min, $t_3 = 100$ min, $\tau = T = 20$ min (see Eq. (4.2.20)).

A) To plot the ordinary creep diagram, we use formulae (3.3.20) and (3.3.10). As a result, Curve 1 in Fig. 4.11 constructed with $\sigma_P = 5$ MPa , $B = 1.9 \times 10^{-1}$, $p = 2.1 \times 10^{-3}\ \mathrm{s}^{-1}$, and $r = 1.45 \times 10^5$ MPa^2 shows good agreement with the experimental one.

B) The next step is the creep diagram with the simultaneous action of unidirectional and oscillating stresses. It must be stressed that the model constants used above also remain unchangeable here. Formulae (4.2.9), (4.2.7), and (4.2.4) with model constants $A_1'' = 5.375$ MPa$^{1-A_2}$,[3] $A_2 = 1.0$, and $w = 9.5 \times 10^{-4}\ \mathrm{s}^{-1}$ lead to a good fit between the theoretical and experimental results (Curve 2 in Fig. 4.11).

C) In the last case, periodic sonication, the first portion of the sonication starts in the 20th minute of creep when deformation is $\varepsilon = 1.24 \times 10^{-4}$. Curve 3 from Fig. 4.11 demonstrate the results obtained via Eqs. (4.2.14), (4.2.7), and (4.2.4) at $A_1' = 2.75 \times 10^3$ MPa$^{1-A_2}$.

The analysis of Fig. 4.11 shows that the creep deformation at the beginning of sonication (shadowed areas) increases more intensively than that obtained analytically. At the same time, with the further increase in t, the model results show outstanding accordance with the experimental data for continuous and periodic sonication. Thus, for the periodic action of ultrasound, the maximum height of error bars in Fig. 4.11 is only -15.85% for $t \geq 40$ min.

Aluminum

Another case to be tested is the ultrasound-assisted creep of aluminum (continuous longitudinal sonication is considered). Together with an ordinary creep in uniaxial tension at $\sigma = 10$ MPa, the creep deformation in the acoustic field was modeled at the following values of vibrating stress amplitudes: $\sigma_{m1} = 1.3$ MPa and $\sigma_{m2} = 2.0$ MPa (Fig. 4.12; Kulemin,1978).

[3] Since the ultrasound acts from the very vegining of the experiment ($e = 0$), the model constant A'_1 is not needed.

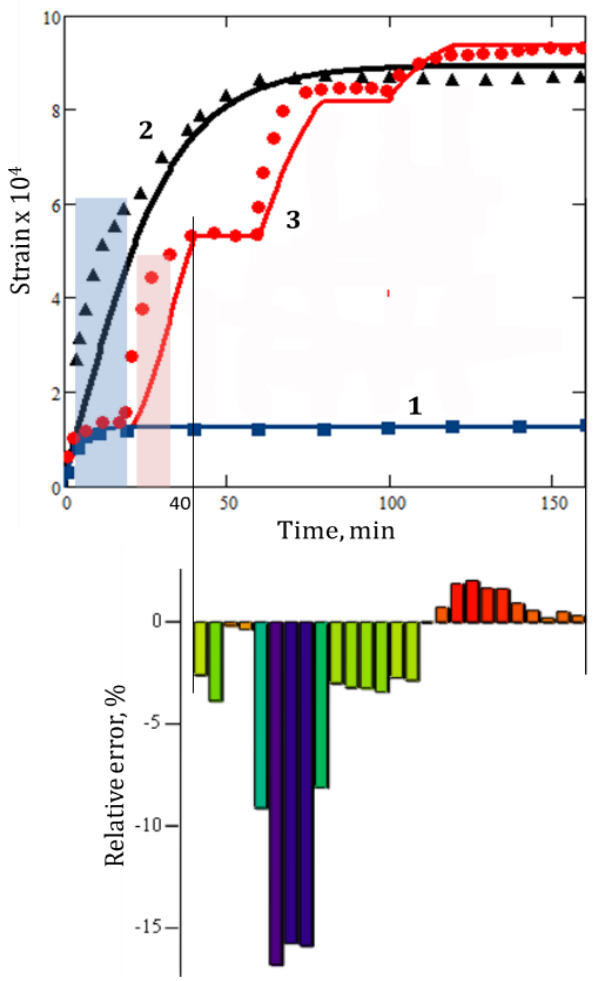

Fig. 4.11 Strain vs. Time diagrams of copper: **1** – ordinary creep, **2** – ultrasound-assisted creep with continuous sonication, **3** – ultrasound-assisted creep with periodic sonication; symbols – experiment (Kulemin, 1978), lines – model. Error bars are constructed for the case of periodic sonication ($t \geq 40$ min).

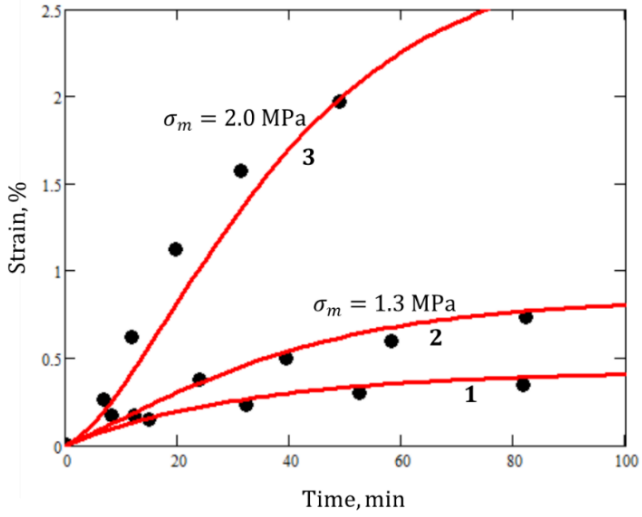

Fig. 4.12 Strain vs. Time diagrams of aluminum in uniaxial tension ($\sigma = 10$ MPa, $t = 40$°C): 1 – ordinary creep, 2 and 3 – ultrasound-assisted creep with continuous sonication, ● – experiment (Kulemin, 1978), lines – model.

The technique of constructing strain-time diagrams is identical to that applied early for copper A) and B). The model curves in Fig. 4.12 are obtained via Eqs. (4.2.9), (4.2.7), and (4.2.4) with the following parameters:

$\sigma_P = 4.8$ MPa, $B = 3.1 \times 10^{-1}$, $p = 2.5 \times 10^{-4}$ s^{-1}, $r = 1.1 \times 10^{3}$ MPa^2, $A_1'' = 1.8$ MPa$^{1-A_2}$, $A_2 = 2$, and $w = 6.0 \times 10^{-4}$ s^{-1}.

Since the ultrasound acts from the very beginning of the experiment, i.e., $|\vec{e}| = 0$ in Eq. (4.2.4), constant A_1' is not used here. Again, one can see that ultrasound increases creep deformation, which is in full accordance with the experiment.

4.2.4 Creep coupled with ultrasound – general case

To complete the modeling of the ultrasound-assisted creep, Formulae (4.2.1)-(4.2.4) must be supplemented by that governing the effect of ultrasound on the steady-state creep deformation. Since, in terms of the synthetic theory, function K regulates the primary creep rate, we propose to introduce a linear term of oscillating stress amplitude:

$$K_U = K + A_3 S_m^{A_4}, \tag{4.2.15}$$

where K is defined by (3.2.3). The logic of adding $A_3 S_m^{A_4}$ is to model the experimentally recorded increase in the ultrasound-assisted secondary creep. This term expresses the power section of acoustic energy alone because its temporary part tends to zero as the long-termed processes such as secondary creep are considered.

Considering the results from the previous section and formula (4.2.15), the relationship (3.3.19) accounting for the action of ultrasound takes the following form

$$e_{CreepU} = \sqrt{\frac{2}{3}} a_0 \left[\Phi(b_U) - \Phi(b_{UM}) + \left(K + A_3 S_m^{A_4}\right) \Phi\left(\frac{S_P}{\sqrt{S_1^2 + \left(A_1 {S_m}^{A_2}\right)^2}} \right) t \right], \tag{4.2.16}$$

where (in the case of uniaxial tension and longitudinal sonication) b_U is defined by (4.2.7) and b_{UM} is from (4.2.7) as $t = 0$.

The value of b_U for the steady steady-state creep is obtained from (4.2.7) as the exponential functions tend to zero:

$$b_U = \frac{\sigma_p}{\sqrt{\sigma^2 + (A_1 {\sigma_m}^{A_2})^2}}. \qquad (4.2.17)$$

Comparing (4.2.7) and (4.2.17) to (3.3.10), it is easy to conclude that $b_U < b$ for both primary ($I > 0$) and secondary ($I \to 0$) portions. This inequality immediately means that $e_{CreepU} > e_{Creep}$, which is caused by the extension of formulae (3.2.3) and (3.1.14) by the terms the action of ultrasound, formulae (4.2.1) and (4.2.15).

Figure 4.13 shows the loading surfaces in uniaxial tension for ordinary (the left column) and ultrasound-assisted creep (the right column). Three positions are considered:

a) the start of creep deforming (for simplicity, we assume that the amount of plastic deformations cumulated prior to the creep is identical),
b) primary creep,
c) secondary creep.

As is seen from this figure, $\beta_1 > \beta_{1U}$ for both portions of the creep, meaning that, due to the action of ultrasound, the amount of slip systems involved in time-dependent plastic flow is greater than that for ordinary loading.

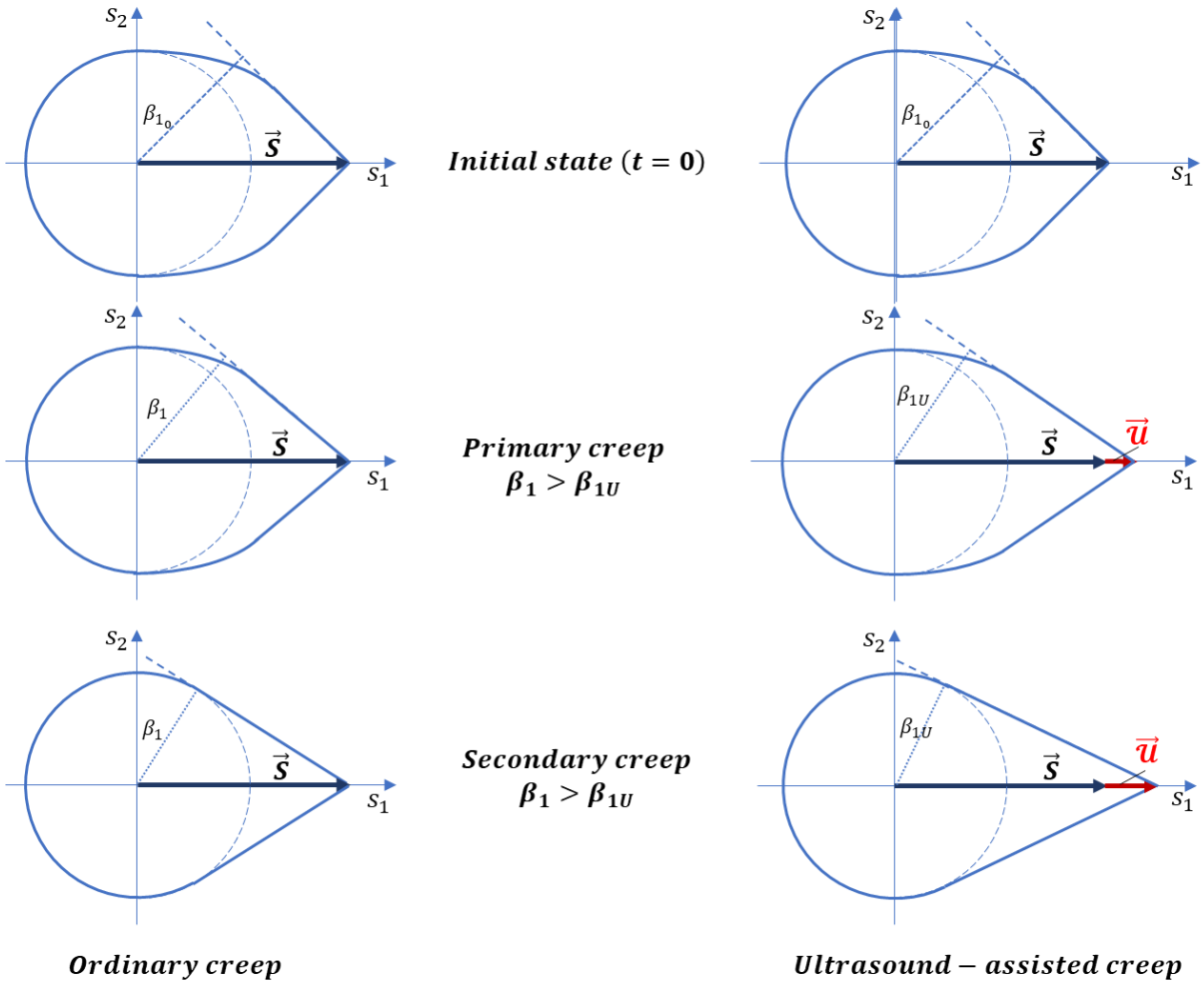

Fig. 4.13 Loading surface for creep in uniaxial tension

4.2.5 Results. Discussion

This point aims to plot ultrasound-assisted strain~time curves for aluminum and compare the model results to experimental observations. The experiments were conducted in two regimes (Kulemin, 1978):

(i) Ordinary creep under the action of tensile stress $\sigma = 10$ MPa.

(ii) Simultaneous action of tensile stress $\sigma = 10$ MPa, and longitudinal oscillating stress of various amplitudes: $\sigma_{m1} = 0.6$ MPa, $\sigma_{m2} = 1.3$ MPa, and $\sigma_{m3} = 2.0$ MPa.

A) To plot the ordinary creep diagram, we utilize formulae (3.3.17) and (3.3.10). To achieve the best fit between the analytic and experimental results, we propose the following values of the parameters standing in these formulae:

$\sigma_p = 5$ MPa, $B = 2.31 \times 10^{-1}$, $p = 2.5 \times 10^{-4}$ s^{-1}, $K = 1.0 \times 10^{-5}$ s^{-1}, and $r = 1.0 \times 10^{3}$ MPa^2.

As a result, Line 1 in Fig. 4.14 shows good agreement with the experimental one.

B) By formulae (4.2.16), (4.2.15), and (4.2.7) with model constants

$A_1 = 1.28\ \text{MPa}^{1-A_2}$, $A_2 = 2.0$, $A_3 = 1.5 \times 10^{-5}\ (\text{MPa}^{A_4} \times \text{s})^{-1}$, $A_4 = 1.0$, and $w = 2.1 \times 10^{-3}\ \text{s}^{-1}$

An analytical creep diagrams plotted in the presence of ultrasound. Lines 2-4 in Fig. 4.14 demonstrate good agreement between the theoretical and experimental results. It must be stressed that the model constants used for Line 1 in Fig. 4.14 (see above) remain actual here.

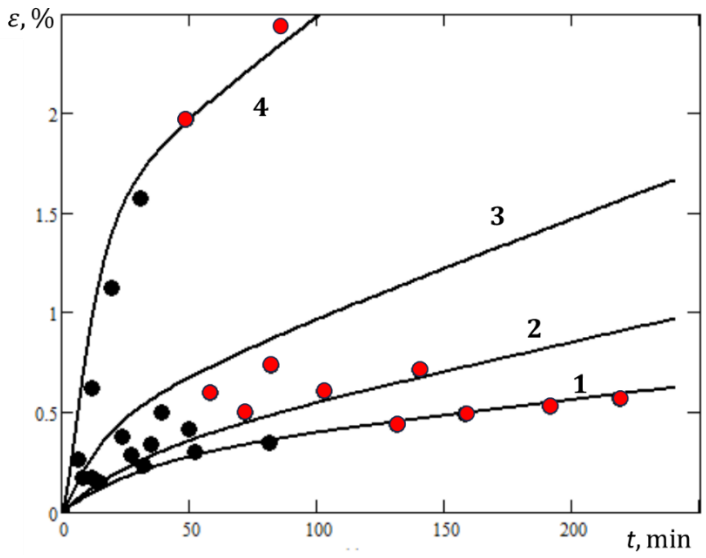

Fig. 4.14 Creep diagrams of aluminum in uniaxial tension ($\sigma = 10$ MPa, $T = 40$°C), 1 – ordinary creep, 2-4 ultrasound-assisted creep with oscillating stress amplitudes of 0.6 MPa (2), 1.3 MPa (3), and 2.0 MPa (4); • – experiment (Kulemin, 1978), lines – model.

Fig. 4.15 demonstrates the temporary behavior of the angles for boundary tangent planes – calculated via Eqs. (3.3.10) and (4.2.7) – located at the endpoint of the stress vector for the experiment in Figure 4.14. This figure correlates with Fig. 4.13, indicating the expansion of active slip systems, i.e., the increase in both portions of creep deformation due to the ultrasound.

A question may arise as to whether the term $A_3 {S_m}^{A_4}$ in Eq. (4.2.35) is needed to model the ultrasound-assisted secondary creep because the term $A_1 {S_m}^{A_2}$ leads to the increase of Φ as well. To answer this question, plot strain~time diagrams via formulae (4.2.16), (4.2.15), and (4.2.7) at $A_3 = 0$.

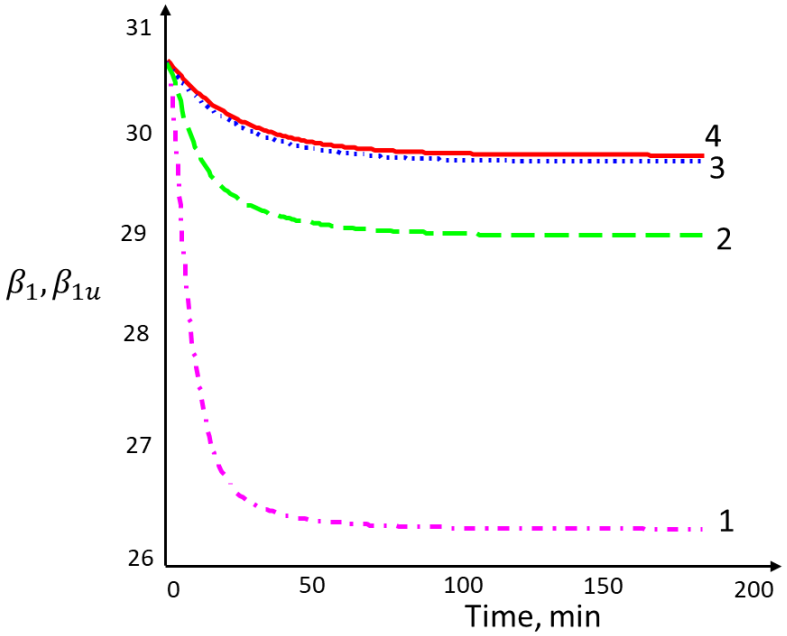

Fig. 4.15 Boundary angles β_1 (4) and β_{1U} (3-1) for active slip systems

As shown in Fig. (4.16), the result is unsatisfactory. The increase in the slope of the linear portion is much less than that from the experiment. Therefore, the addition of $A_3 {S_m}^{A_4}$ to K, which is responsible for the growth of secondary creep in the ultrasonic field, is vital. In confirmation of that, Fig. 4.17 shows the deformations' linear portions at various values of oscillating stress amplitudes. It is clear that ignoring the extension proposed in (4.2.15) results in a slight increase in the slope angle, while its presence shows much greater angle increments.

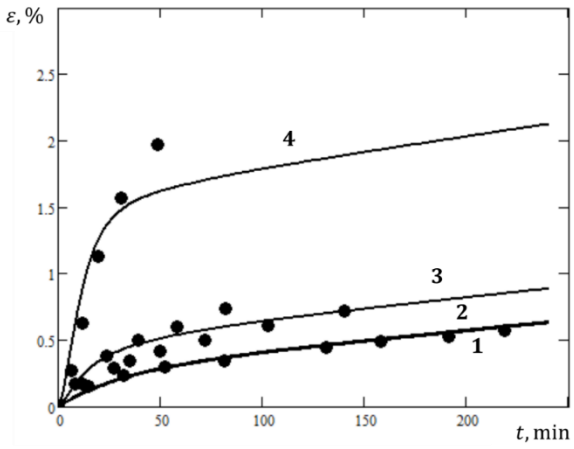

Fig. 4.16 Creep diagrams plotted via model relationships at $A_3 = 0$ (nomenclature is the same as in Fig. 4.14)

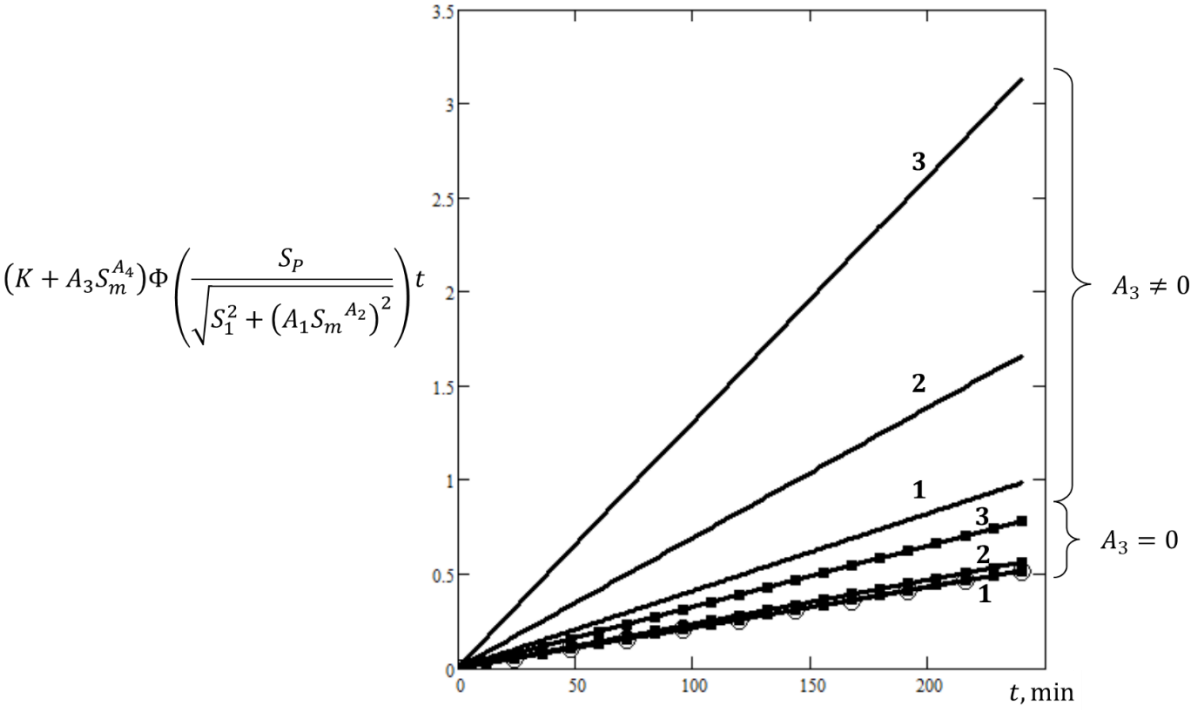

Fig. 4.17 Linear portions from Eq. (4.2.16) at amplitudes $\sigma_{m1} = 0.6$ MPa, $\sigma_{m2} = 1.3$ MPa, and $\sigma_{m3} = 2.0$ MPa; ○ – ordinary creep.

4.2.6 The extension of the synthetic theory for the case of ultrasonic recovery of the work-hardened material

Consider the following sequence of operations:

(i) plastic deforming of a specimen by unidirectional load,
(ii) unloading,
(iii) sonication of the work-hardened specimen.

The Synthetic theory uses the differential equation (3.2.7) to model the defect relaxation for the post-deformed material. The solution of Eq. (3.2.7) is

$$\psi_N = \psi_{N0}\exp(-Kt), \tag{4.2.18}$$

where ψ_{N0} the number of defects cumulated in the material during plastic deforming, Eq. (3.2.6).

Formula (4.2.18), together with (3.1.14)[4], means that the tangent planes move towards the origin of coordinates:

$$H_N = \sqrt{S_S^2 + \psi_{N0}\exp(-Kt)}. \tag{4.2.19}$$

To adopt Eq. (4.2.19) for modeling the phenomenon that acoustic energy leads to the recovery of work-hardened materials' mechanical properties, we propose the following.

Since the ultrasonic recovery experiments were held at the stress-free state, the function K defined via Eq. (3.2.3) is inapplicable because $K = 0$ at $\tau_0 = 0$ and we obtain no change in H_N. Further, since the thermally activated processes at room temperature exert a feeble effect, we need to insert into the function K a term that expresses the recovery processes induced by ultrasound.

We replace the function K from (3.2.3) by

[4] We use here (3.1.4) with the yield strength S_S and $I_N = 0$.

$$K_U = K + A_1(S_m H_{\max})^{A_2}, \tag{4.2.20}$$

where S_m is the oscillating stress vector amplitude, $H_{\max}$ is the maximum plane distance for the whole loading history, A_1 and A_2 are the model constant to be chosen for the best fit between the analytic and experimental results. It is clear that $K_U = K$ in the absence of ultrasonic energy ($S_m = 0$), i.e., we return to the formula (3.2.3).

Therefore now the degree of hardening – the plane distances in terms of the synthetic theory – obeys the following relationships:

$$H_{NU} = \sqrt{S_S^2 + \psi_{N0}\exp(-A_1(S_m H_{\max})^{A_2} t)}, \tag{4.2.21}$$

where t is the sonication duration.

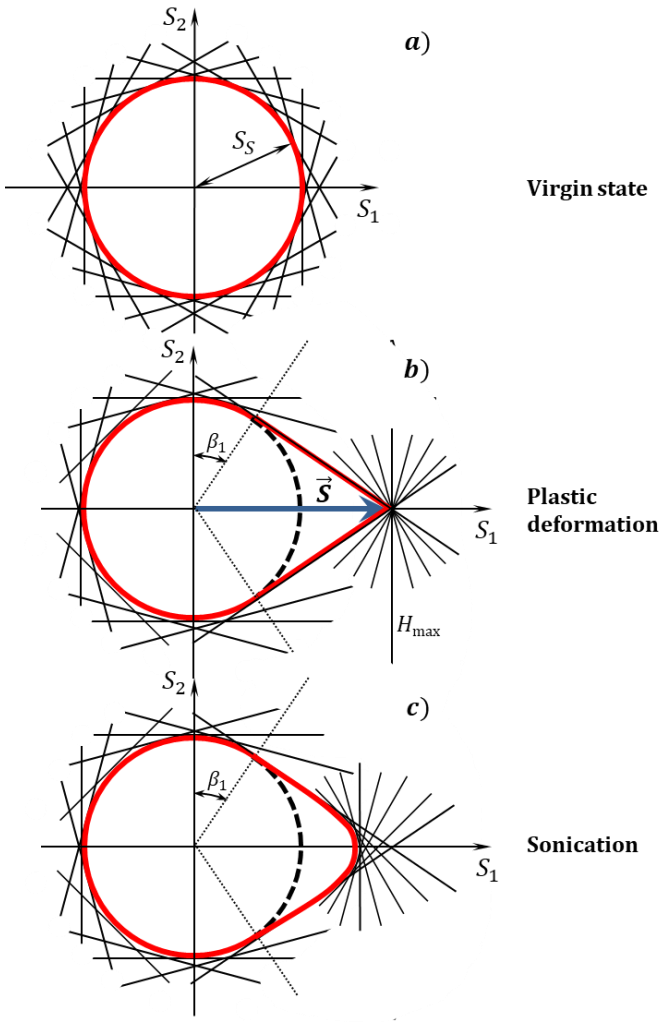

Fig. 4.18 Yield and loading surface in terms of the synthetic theory in S_1-S_2 coordinate plane for uniaxial tension ($\lambda = 0$)

Let us analyze the modification proposed in Eqs. (4.2.20)-(4.2.21) and check them against the experimental observations. The appearance of a term depending on the intensity of sonication (S_m) in the function that governs the decrease of the plane distances reflects the experimental fact that the acoustic energy can induce alone the recovery processes in plastically deformed materials. Further, we define K_U via the product $S_m H_{\max}$ to reflect another experimental fact, the greater strain hardening (plastic deformation) values lead to more intensive recovery during the sonication at a given ultrasound intensity and duration.

Consider the case when longitudinal vibrations ($S_m = \sqrt{2/3}\,\sigma_m$) are applied to the material plastically deformed in uniaxial tension. Under these conditions, $H_{\max}$ is the distance to the plane perpendicular to the static stress vector $\vec{\boldsymbol{S}}$ (Fig. 4.18b) determined via formula (3.1.11) at $\beta = \pi/2$ and $\lambda = 0$:

$$H_{\max} = S_1 N_1 = \sqrt{2/3}\,\sigma. \tag{4.2.22}$$

So $H_{\max}$, via σ, bears in itself the information on the degree of plastic deformation.

Therefore the plane distances during ultrasonic vibration are

$$H_{NU} = \frac{2}{3}\sqrt{\sigma_S^2 + [(\sigma \sin\beta \cos\lambda)^2 - \sigma_S^2]\exp\left[-A_1\left(\frac{2}{3}\sigma_m\sigma\right)^{A_2} t\right]}, \tag{4.2.23}$$

where the non-zero values of ψ_{N0} are from (3.3.4) (see the boundary angle β_1 in Fig. 4.18). The formula above analytically describes the decrease in the plane distances (Fig. 4.18c), i.e., the recovery of strain-hardened material in the ultrasonic field.

The change in the yield stress due to the ultrasound (σ_{SU}) is calculated via (4.2.23) as

$$\sigma_{SU} = H_{NU}\left(\beta = \frac{\pi}{2}, \lambda = 0\right). \tag{4.2.24}$$

4.2.7 Results. Discussion

To inspect the modifications proposed above, let us compare model results with experimental data (Kulemim, 1978) on the temporary decrease of Vickers hardness number (*HV*) of aluminum specimen plastically deformed in uniaxial tension on two values: $\varepsilon_1 = 3.6$ % and $\varepsilon_2 = 6.8$ % (Fig. 4.19). The sonication of the strain-hardened specimen is conducted by the longitudinal oscillation of amplitude

$\sigma_m = 10$ MPa. Both the plastic deforming and the sonication take place at room temperature. To relate the value of HV to the yield strength in uniaxial tension σ_S, we address the results on the correlation between Vickers hardness number and yield strength for aluminum, which states that $HV = 17.4$ corresponds to $\sigma_S = 23.4$ MPa (Arbtin and Murphym, 1953). We preserve the relation $R \equiv HV/\sigma_S = 0.744$ not only for the start of plastic deforming but for formula (4.2.24) as well:

$$HV = R \cdot \sigma_{SU}. \tag{4.2.25}$$

To apply the formulae proposed above, first, we must choose the constant r to ensure that it gives the correct HV for the plastically deformed specimens. For this purpose,

(i) we utilize formulae (3.3.5)-(3.3.7), which give $\varepsilon \sim \sigma$ relation;

(ii) from the $\varepsilon \sim \sigma$ relationships, we take those values of the stresses ($\sigma_1 = 31.0$MPa and $\sigma_2 = 33.6$ MPa) that correspond to $\varepsilon_1 = 3.6$ % and $\varepsilon_2 = 6.8$ %;

(iii) utilizing (3.2.6), we calculate ψ_{N0} for σ_1 and σ_2;

(iv) formulae (4.2.23)-(4.2.25) at $t = 0$ give the values of HV for the plastic deformation caused by σ_1 and σ_2.

As a result, we obtain two points on the $HV \sim t$ diagram at $t = 0$.

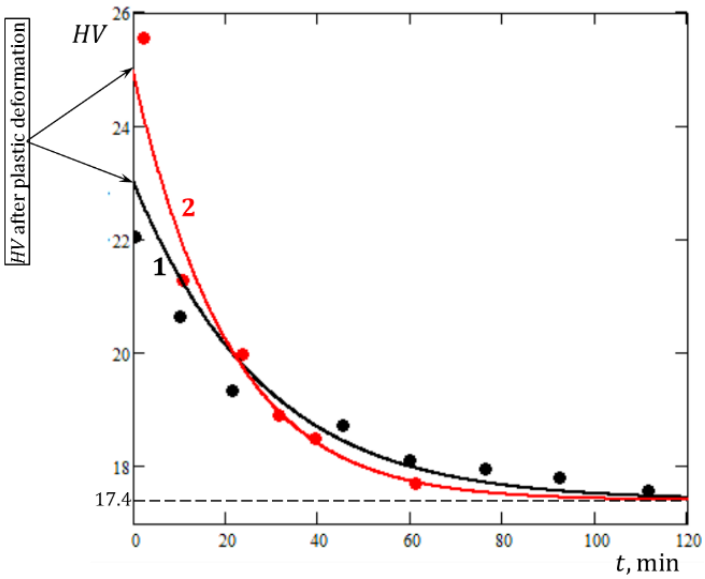

Fig. 4.19 *HV* vs. *sonication time* plots for the plastically deformed aluminum specimen: $\varepsilon_1 = 3.6$ % and $\varepsilon_2 = 6.8$ %. ● – experiment (Kulemim, 1978), lines – model

The next step is to model the decrease in HV as a function of sonication time by formulae (4.2.23)-(4.2.25) for $t > 0$. Fig. 4.19 demonstrates the model $HV \sim t$ curves constructed at the following constants' values: $A_1 = 7.136 \times 10^{14}\left(\mathrm{MPa}^{2A_2} \cdot \mathrm{s}\right)^{-1}$, $A_2 = 4.0$. Similarly to the experiment, the model curve at $\varepsilon_2 = 6.8$ % shows a quicker decrease in HV than that at $\varepsilon_1 = 3.6$ %. It is in full accordance with the experimental fact that the initial strain hardening increase boosts the acoustic field's recovery processes.

The results regarding section 4.2 are published in

Rusinko, A. & Alhilfi, A. (2021)
Rusinko, A. Alhilfi, A., Rusinko, M. (2022)
Ruszinko, E. & Alhilfi, A. (2021)

Thesis II

In terms of the Synthetic theory, a model for the analytical description of the ultrasound-assisted time-dependent deformation processes has been developed. The obtained results show good conformity between the model and experimental data for the following phenomena:

(i) The increase in primary creep under the periodic and continuous action of ultrasound

(ii) The increase in secondary creep in an acoustic field

(iii) Ultrasound-induced relaxation (recovery) of the work-hardened materials.

4.3 Extension of the Synthetic theory to the ultrasound-assisted phase transformations

4.3.1 Effect of ultrasound impulses on the austenite transformation

This section deals with the transformation plasticity (austenite transformation), during which ultrasonic impulses are applied to the material (Fig. 4.20). There are two goals to be achieved here:

(i) to derive formulae for describing the course of $\varepsilon \sim T$ curve in the presence of ultrasound impulses (see Fig. 2.30) and

(ii) to give a relationship for the distribution of the magnitude of the strain-drops caused by ultrasound impulses (Fig. 2.31)

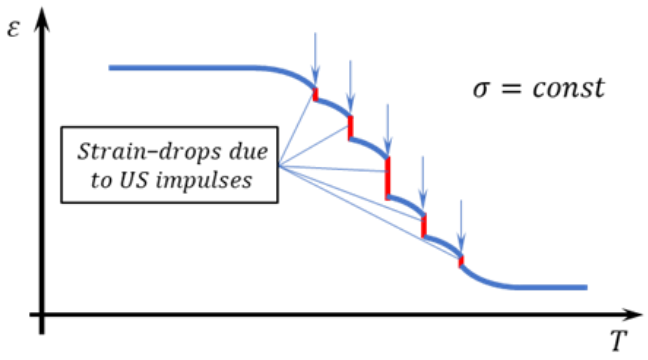

Fig. 4.20 Schematic plot of austenite transformation in the presence of ultrasound (arrows indicate the moments of ultrasonic impulses

Since effective temperature is the most crucial factor in the progress of phase transformation – T_e directly influences the values of Φ and φ_N via Eqs. (3.4.1) and (3-4-4) –, we propose to extend Eq. (3.4.5) by a term reflecting the presence of ultrasound. Following the observations on the effect of ultrasound on austenitic transformation, we propose to shift (increase) the value of effective temperature by a term (U) representing the ultrasound action:

$$T_e = T\left(1 - D\vec{\boldsymbol{S}} \cdot \vec{\boldsymbol{N}}\right) + U. \qquad (4.3.1)$$

We decompose the U on two components, functions f and g, to reflect the mechanical and thermal impact of acoustic energy on the kinetics of the austenitic transformation.

$$U = \left(B + e^{-w(T-T_i)}\right) \int_{A_s}^{T} (f \cdot g) dt, \tag{4.3.2}$$

where T_i are the temperatures as ultrasound is On; w and B are model constants.

The function f points out the assisting action of ultrasound due to the generation of alternating stresses that induce and intensify the movement of interface and martensitic domain boundaries. We define f as

$$f(S_m) = U_1\left(\vec{\boldsymbol{S}}_m \cdot \vec{\boldsymbol{N}}\right), \tag{4.3.3}$$

where U_1 is the model constant and S_m is a stress vector whose components are formed via Eq. (3.1.1) by the values of alternating stress amplitudes. Considering short-termed ultrasound impulses, f is assumed to increase jump-wise as the ultrasound is On. Then it decreases, stabilizing at some value after the ultrasound is Off. The overall effect of the ultrasonic impulses is an increase in f. Although $S_m = 0$ between the ultrasound impulses, $U > 0$ throughout the transformation due to the integration in (4.3.2) that cumulates positive values during the sonication.

We propose the term $U_1\left(\vec{\boldsymbol{S}}_m \cdot \vec{\boldsymbol{N}}\right)$ in (4.3.3) to comply with experimental data stating that the magnitude of the strain jumps is proportional to stress amplitudes (S_m), and the effectiveness of ultrasound varies depending on the orientation of the microregion considered. It is the scalar product $\vec{\boldsymbol{S}}_m \cdot \vec{\boldsymbol{N}}$ that reflects the effectiveness of the ultrasound action for a given orientation.

The presence of $\left(B + e^{-w(T-T_i)}\right)$ in (4.3.2) reflects the experimental fact that after ultrasound is Off, the so-called aftereffect is recorded, consisting of some deformation increase. As $e^{-w(T-T_i)} \to 0$, the further realization of SME takes place according to the austenite transformation kinetics, although shifted by B. To summarize, the effect of ultrasound manifests itself in the recoverable and irrecoverable portions of phase deformation.

In order to catch the experimental observation recording that the strain-jump magnitude strongly depends on the temperature when ultrasound is applied, we propose the function $g(T)$ from (4.3.2) in the form of the Agnesi curve:

$$g(T) = \frac{a^3}{a^2 + (T - C)^2}. \tag{4.3.4}$$

While the function f leads to uniform strain increments at a given ultrasonic intensity, the function g gives different strain-jump magnitudes depending on the transformation stage when the acoustic energy

acts. The model constants a and C from (4.3.4) reflect the material's compliance to react to the ultrasonic impact at different moments of the transformation.

Fig. 4.21 demonstrates the $U(T)$ plot, which shows its step-wise increments at the temperatures as the ultrasound is On. The magnitudes of these increments vary with the temperature.

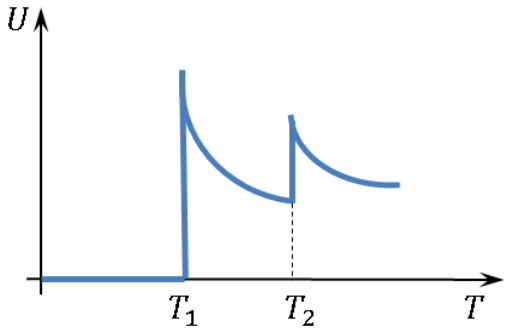

Fig. 4.21. Dependence of U on temperature; ultrasonic impulses are applied at $T = T_1$ and $T = T_2$.

Consider heating a material subjected to constant uniaxial stress (σ) from its full martensite state ($\Phi = 1$). Let an impulse of longitudinal ultrasound at a given temperature be applied. In this case, the vector S_m, according to (3.1.1), has components $\left(\sqrt{2/3}\,\sigma_m, 0,0\right)$, where σ_m is the amplitude of oscillating tension-compression stress.

Now, the strain intensity, on the base of Eqs. (3.4.11) and (4.3.1)-(4.3.4), is

$$r\varphi_{NU} = -\left(T - A_f\right) + (TDS - U)\sin\beta\cos\lambda, \qquad (4.3.5)$$

where $S = \sqrt{2/3}\,\sigma$.

It is clearly seen due to the term U in (4.3.5) that φ_{NU} takes less value compared to that from (3.4.11), which correctly catches the experimental result saying that ultrasound energy causes a negative increment in the deformation.

The shape memory deformation (e_u), according to Eq. (3.1.8), takes the following form (the integral over α gives 2π)

$$e_u = \frac{\pi}{r}\int_0^{\lambda_{1U}}\int_{\beta_{1U}}^{\pi/2}\left[-\left(T - A_f\right) + (TDS - U)\sin\beta\cos\lambda\right]\sin 2\beta\cos\lambda\, d\lambda\, d\beta. \qquad (4.3.6)$$

The boundary angles in (4.3.6) are

$$\cos\lambda_{1U} = \frac{1}{(DS-U)\sin\beta}\left(1-\frac{A_f}{T}\right), \qquad \sin\beta_{1U} = \frac{1}{(DS-U)}\left(1-\frac{A_f}{T}\right). \tag{4.3.7}$$

Like in Eq. (3.4.12), we assume that $T > A_f$. Otherwise, we let $\beta_{1U} = 0$ and $\lambda_{1U} = \pi/2$.

Fig. 4.22 gives a comparison between $\varphi_{NU}{\sim}T$ and $\varphi_N{\sim}T$ plots, which demonstrate entire agreement with experimental observations:

a) strain intensity (therefore, deformation) gains a negative-signed increment at the moment of ultrasound impulse,
b) after some interim period, it follows the kinetics of austenite transformation but with irrecoverable reduction.

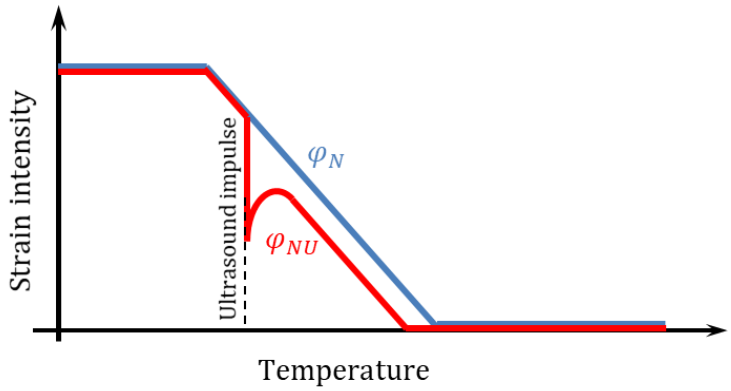

Fig. 4.22. Strain intensity vs. temperature for an ordinary (φ_N) case and with ultrasound (φ_{NU}).

Summary.

To mirror the fact that ultrasound induces the deformation recovery on heating, i.e., intensifies the shape memory deformation, we have introduced the term U in Eq. (4.3.5), which reflects the promoting action of ultrasound within microelements. In an instant as ultrasound On, the deformation yields a negative increment and, after a short disturbance, follows the kinetics of austenitic transformation. Another effect from U is that the amount of material involved in the transformation increases due to ultrasonic impulse, i.e., by comparing (3.4.12) and (4.3.7), we have $\lambda_{1U} < \lambda_1$ and $\beta_{1U} > \beta_1$. Besides, formula (4.3.4) governs the magnitude of the strain jump depending on the temperature of ultrasonic insonation.

Summing the strain intensities in all the micro volumes taking part in the austenitic transformation, Eq. (4.3.6), we obtain the deformation on the macroscopic scale.

Since acoustic energy boosts the phase transformation, it ends at less temperature than the ordinary shape memory effect – in Fig. 4.22, the φ_{NU} line reaches sooner than φ_N the zero value.

Figure 4.23 demonstrates the change in the boundary angle β_1 that determines the region where the strain intensity is non-zero from the martensite ($\Phi = 1$, $\beta_1 = 0$) up to the austenite state ($\Phi = 0$, $\beta_1 = \pi/2$). t Ultrasound impulse results in the step-wise increase of his angle: from β_1 (3.4.12) to β_{1U} (4.3.7).

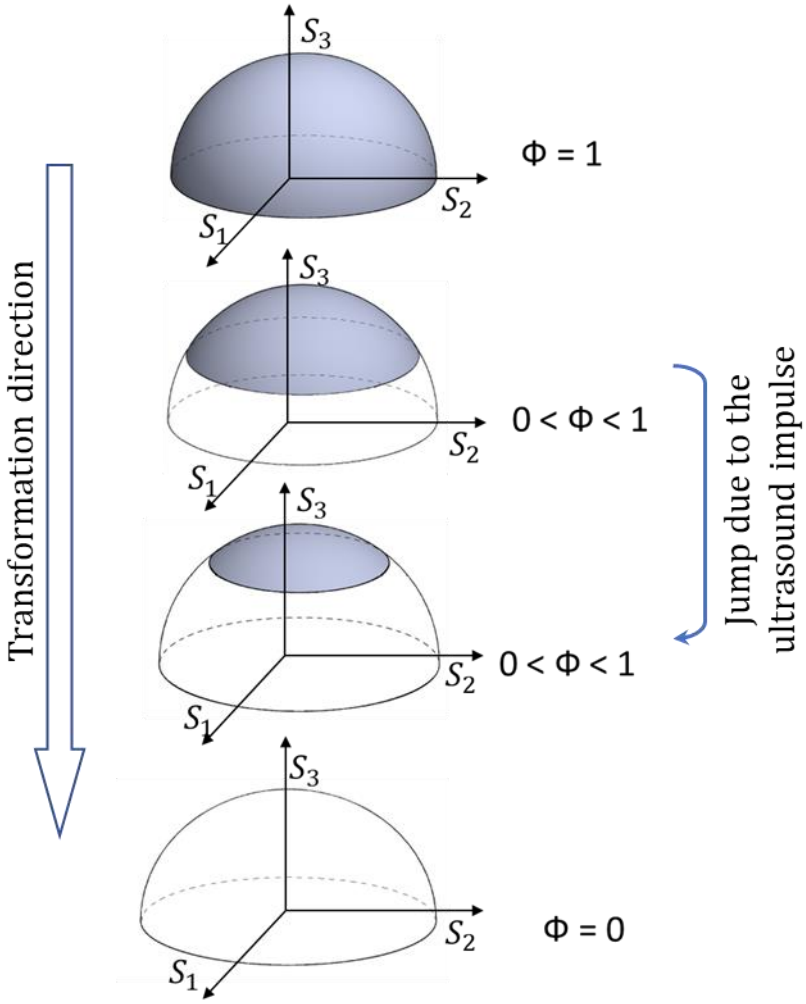

Fig. 4.23 The change in the integration domain during austenite transformation with one ultrasound impulse.

If to set the task of modeling the ultrasound-induced strain drops alone, i.e., we are not interested in the development of the transformation between the ultrasound impulses, we ignore the bracket in the formula (4.3.2):

$$U = \int_{A_s}^{T} (f \cdot g) dt. \tag{4.3.8}$$

In this case, U , being the product of f Fig. 4.24a and g Fig. 4.24b, takes the step-shaped form Fig. 4.24c with different magnitudes of the steps. Together with Eq. (4.3.5), it correctly reflects the experimental requirements – a) ultrasonics impulses cause the negative increments in the strain intensity. b) the magnitude of these increments varies with the temperature, having the greatest value in the middle of a transformation.

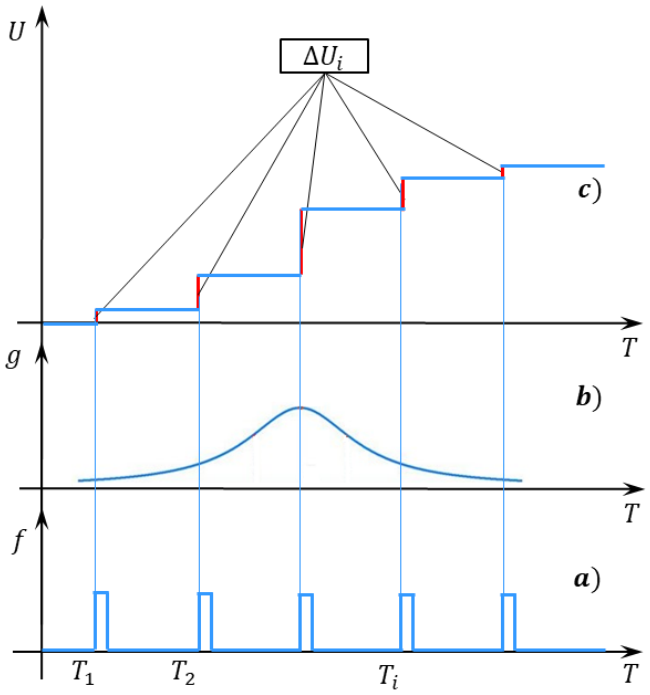

Fig. 4.24 Schematic plots of functions from Eqs. (4.3.2)-(4.3.4) at $\beta = \pi/2$ and $\lambda = 0$.

The increment in the strain intensity due to the ultrasound impulses, according to Eq. (4.3.5), is

$$r\Delta\varphi_{NU} = -\Delta U \tag{4.3.9}$$

Taking into account (4.3.2) and (4.3.8), the above formula, i.e., the negative strain intensity jumps caused by ultrasonic longitudinal impulses of equal intensity (amplitude) and duration at temperatures T_i are written as follows

$$r\Delta\varphi_{NUi} = -U_1 \frac{2}{3} \sigma_m \sin\beta \cos\lambda g(T_i) \Delta T \tag{4.3.10}$$

where ΔT is the temperature range when ultrasound is On.

To calculate the increment in deformation, we utilize Eq. (3.1.8):

$$\Delta e_{Ui} = \pi \int_0^{\pi/2} \int_0^{\pi/2} \Delta\varphi_{NUi} sin2\beta cos\lambda d\lambda d\beta \qquad (4.3.11)$$

The formula above matches experimental recordings: a) acoustic energy enhances shape memory deformation by generating a negative increase in deformation, b) the magnitude of the deformation increments is proportional to the sonication intensity, and c) the effect of ultrasound impulses depends on the stage of austenitic transformation when the ultrasound is switched on.

Therefore, the extension of the synthetic theory expressed in this section leads to a qualitative correspondence with experiments. The next step is to inspect its quantitative correctness.

4.3.2 Results. Discussion

$\varepsilon \sim T$ diagram in the ultrasound field

Here, our goal is to plot $\varepsilon \sim T$ diagram of NiTi alloy at fixed static stress subjected to ultrasonic insonation and compare it with the experiment. Characteristic temperatures of the alloy measured by differential scanning calorimetry were: $A_s = 323$ K, $A_f = 349$ K (Rubanik et al., 2008). The procedure of tests was the following. The wire sample in the high-temperature austenite was subjected to load (uniaxial tension $\sigma = 30$ MPa that results in deformation of 1.9%) with subsequent cooling. After cooling, the sample was brought into austenitic condition by heating. The heating was performed at a rate of 1 K/min. Two ultrasonic impulses (each of 9 sec) with vibrational amplitude $A = 5$ μm and frequency $f = 22.2$ kHz were produced in the temperature range A_s-A_f. The first ultrasonic impulse was produced at $T_1 = 340$ K, and the second at $T_2 = 373$ K.

To calculate the alternating stress amplitudes σ_m, we utilize Eq. (4.1.20). Taking into account that these are temperature functions, further throughout, we utilize their average values for A_s-A_f diapason: $E = 62$ GPa, $c = 5200$ m/s (Bradley, 1965). As a result, from (4.1.20), we have $\sigma_m = 8.3$ MPa.

First, we plot the $\varepsilon \sim T$ diagram for the shape memory effect with the above data without ultrasonic action. To do this, we use Eqs. (3.4.11)-(3.4.13) for plotting line 1 in Fig. 4.22 with the following model constants: $D = 4.2 \times 10^{-3}$ MPa^{-1} and $r = 4.9 \times 10^2$ K. At least for the temperature diapason 290-340 K, i.e., before the first ultrasonic impulse, we can conclude that the model curve shows good agreement with the experiment.

The next step is the $\varepsilon{\sim}T$ diagram in the presence of ultrasonic impulses (line 2 in Fig. 4.25). Formulae (4.3.1)-(4.3.7) give the strain drop values shown in Table 4.1. The model results have been obtained with the following values of constants: $w = 1.32 \times 10^{-1}\text{K}^{-1}$, $U_1 = 13.83\ (\text{K} \cdot \text{MPa})^{-1}$, $a = 4.0$ K, $C = 360$ K, $B = 4.79 \times 10^{-1}$. It must be stressed that the values of constants D and r stay the same as in the previous paragraph. The magnitude of the strain jump at the first impulse is much greater than that at the second. The reason is that the first impulse is done near the middle of the transformation while the second is closer to its end. The same result is obtained analytically because of the function $g(T)$ (4.3.4), where the constant C regulates the temperature of the greatest increment in the deformation caused by ultrasound. Therefore, the magnitude of strain jumps is governed by constants U_1 in $f(S_U)$ and a in $g(T)$, and the constant C in $g(T)$ regulates the temperature of the maximum ultrasound effect.

The kinetics of $\varepsilon{\sim}T$ after switching off of ultrasound is also in full accordance with experimental results. Namely, after the strain jump, the model result shows some increase in the deformation, after which the deformation on heating develops according to the reverse transformation kinetics. This result is due to the term $\left(B + e^{-w(T-T_i)}\right)$ in (4.3.2) Here, constant w governs the duration of the deformation's increase following the ultrasonic action, and B expresses an irrecoverable portion of deformation caused by ultrasound. Thus, the model accounts for another experimental fact stating that the ultrasound-assisted transformation ends at lower temperatures. In our case, the second ultrasonic impulse results in such a drop in deformation that the material achieves a fully austenitic state when the further temperature increase results in no deformation variation. So, we read from Fig. 4.25 that the finish temperature after two acoustic impulses is 373 K, while the ordinary $\varepsilon{\sim}T$ diagram stops its variation at about 400 K.

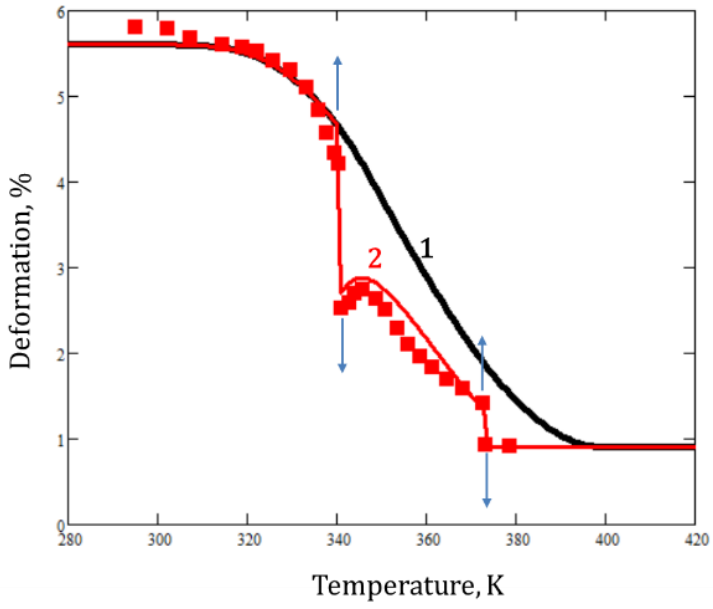

Fig. 4.25 State diagram of NiTi alloy in deformation-temperature coordinate. The sample is subjected to uniaxial tension $\sigma = 30$ MPa. The arrows show the moments of switching-on (↑) and switching-off (↓)of ultrasonic vibrations; ■ –experiment (Rubanik et al., 2008), lines – model.

Table 4.1 Strain drops due to ultrasound impulses

	Experiment	Model	Relative error, %
1st impulse	1.675	1.973	+15.1
2nd impulse	0.493	0.445	–9.7

In summary, we may conclude that the extension of the synthetic theory leads to qualitatively and quantitatively correct results.

Ultrasound-induced strain drops

Here, our goal is to calculate the ultrasound-induced drops of deformation during the austenitic transformation in Ni-Ti alloy at fixed stress and compare them with the experimental results, Fig. 4.26.

Characteristic temperatures of the alloy measured by differential scanning calorimetry were $A_s = 356$ K and $A_s = 390$ K (Steckmann et al., 1999). The stress state of the experiment was uniaxial tension ($\sigma = 100$ MPa $= const$). The initial state was martensite, $\Phi = 1$. Then, during the heating, longitudinal ultrasound impulses were superimposed at the following temperatures $T_i = 370{,}373{,}377{,}380{,}383$ K. The amplitude of ultrasonic deformation at every sonication was $\varepsilon_m = 5 \times 10^{-5}$. The amplitude of oscillating stress is calculated as $\sigma_m = E\varepsilon_m$. The Young modulus ($E$) of MSA strongly depends on the stage of transformation. Thus, for Ni-Ti alloy $E_s = 28$ GPa as $\Phi = 1$ and $E_f = 84$ GPa as $\Phi = 0$. By applying linear interpolation between two pairs of the values of E_s, A_s and E_f, A_f, we obtain the following values of the Young moduli for the temperatures T_i: E_i = 49, 57, 63, 67, 72 GPa. As a result, we obtain the following values for σ_{mi}: 2.5, 2.8, 3.2, 3.4, 3.6 MPa.

The drops of the deformation are calculated via Eqs. (4.3.10) and (4.3.11). To make calculations by this formula, we need to choose the model constants U_1, a, and C standing in Eqs. (4.3.8) and (4.3.4) so that the model result fits the experimental one as much as possible. While the model constant U_1 governs the

magnitude of the strain jump as a function of oscillating stress amplitude; the constants a and C regulate the position of the most significant effect from the acoustic impulses.

Fig. 4.26 demonstrates the deformation drops caused by acoustic impulses. The model results are obtained via Eqs. (4.3.10) and (4.3.11) at the following values of the model constants: $U_1 = 8.5 \times 10^{-2}$ $(\mathrm{K} \cdot \mathrm{MPa})^{-1}$, $a = 8.5$ K, $C = 377$ K. Constants r and D, responsible for conventional austenite transformation, are taken as $r = 375$ K, $D = 3 \times 10^{-5}$ MPa^{-1}.

It is easy to see from Fig. 4.26 that the model results correctly fit experimental data, allowing us to utilize the synthetic theory as a reliable instrument to predict the ultrasound-induced deformation drops in austenite transformation.

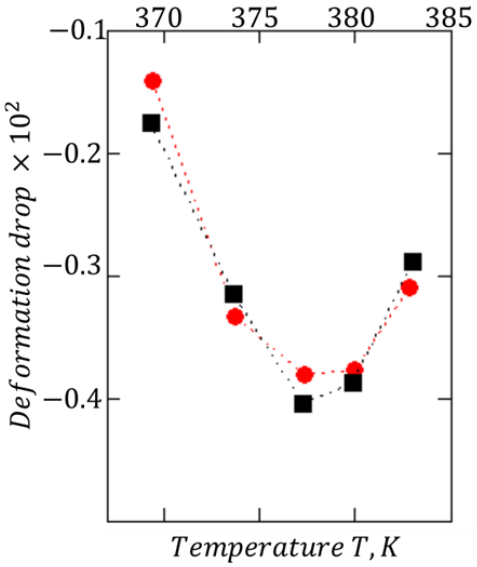

Fig. 4.26 Ultrasound-induced deformation drops in the course of austenitic reverse thermoelastic phase transformation; ● – experiment (Steckmann et al. 1999), ■ – model results via Eq. (4.3.11)

4.3.3 Extension of the Synthetic theory to the ultrasound-assisted pseudoelasticity (martensite transformation)

Consider the case when an SMA specimen in an austenite state is subjected to load at a constant temperature (T_0). The effect of pseudoelasticity results from martensite transformation occurring in the material, which leads to inelastic deforming for stresses beneath the material's yield strength.

This section aims to model the martensite transformation in the acoustic field, i.e., when the unidirectional and vibrating stresses act simultaneously from the beginning of loading.

Formula (3.4.15) says that the strain intensity in martensite transformation is related to the effective temperature as

$$r\varphi_N = M_s - T_e \tag{4.3.12}$$

Again, one can see that the effective temperature is the central element governing the development of deformation. In order to model the promoting effect of acoustic energy on the martensite transformation, i.e., to obtain the increase in the strain energy, we propose to shift (decrease) the effective temperature by a term that expresses the action of ultrasound:

$$T_e = T_0\left(1 - D\vec{\boldsymbol{S}} \cdot \vec{\boldsymbol{N}}\right) - U. \tag{4.3.13}$$

where U is proportional to the ultrasound energy (vibrating stress amplitude) and is proposed to be defined as

$$U = U_1\left(\vec{\boldsymbol{S}}_m \cdot \vec{\boldsymbol{N}}\right), \tag{4.3.14}$$

where the nomenclature is the same as in the previous section. The scalar product ($\vec{\boldsymbol{S}}_m \cdot \vec{\boldsymbol{N}}$) in formula (4.3.13) expresses the well-known fact that the effectiveness of ultrasound varies depending on the orientation of the microregion considered.

The term U inserted into Eq. (4.3.1) represents only an assisting effect of ultrasound upon the pseudoelasticity.

On the other hand, acoustic energy can decrease or increase the stress to be applied and increase the slope angle of the stress-strain curve (Malygin, 2001; Sapozhnikov et al., 1996). To account for this, we increase the value of the constant r, which is responsible for the slope angle of the stress~strain diagram, by $U_2|S_m|$. As a result, the ultrasound-assisted diagram inevitably crosses the ordinary one, which

symbolizes that the pseudoelastic deformation needs greater stresses starting from this point (see Fig. 2.32). A new constant, r_U, is related to r as

$$r_U = r + U_2|S_m|, \tag{4.3.15}$$

where U_2 is model constant. Formula (4.3.15) aligns with the increase in the hardening coefficient proposed by Sathish et al. (2013).

It is easy to see that as $S_m = 0$, i.e., in the absence of ultrasound, we arrive at the relationships to be applied to the modeling of ordinary pseudoelastic $\sigma \sim \varepsilon$ diagrams.

Consider a material in an austenitic state ($\Phi = 0$). Taking temperature constant (T_0), we load the material by simultaneous uniaxial tension and longitudinal vibration. In this case, according to Equation (3.1.8), the vector S_m, has components $(\sqrt{2/3}\,\sigma_m, 0,0)$, where σ_m is the amplitude of oscillating tension-compression stress.

According to Equations (3.4.15) and (4.3.12)-(4.3.15), the strain intensity with superimposed ultrasound (φ_{NU}) is

$$r_U\varphi_{NU} = M_s - T_0(1 - DS\sin\beta\cos\lambda) + U_1 S_m \sin\beta\cos\lambda. \tag{4.3.16}$$

Comparing φ_{NU} to the strain intensity from (3.4.15), it is easy to see that the presence of U on the right-hand side in (4.3.16) promotes the development of inelastic deformation. In other words, a given deformation value can be achieved with less stress because of compensating action of ultrasound energy.

The pseudoelastic deformation starts as

$$S_{\Phi U} = \frac{1}{D}\left[1 - \frac{M_s}{T_0} - \frac{U_1 S_m}{T_0}\right]. \tag{4.3.17}$$

The above formula is obtained from Eq. (4.3.13) via condition $T_e = M_s$, which is the same as $\varphi_{NU} = 0$ at $\beta = \pi/2$ and $\lambda = 0$.

Formula (4.3.17) testifies – $S_{\Phi U} < S_\Phi$ (3.4.16) – that the superposition of ultrasound lowers the value of static stress needed to induce martensite transformation/pseudoelastic deformation.

The pseudoelastic strain component (e_U), according to Equations (3.1.8) and (4.3.16), takes the following form in the presence of ultrasound

$$e_U = \frac{\pi}{r_U}\int_0^{\pi/2}\int_0^{\pi/2}[M_s - T_0(1 - DS\sin\beta\cos\lambda) + U_1 S_m \sin\beta\cos\lambda]\sin 2\beta\cos\lambda d\beta d\lambda. \quad (4.3.18)$$

The boundary angles in formula (4.3.18) are

$$\cos\lambda_{1U} = \frac{1}{\left(DS + \frac{U_1 S_m}{T_0}\right)\sin\beta}\left(1 - \frac{M_s}{T_0}\right), \quad \sin\beta_{1U} = \frac{1}{DS + \frac{U_1 S_m}{T_0}}\left(1 - \frac{M_s}{T_0}\right). \quad (4.3.19)$$

Let us calculate the stress value in the acoustic field when the $\sigma \sim \varepsilon$ diagram has a reflection point (S_{fU}), from which the slope angle tends (increases) to its initial elastic value. To do this, we equate T_e from formula (4.3.13) at $\beta = \pi/2$ and $\lambda = 0$ to M_f. As a result:

$$S_{fU} = \frac{1}{D}\left(1 - \frac{M_f}{T_0} - \frac{U}{T_0}\right) < S_f \text{ from (3.4.21)} \quad (4.3.20)$$

The inequality $S_{fU} < S_f$ correctly reflects the experimental result (Fig. 2.32) that the ultrasound-assisted pseudoelasticity tends to its completion at a smaller deformation value than that in the ultrasound-free case.

And lastly, the constant r_U that stands in formula (4.3.18) reflects another experimental fact that the sign of the ultra-sonic action changes from positive (assisting) to negative (suppressing) depending on the stage of transformation. The inequality $r_U > r$ ensures that closer to the finish of the transformation, the ultrasound-assisted $\sigma \sim \varepsilon$ diagram runs above the ordinary one.

Therefore, the extension of the synthetic theory expressed in formulae (4.3.13)-(4.3.20) leads to a qualitative correspondence with experiments. The next step is to inspect its quantitative correctness.

4.3.4 Results. Discussion

This section deals with plotting $\sigma \sim \varepsilon$ diagrams of NiTiRe alloy at a constant temperature $T_0 = 283$ K in an acoustic field. The samples at the austenite state are subjected to uniaxial tension within the martensite transformation temperature range. Two loading regimes are applied: (i) static stress alone and (ii) static and vibrating stresses with the amplitude of ultrasonic deformation $\varepsilon_m = 2 \times 10^{-4}$ (Steckmann et al., 1999). The amplitude of alternating stress is calculated via Young law as

$$\sigma_m = E\varepsilon_m, \quad (4.3.21)$$

where E is the Young modulus, $E = 80$ GPa. As a result, we obtain $\sigma_m = 16$ MPa.

First, we plot $\sigma \sim \varepsilon$ diagram without ultrasonic action (Fig. 4.27, line 1). We use Eqs (3.4.16)-(3.4.20) to do this. As a result, we arrive at the correct results: a) $S_\Phi = 88.3$ MPa and b) the model $\sigma \sim \varepsilon$ curve shows good agreement with the experiment. Line 1 in Fig. 4.27 is constructed with the following values of constants: $D = 1.2 \times 10^{-4}$ MPa^{-1}, $r = 1300$ K, $M_s = 280$ K, $M_f = 260$ K.

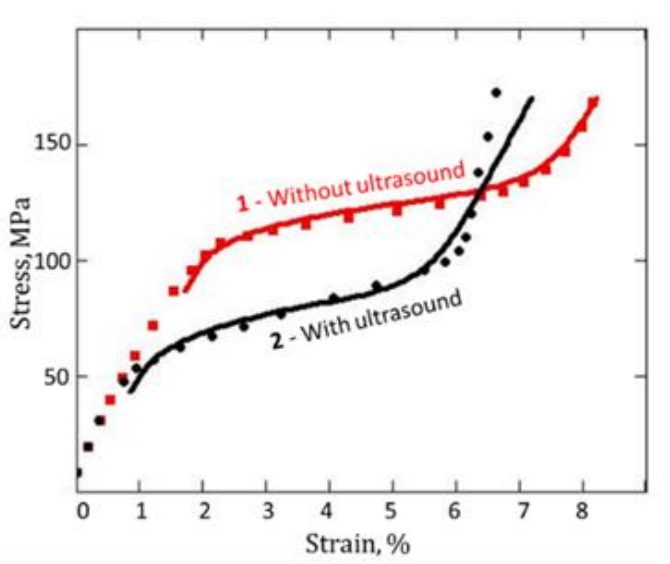

Fig. 4.27 Pseudoelastic σ~ε diagram of NiTiRe alloy at constant temperature ($T_0 = 283$ K) in uniaxial tension: 1 – static loading, 2 – simultaneous action of static and ultrasonic loading ($f = 18$ kHz). Lines – model, symbols – experiment (Steckmann et al., 1999).

The next step is $\sigma \sim \varepsilon$ diagram in the presence of ultrasound (line 2 in Fig. 4.27). The model results have been obtained via formulae (4.3.1)-(4.3.18) with the following values of constants: $U_1 = 3.75 \times 10^{-2}$ MPa^{-1}, $U_2 = 22$ K/MPa. It must be stressed that the values of constants D and r remain unchangeable.

Inspect the behavior of the strain intensity for variously oriented microvolumes for ordinary and ultra-sound-assisted deformations. Fig. 4.28 demonstrates $\varphi_{NU} \sim \sigma$ and $\varphi_N \sim \sigma$ plots obtained via Eqs (4.3.16) and (3.4.15), respectively.

The following conclusion can be derived from this figure:

(i) According to Eq. (4.3.17), the start of ultrasound-assisted plastic (pseudoelastic) deformation takes place at $S_{\Phi U} = 38.3$ MPa (compare to $S_\Phi = 88.3$ MPa without ultrasound).

(ii) The stress range where pseudoelastic deformation develops shifts toward smaller stresses.

The above-listed points have been achieved by introducing the term U into the formula for the effective temperature.

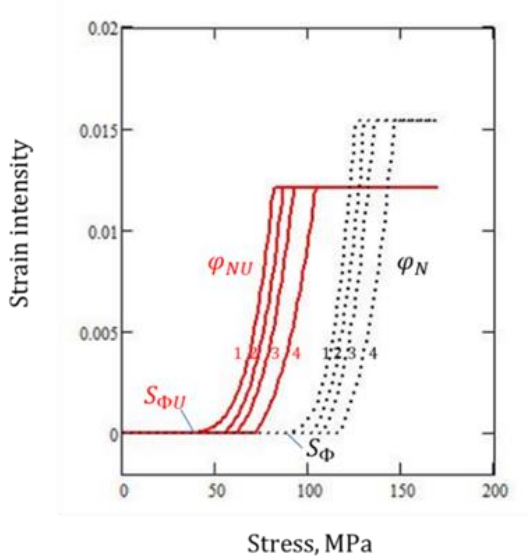

Fig. 4.28 Strain intensity Vs. Stress plots for various directions 1-4: $\beta = \pi/2, \pi/4, \pi/6, \pi/12$ ($\lambda = 0$)

With r_U from Eq. (4.3.15) standing in the denominator in formula (4.3.18), we have obtained the result correlating with Malygin's predictions (Malygin, 2001), namely

(iii) Acoustic energy can decrease or increase the stresses needed to develop pseudoelastic deformation (in our case, the sign of ultrasonic action changes at the very end of the transformation, $\varepsilon \approx 6.4$ %).

All the results above are in full accordance with the experimental records. Therefore, we may conclude that the extension of the synthetic theory leads to qualitatively and quantitatively correct results.

The results regarding section 4.3 are published in

Alhilfi, A. & Rusinko, A. (2022)c.
Alhilfi, A. & Rusinko, A. (2022)d.
Alhilfi, A. & Ruszinkó, E. (2023)

Thesis III

In terms of the Synthetic theory, a model for the analytical description of the ultrasound-assisted phase transformations of the shape memory alloys has been developed. The model results correctly correlate with experimental recordings for the following phenomena:

(i) Ultrasound impulses induce strain drops during austenite transformation (transformation plasticity)

(ii) Ultrasound superimposed on a static load decreases stresses needed to start martensite transformation during pseudoelastic deformation

Conclusion

This thesis presents the results of the investigations regarding the effects of ultrasound on the inelastic deformation of metals. The Synthetic theory of inelastic deformation is taken for the mathematic apparatus to model the phenomena observed in the acoustic field. There are three main themes addressed in this study.

The first theme is a string of phenomena accompanying the plastic deformation of metals in an ultrasound field: ultrasound temporary softening and ultrasound residual hardening/softening. The temporary softening (acoustoplasticity) is observed during the simultaneous action of ultrasound and unidirectional loading, and the residual effects manifest themselves in the post-sonication period. While the former phenomenon always gives the same result – the reduction of static stresses needed to develop plastic deformation due to the ultrasound energy inflow – the latter strongly depends on the mechanisms governing the temporary softening. If, as a result of acoustoplasticity, a stable defect structure forms, typical for materials with high stacking fault energy, the residual hardening will be observed. In other words, the defect structure formed during the sonication will hamper the development of plastic deformation in the post-sonication stage, and more significant stresses are needed to continue the material flow. Materials with low stacking fault energy come from the acoustoplasticity with a softer defect structure, which reduces the stresses needed to induce the material flow after the sonication. Both temporary and residual effects become more evident as the ultrasound intensity grows.

In order to model the ultrasound-assisted plastic deformation, two new terms are inserted into the relationship of the Synthetic theory that governs the deformation state of the material. The first term symbolizes that ultrasound facilitates the development of plastic deformation by activating blocked dislocations, localized heating, and dynamic softening. The second one reflects the degree of the material hardening obtained during the acoustoplasticity. Both of these terms are increasing functions of ultrasound intensity.

The second topic is modeling ultrasound's effect on time-dependent processes, such as the creep deformation of metals and the relaxation of work-hardened materials. Two cases are considered: (i) the ultrasound is superimposed upon the creep deformation from the beginning of the experiment, and (ii) the ultrasound acts periodically. In both cases, the sonication results in a drastic increase in creep deformation. Similar to the previous case, the flow-rule relationship is extended by a term governing the

time-dependent behavior of the ultrasound-induced defects of the metal's crystalline grid. Since the number of ultrasound defects is not a monotonic function of time (they first increase and then go to the plateau value), the effect from periodic sonication fades with the number of ultrasound switches.

With the ultrasound effect on the recovery (relaxation) processes, experiments record that even at low (room) temperatures, acoustic energy decreases the hardness of the materials preliminarily subjected to plastic deformation. This phenomenon becomes more evident as the magnitude of the plastic prestrain grows. The relationships correctly describing the ultrasound-induced recovery have been obtained by extending the element of the synthetic theory, which governs relaxation processes, by the term proportional to the product of ultrasound intensity and the magnitude of plastic prestrain.

The last (third) sphere of interest lies in the ultrasound-assisted phase transformations of shape memory alloys. A series of exciting results can be found in this area. Ultrasound, the source of mechanical and thermal stimuli for austenite transformation, causes strain drops on the strain~temperature diagram, and their magnitudes strongly depend on the temperature when the sonication happens. After the ultrasound is Off, the deformation grows a little, after which the strain-temperature diagram runs according to austenitic transformation kinetics, although beneath the standard curve. Another effect is that in the presence of ultrasound impulses, the finish temperature of the austenite transformation reduces compared to the ordinary case.

With martensite transformation, ultrasound superimposed on the static load during pseudoelastic experiment reduces the stress needed to start martensite transformation. Further, acoustic energy shortens the deformation range within which the transformation occurs and varies the slope angle of the stress~strain diagram.

In order to model the phenomena considered above, following the experimental results that acoustic energy shifts the effective temperature of the transformations, the relationship that defines the effective temperature is extended by a term reflecting the presence of ultrasound and its thermal and mechanical impact on the transformation considered.

To conclude, I summarize the main contributions of this work as follows:

I have extended the Synthetic theory so that it enables to model: (**i**) ultrasound-assisted plastic deformation, (**ii**) ultrasound-assisted creep deformation and recovery, and (**iii**) ultrasound-assisted phase transformations. All model results agree with experimental data (numerical calculations have been carried out using the MathCad13-Professional software package), which testifies to the qualitative and quantitative reliability of the model developed.

List of contributions

Alhilfi, A. & Rusinko, A. (2021), Ultrasonic Temporary Softening And Residual Softening In Terms Of The Synthetic Theory, AGTECO 2021, Kecskemét, Hungary, Nov. 25-27, 202, Published in journal Gradus 19(2), 2022.

Alhilfi, A. & Rusinko, A., (2022)a, Modelling of ultrasonic temporary and residual effects, *JTAMS*, Sofia (0.4), vol.52, pp. 64-74

Alhilfi, A. & Rusinko, A. (2022)b. Ultrasonic temporary softening and residual hardening. *Engineering Review*: 42(2).

Alhilfi, A. & Rusinko, A. (2022)c. Austenite Transformation of Shape Memory Alloys in the Ultrasonic Field. *Mechanics of Solids*, 57(5), 1097-1103.

Alhilfi, A. & Rusinko, A. (2022)d. Effect of Ultrasound on the Pseudoelasticity of Shape Memory Alloys. *Journal of Materials Science and Chemical Engineering*, 10(6), 1-12.

Alhilfi, A. & Ruszinkó, E. (2023). Effect of Ultrasound on the Austenite Transformation of Shape Memory Alloys. *Acta Polytechnica Hungarica*, 20(4).

Rusinko, A. & Alhilfi, A. (2020), Evolution of loading surface in the ultrasonic field, Proceedings of the Engineering Symposium at Bánki, pp. 35-40.

Rusinko, A. & Alhilfi, A. (2021), Ultrasound-assisted creep deformation of metals. *Acta Periodica Technologica*, (52), 265-273.

Rusinko, A. Alhilfi, A., Rusinko, M. (2022). An analytic description of the creep deformation of metals in the ultrasonic field. *Mechanics of Time-Dependent Materials*, 26(3), 649-661.

Ruszinko, E. & Alhilfi, A. (2021), The Effect of Ultrasound on Strain-hardened Metals. *Acta Polytechnica Hungarica*, 18(8), 221-233.

References

Abdullah, A., Sotoodezadeh, M., Abedini, R., & Fartashvand, V. (2013). Experimental study on ultrasonic use in dry creep-feed up-grinding of aluminum 7075 and Steel X210Cr12. International Journal of Precision Engineering and Manufacturing, 14(2), 191-198.

Achenbach, M., Atanackovic, T., & Müller, I. (1986). A model for memory alloys in plane strain. International Journal of Solids and Structures, 22(2), 171-193.

Arbtin Jr., E., Murphym G., 1953, Correlation of Vickers hardness number, modulus of elasticity, and the yield strength for ductile metals. Ames Laboratory ISC Technical Reports.

Bagherzadeh, S., & Abrinia, K. 2015. Effect of ultra-sonic vibration on compression behavior and micro-structural characteristics of commercially pure alumi-num. Journal of Materials Engineering and Perfor-mance, 24(11), 4364-4376.

Bansiddhi A, Sargeant T, Stupp S and Dunand D (2008) Porous nickel-titanium for bone implants: a review. Acta Biomaterialia 4, pp773–782.

Bao, M., Zhou, Q., Dong, W., Lou, X., Zhang, Y. (2013) Ultrasound-modulated shape memory and payload release effects in a biodegradable cylindrical rod made of chitosan-functionalized PLGA microsphere, BioMac.

Batdorf, S. and Budiansky, B. (1949) A mathematical theory of plasticity based on the concept of slip, NACA, Technical note, 871.

Bellini A, Colli M and Dragoni E (2009) Mechatronic design of a shape memory alloy actuator for automotive tumble flaps: a case study. IEEE Transactions on Industrial Electronics 56(7): 2644–2656.

Belyaev, S., Volkov, A., & Resnina, N. (2014). Alternate stresses and temperature variation as factors of influence of ultrasonic vibration on mechanical and functional properties of shape memory alloys. Ultrasonics, 54(1), 84-89.

Blagoveshchenskii, V., Panin, 2007 I.: An increase in the rate of plastic deformation under the effect of ultrasound. The Physics of Metals and Metallography, 103, 424-426, 2007.):

Blaha, F., Langenecker, B., (1955), Dehnung von Zink-Kristallen unter Ultraschalleinwirkung. Naturwissenschaften 42, 556. doi.org/10.1007/BF00623773.

Blum, W., Zhu, Q., Merkel, R., & McQueen, H. J. (1996). Geometric dynamic recrystallization in hot torsion of Al- 5Mg- 0.6 Mn (AA5083). Materials Science and Engineering: A, 205(1-2), 23-30, https://doi.org/10.1016/0921-5093(95)09990-5.

Breczko, T., Rubanik, V.V., Rubanik Jr., V.V. (1999) Study of behaviour NiTi-alloy under action of ultrasound, Proc. of SPIE, NDTCS-98 3687 310–312.

Brehl, D. A., & Dow, T. A. (2008). Review of vibration-assisted machining. Precision engineering, 32(3), 153-172.

Buchelnikov, V., Pikshtein, I., Grechishin, R., Khudoverdyan, T., Koledov, V., Kuzavko, Y., Nazarkin, I., Shavrov, V. Takagi, T. (2004) Ultrasound-induced martensitic transition in ferromagnetic Ni2.15Mn0.81Fe0.04Ga shape memory alloy, J. Magn. Mater. 272–276 2025–2026.

Daud, Y., Lucas, M., & Huang, Z. (2006). Superimposed ultrasonic oscillations in compression tests of aluminium. Ultrasonics, 44, e511-e515, https://doi.org/10.1016/j.ultras.2006.05.116.

Daud, Y., Lucas, M., & Huang, Z. (2007). Modelling the effects of superimposed ultrasonic vibrations on tension and compression tests of aluminium. Journal of Materials Processing Technology, 186(1-3), 179-190. doi.org/10.1016/j.jmatprotec.2006.12.032.

Daud, Y., Lucas, M., & Huang, Z. H. (2006). Ultrasonic compression tests on aluminium. In Applied Mechanics and Materials (Vol. 3, pp. 99-104). Trans Tech Publications Ltd. doi.org/10.4028/www.scientific.net/AMM.3-4.99.

Deng, J., Zhang, L., Dong, J., & Cohen, P. H. (2016). AFM-based 3D nanofabrication using ultrasonic vibration assisted nanomachining. Journal of Manufacturing Processes, 24, 195-202.

Deshpande, A., & Hsu, K. (2018). Acoustic energy enabled dynamic recovery in aluminum and its effects on stress evolution and post-deformation microstructure. Materials Science and Engineering: A, 711, 62-68, https://doi.org/10.1016/j.msea.2017.11.015.

Deshpande, A., Tofangchi, A., & Hsu, K. 2019. Micro-structure evolution of Al6061 and copper during ultra-sonic energy assisted compression. Materials Characterization, 153, 240-250. https://doi.org/10.1016/j.matchar.2019.05.005

Dutta, R. K., Petrov, R. H., Delhez, R., Hermans, M. J. M., Richardson, I. M., & Böttger, A. J. (2013). The effect of tensile deformation by in situ ultrasonic treatment on the microstructure of low-carbon steel. Acta Materialia, 61(5), 1592-1602, https://doi.org/10.1016/j.actamat.2012.11.036.

Fitzpatrick, R. (2018). Oscillations and waves: an introduction. CRC Press.

Geibler, U., Schneider-Ramelow, M., & Reichl, H. 2009. Hardening and softening in AlSi1 bond contacts during ultrasonic wire bonding. IEEE Transactions on Components and Packaging Technologies, 32(4), 794-799. DOI: 10.1109/TCAPT.2008.2009930.

Goliboroda, I. M., & Rusinko, K. N. (1996). Derivation of a universal relation between tangential stress and shear strain intensities in describing reversible martensitic deformation within the framework of a synthetic model. Journal of applied mechanics and technical physics, 37(3), 447-453.

Goliboroda, I., Rusinko, K., & Tanaka, K. (1999). Description of a Fe-based shape memory alloy thermomechanical behavior in terms of the synthetic model. Computational materials science, 13(4), 218-226.

Golyamina, I. et al. (1979), Ultrasound: small encyclopedia, Soviet Encyclopaedia, Moscow (in Russian).

Graff, K. F. (2015). Ultrasonic metal forming: Processing. In Power Ultrasonics (pp. 377-438). Woodhead Publishing.

Hartl D, Lagoudas D, Calkins F and Mabe J (2010a) Use of a Ni60Ti shape memory alloy for active jet engine chevron application: I. Thermomechanical characterization. Smart Materials and Structures 19(1): 015020.

Hartl D, Mooney J, Lagoudas D, Calkins F and Mabe J (2010b) Use of a Ni60Ti shape-memory alloy for active jet engine chevron application: ii. Experimentally validated numerical analysis. Smart Materials and Structures 19(1).

Hartl D. and Lagoudas D. (2007) Aerospace applications of shape-memory alloys. Proceedings of the Institution of Mechanical Engineers, Part G: Journal of Aerospace Engineering 221(4): 535–552.

Huang, H., Pequegnat, A., Chang, B. H., Mayer, M., Du, D., & Zhou, Y. 2009. Influence of superimposed ultrasound on deformability of Cu. Journal of Applied Physics, 106(11), 113514. https://doi.org/10.1063/1.3266170

Huang, K. E., & Logé, R. E. (2016). A review of dynamic recrystallization phenomena in metallic materials. Materials & Design, 111, 548-574, https://doi.org/10.1016/j.matdes.2016.09.012.

Humphreys, F. J., & Hatherly, M. (2012). Recrystallization and related annealing phenomena. Elsevier.

Ilyushin, A. A. (1963). Plasticity: Fundamentals of general mathematical theory. Akademiia Nauk, SSSR. (in Russian).

Inoue, M. (1984). Studies on Ultrasonic Metal Tube Drawing. Mem Sagami Inst Technol, 18(1), p41-55.

Jani, J. M., Leary, M., & Subic, A. (2014). Shape Memory Alloys in Automotive Applications. Applied Mechanics and Materials, 663, 248–253.

Jani, J. M., Leary, M., Subic, A., & Gibson, M. A. (2014). A review of shape memory alloy research, applications and opportunities. Materials & Design (1980-2015), 56, 1078-1113.

Kang, J., Liu, X., & Xu, M. (2020). Plastic deformation of pure copper in ultrasonic assisted micro-tensile test. Materials Science and Engineering: A, 785, 139364, https://doi.org/10.1016/j.msea.2020.139364.

Kim B, Lee MG, Lee YP, Kim Y and Lee G (2006) An earthworm-like micro robot using shape-memory alloy actuator. Sensors and Actuators A: Physical 125(2): 429–437.

Klubovich, V.V., Rubanik, V.V., Likhachev, V.A., Rubanik Jr., V.V. Dorodeiko, V.G. (1997) Generation of shape memory effect in Ti-Ni alloy by means of ultrasound, in A. Pelton, D. Hodgson, S. Russel, T. Duering (Eds.), Proc of the 2nd International Conference on Shape Memory and Superelastic Technologies, SMST, pp. 59–64.

Kulemin, A. V. 1978. Ultrasound and Diffusion in Metals. Metallurgia Publ., Moscow.

Kumar, J. (2013). Ultrasonic machining—a comprehensive review. Machining Science and Technology, 17(3), 325-379.

Kumar, J., Khamba, J. S., & Mohapatra, S. K. (2008). An investigation into the machining characteristics of titanium using ultrasonic machining. International Journal of Machining and Machinability of Materials, 3(1/2), 143.

Kumar, S., Wu, C. S., Padhy, G. K., & Ding, W. (2017). Application of ultrasonic vibrations in welding and metal processing: A status review. Journal of Manufacturing Processes, 26, 295–322. https://doi.org/10.1016/J.JMAPRO.2017.02.027

Langenecker, B. (1961). Work-softening of metal crystals by alternating the rate of glide strain. Acta metallurgica, 9(10), 937-940.

Langenecker, B. (1966). Effects of ultrasound on deformation characteristics of metals. IEEE transactions on sonics and ultrasonics, 13(1), 1-8.

Liang, C., & Rogers, C. A. (1997). One-dimensional thermomechanical constitutive relations for shape memory materials. Journal of intelligent material systems and structures, 8(4), 285-302.

Lichachov, V., Malinin, V. (1993). Structure-analytical theory of strength, St. Peterburg (in Russian).

Likhachev, V. A., Kuz'min, S. L., & Kamentseva, Z. P. (1987). Effect of the Memory of Shape. Leningrad, Leningrad State University.

Liu, Y., Wang, C., & Bi, R. (2022). Acoustic residual softening and microstructure evolution of T2 copper foil in ultrasonic vibration assisted micro-tension. Materials Science and Engineering: A, 841, 143044, https://doi.org/10.1016/j.msea.2022.143044.

Liu, Y., Wang, C., & Bi, R. (2022). Acoustic residual softening and microstructure evolution of T2 copper foil in ultrasonic vibration assisted micro-tension. Materials Science and Engineering: A, 841, 143044, https://doi.org/10.1016/j.msea.2022.143044.

Lum, I., Hang, C. J., Mayer, M., & Zhou, Y. (2009). In situ studies of the effect of ultrasound during deformation on residual hardness of a metal. Journal of electronic materials, 38(5), 647-654, https://doi.org/10.1007/s11664-009-0732-4.

Lum, I., Huang, H., Chang, B. H., Mayer, M., Du, D., & Zhou, Y. 2009. Effects of superimposed ultrasound on deformation of gold. Journal of Applied Physics, 105(2), 024905. https://doi.org/10.1063/1.3068352

Malekipour, E., Heidary, H., Majd, N. S., Mazdak, S., & Sharifi, E. (2020). Effect of resonant frequency variation on the ultrasonically assisted deep drawing process: numerical and experimental study. The International Journal of Advanced Manufacturing Technology, 106(5), 2243-2264.

Malygin, G. A. 2000. Acoustoplastic effect and the stress superimposition mechanism. Physics of the Solid State, 42(1), 72-78.

Mercier, O., Melton, K. N., & De Préville, Y. (1979). Low-frequency internal friction peaks associated with the martensitic phase transformation of NiTi. Acta Metallurgica, 27(9), 1467-1475.

Morgan N. (2004) Medical shape-memory alloy applications—the market and its products. Materials Science and Engineering: A 378(1–2): 16–23.

Mueller, I. (1987). Shape memory alloys-Phenomenology and Simulation. London Math. Soc. Lect. Note, (122), 22-35.

Qin C.J., Ma P.S. and Yao Q. (2004) A prototype micro-wheeled-robot using shape memory alloy actuator. Sensors and Actuators A: Physical 113(1): 94–99.

Rubanick, V., Rubanick, V., & Razov, A. (1999). Thermographic investigations of reverse martensitic transformation in TiNi under the action of ultrasound. In International Symposium on Shape Memory Alloys: Fundamentals, Modeling and Industrial Applications as held at the 38 th Annual Conference of Metallurgists of CIM (pp. 283-287).

Rubanik Jr., V.V. Rubanik, V.V. Klubovich, V.V. (2008) The influence of ultrasound on the shape memory behavior, MSE A 481–482 620–622.

Rubanik, V. V., Klubovich, V. V., & Rubanik Jr, V. V. (2003, October). The ultrasounds initiation of SME. In Journal de Physique IV (Proceedings) (Vol. 112, pp. 249-251). EDP sciences. https://doi.org/10.1051/jp4:2003876.

Rubanik, V. V., Rubanik Jr, V. V., Dorodeiko, V., & Miliukina, S. (2013). Influence of ultrasonic treatment on shape memory effects in Ti-50, 4at.% Ni alloy. In Materials Science Forum (Vol. 738, pp. 362-366). Trans Tech Publications Ltd. https://doi.org/10.4028/www.scientific.net/MSF.738-739.362.

Rukosuyev, M., Goo, C. S., & Jun, M. B. (2010). Understanding the effects of the system parameters of an ultrasonic cutting fluid application system for micro-machining. Journal of Manufacturing Processes, 12(2), 92-98.

Rusinko, A. & Fenyvesi, D. (2014). On the Advantages of the Theories of Plasticity with Singular Loading Surface. Journal of Materials Science and Chemical Engineering, 2(11), 14.

Rusinko, A. & Rusinko, K. (2009). Synthetic theory of irreversible deformation in the context of fundamental bases of plasticity. *Mechanics of Materials*, 41(2), 106-120.

Rusinko, A. & Rusinko, K. (2011). Plasticity and creep of metals. Springer Science & Business Media.

Rusinko, A. & Varga, P. (2019). Analytical description of the steady-state creep of metals in the presence of direct current. Acta Polytechnica Hungarica, 16(7).

Rusinko, A. (2012), Ultrasound and Irrecoverable Deformation in Metals, LAP LAMBERT Academic Publishing, 168 p.

Rusinko, A. (2012). Peculiarities of irreversible straining in step-wise loading, reverse and inverse creep. Acta Mechanica Solida Sinica, 25(2), 152-167.

Rusinko, A. (2014). Feigen's Phenomenon in Terms of the Synthetic Theory. International Journal of Engineering Research and Applications, 4, 172-180.

Rusinko, A. (2016). Modeling the effect of DC on the creep of metals in terms of the synthetic theory of irrecoverable deformation. Mechanics of Materials, 93, 163-167.

Rusinko, A., Varga, P. Modelling of the plastic deformation and primary creep of metals coupled with DC in terms of the synthetic theory of irrecoverable deformation. Mech Time-Depend Mater 23, 23–33 (2019).

Rusynko, K. N., & Shandrivskyi, A. H. (1996). Irreversible deformation in the course of a martensite transformation. Materials Science, 31(6), 786-789.

Sakai, T., Belyakov, A., Kaibyshev, R., Miura, H., & Jonas, J. J. (2014). Dynamic and post-dynamic recrystallization under hot, cold and severe plastic deformation conditions. Progress in materials science, 60, 130-207, https://doi.org/10.1016/j.pmatsci.2013.09.002.

Samigullina, A., Murzinova, M., Mukhametgalina, A., Zhilyaev, A. P. and Nazarov, A. A. (2018) Effect of ultrasonic treatment on the characteristics of superplasticity of tita-nium alloy Ti-6Al-4V. In Defect and Diffusion Forum, Trans Tech Publications Ltd. 385, 53-58.

Sanders J. (1954) Plastic Stress-Strain Relations Based on Linear Loading Functions. Proceedings of the Second USA National Congress of Applied Mechanics, Ann Arbor, 14-18 June 1954, 455-460.

Sapozhnikov, K. V., Vetrov, V. V., Pulnev, S. A. and Kustov, S. B. (1996) Acous-tic-pseudoelastic effect and internal friction during stress-induced martensitic trans-formation in Cu-Al-Ni single crystals. Scripta Materialia, 34, 1543-1548. https://doi.org/10.1016/1359-6462(96)00013-9

Sathish, S., Mallik, U. and Raju, T. (2013) Corrosion Behavior of Cu-Zn-Ni Shape Memory Alloys, Journal of Minerals and Materials Characterization and Engineering, 1, 2, 49-54. DOI: 10.4236/jmmce.2013.12010

Schmid, E., Boas, W., 1935. Kristallplastizitact. Spring-Verlag, Berlin, pp. 152–157.

Sedaghat, H., Xu, W., & Zhang, L. (2019). Ultrasonic vibration-assisted metal forming: Constitutive modelling of acoustoplasticity and applications. Journal of Materials Processing Technology, 265, 122-129, https://doi.org/10.1016/j.jmatprotec.2018.10.012.

Severdenko, V. (1979), Ultrasound and Strength, Minsk (in Russian).

Shao, G., Li, H., & Zhan, M. (2021). A review on ultrasonic-assisted forming: Mechanism, model, and process. Chinese Journal of Mechanical Engineering, 34(1), 1-24.

Siddiq, A., & El Sayed, T. (2011). Acoustic softening in metals during ultrasonic assisted deformation via CP-FEM. Materials Letters, 65(2), 356-359, https://doi.org/10.1016/j.matlet.2010.10.031.

Siddiq, A., & Ghassemieh, E. (2008)a. Thermomechanical analyses of ultrasonic welding process using thermal and acoustic softening effects. Mechanics of Materials, 40(12), 982-1000. doi.org/10.1016/j.mechmat.2008.06.004.

Siddiq, A., & Ghassemieh, E. (2008)b. Modelling and Characterization of Ultrasonic Consolidation Process of Aluminum Alloys. MRS Online Proceedings Library (OPL), 1079. doi.org/10.1557/PROC-1079-N09-05.

Siu, K. W., & Ngan, A. H. W. (2011). Understanding acoustoplasticity through dislocation dynamics simulations. Philosophical Magazine, 91(34), 4367-4387, https://doi.org/10.1080/14786435.2011.606237.

Siu, K. W., & Ngan, A. H. W. (2013). Oscillation-induced softening in copper and molybdenum from nano-to micro-length scales. Materials Science and Engineering: A, 572, 56-64, https://doi.org/10.1016/j.msea.2013.02.037.

Siu, K. W., Ngan, A. H. W., & Jones, I. P. (2019). New insight on acoustoplasticity–ultrasonic irradiation enhances subgrain formation during deformation. International Journal of Plasticity, 27(5), 788-800, https://doi.org/10.1016/j.ijplas.2010.09.007.

Steckmann, H., Kolomytsev, V.I., Kozlov, A.V. Acoustoplastic effect in the shape memory alloy Ni–Ti–Re at ultrasonic frequency, Ultrasonics 37 (1999) 59–62.

Stoeckel D. (1990) Shape-memory actuators for automotive applications. Materials & Design 11(6): 302–307.

Sun L, Huang WM, Ding Z et al. (2012) Stimulus-responsive shape-memory materials: a review. Materials & Design 33: 577–640.

Susan, M. M., Dumitras, P. G., & Iliescu, V. G. (2007). Experimental research of the ultrasonic softening in cold-rolled steel strips. Электронная обработка материалов, (1), 82-84.

Thoe, T. B., Aspinwall, D. K., & Wise, M. L. H. (1998). Review on ultrasonic machining. International journal of machine tools and manufacture, 38(4), 239-255.

Tsimbalistyj, Y.I., Vlasenko, V.I. (1983). Studies of stress and creep relaxation under ultrasonic cyclic loading. In: Ultrasonics International 83 Conference Proceedings, pp. 507–512.

Tyapunina, N. A., Blagoveshchenskii, V. V., Zinen-kova, G. M., & Ivashkin, Y. A. 1982. Characteristics of plastic deformation under the action of ultra-sound. Soviet Physics Journal, 25(6), 569-578.

Varga, P., & Rusinko, A. (2018, April). Modeling the effects of imposed current on the creep of SAC305 solder material. In 2018 19th International Conference on Thermal, Mechanical and Multi-Physics Simulation and Experiments in Microelectronics and Microsystems (EuroSimE) (pp. 1-4). IEEE.

Wang Z, Hang G, Li J, Wang Y and Xiao K (2008) A micro-robot fish with embedded shape-memory alloy wire actuated flexible biomimetic fin. Sensors and Actuators A: Physical 144(2): 354–360.

Wang, C. J., Liu, Y., Guo, B., Shan, D. B., & Zhang, B. (2016). Acoustic softening and stress superposition in ultrasonic vibration assisted uniaxial tension of copper foil: Experiments and modeling. Materials & Design, 112, 246-253, https://doi.org/10.1016/j.matdes.2016.09.042.

Wanhill, R. J. H., & Ashok, B. (2017). Shape memory alloys (SMAs) for aerospace applications. Aerospace Materials and Material Technologies, 467-481.

Westmacott, K. H., & Langenecker, B. (1965). Dislocation structure in ultrasonically irradiated aluminum. Physical review letters, 14(7), 221.

Yadav, S., & Doumanidis, C. (2005). Thermomechanical analysis of an ultrasonic rapid manufacturing (URM) system. Journal of Manufacturing Processes, 7(2), 153-161. doi.org/10.1016/S1526-6125(05)70092-X.

Yao, Z., Kim, G. Y., Faidley, L., Zou, Q., Mei, D., & Chen, Z. (2012). Effects of superimposed high-frequency vibration on deformation of aluminum in micro/meso-scale upsetting. Journal of Materials Processing Technology, 212(3), 640-646, https://doi.org/10.1016/j.jmatprotec.2011.10.017.

Zhou, H., Cui, H., Qin, Q. H., Wang, H., & Shen, Y. (2017). A comparative study of mechanical and microstructural characteristics of aluminum and titanium undergoing ultrasonic assisted compression testing. Materials Science and Engineering: A, 682, 376-388, https://doi.org/10.1016/j.msea.2016.11.021.

Zohrevand, M., Aghaie-Khafri, M., Forouzan, F., & Vuorinen, E. (2022). An investigation on microstructure and mechanical properties of 316 stainless steel: a comparison between ultrasonic treatment and thermal annealing. Philosophical Magazine, 1-23. doi.org/10.1080/14786435.2022.2048113.

Zohrevand, M., Aghaie-Khafri, M., Forouzan, F., & Vuorinen, E. (2021). Microstructural evolutions under ultrasonic treatment in 304 and 316 austenitic stainless steels: impact of stacking fault energy. steel research international, 92(9), 2100041, https://doi.org/10.1002/srin.202100041.